Asynchrones Quantum Ghost Imaging

English translation of the PhD Thesis of

CARSTEN PITSCH

who also edited this translation

Original document in German can be found under:

https://doi.org/10.5445/IR/1000172085

Filed at Karlsruhe Institut für Technologie (KIT)

This work has been translated using ChatGPT.

Possible errors may occur.

The author does not guarantee correctness of the translation.

Contents

List of Abbreviations . . . . . **iii**

1 Introduction **1**

2 Theoretical Foundations **7**

2.1 (Active) remote sensing 7

2.1.1 Lidar 8

2.1.2 Gated Viewing 11

2.2 Single-Pixel Imaging 13

2.2.1 Laser Scanner 13

2.2.2 Imaging with Structured Light 15

2.3 Imaging with Entangled Light 17

2.3.1 Spontaneous Parametric Down Conversion 18

2.3.2 Quasi-Phase Matching 21

2.4 Quantum Ghost Imaging 25

2.4.1 Resolution Limits of QGI 28

2.4.2 Quantum Ghost Imaging with Asynchronous Detection 29

2.5 Single Photon Avalanche Diodes (SPAD) 31

2.5.1 SPAD Design and Layout 32

2.5.2 Time acquisition of a SPAD 34

2.6 Image Enhancement and Object Detection 38

2.6.1 Noise Effects in QGI 38

2.6.2 Object Detection and 3D Optimization 40

3 Asynchronous Quantum Ghost Imaging . . . 43
3.1 Photon-Pair Source . . . 44
3.2 Detectors . . . 48
3.3 Temporal Resynchronization and Correction . . . 50
3.4 Results . . . 54
3.4.1 Choice of Pump Laser . . . 54
3.4.2 Proof-of-Concept . . . 57
3.4.3 3D Imaging . . . 62
3.4.4 Resolution . . . 70
3.4.5 Spectral Properties . . . 73
3.4.6 Automated Coincidence Analysis and Object Recognition . . . 78

4 Further Developments and Outlook . . . 81
4.1 Setups . . . 81
4.1.1 Ghost Spectroscopy . . . 81
4.1.2 Hyperspectral Quantum Ghost Imaging . . . 83
4.1.3 Hyperspectral Single Photon Imaging . . . 84
4.2 Detectors . . . 86
4.2.1 SPAD Detectors . . . 87
4.2.2 Superconducting Nanowires . . . 89
4.2.3 Optical Converters . . . 89

5 Summary . . . 93

List of Publications . . . 115

List of Abbreviations

QGI	Quantum Ghost Imaging
SPAD	Single Photon Avalanche Diode
DE	Detection Efficiency
Lidar	Light Detection and Ranging
ToF	Time of Flight
cw	continuous wave
InGaAs	Indium Gallium Arsenide
SLM	Spatial Light Modulator
DMD	Digital Micromirror Device
SPDC	SPontaneous Parametric Downconversion
KTP	Potassium Titanyl Phosphate
ppKTP	periodically poled Potassium Titanyl Phosphate
QPM	Quasi Phase Matching
VIS	visible light spectrum ($\sim 360 - 830\ \mathrm{nm}$)
IR	infrared light spectrum ($\sim 760\ \mathrm{nm} - 10\ \mu\mathrm{m}$)

SWIR	Short Wave Infrared light spectrum ($\sim 760\ \mathrm{nm} - 2{,}5\ \mu\mathrm{m}$)
MIR	Middle Wave Infrared light spectrum ($\sim 2{,}5\ \mu\mathrm{m} - 5\ \mu\mathrm{m}$)
UV	Ultraviolet light spectrum (A: $380 - 315\ \mathrm{nm}$, B: $315 - 280\ \mathrm{nm}$, C: $280 - 100\ \mathrm{nm}$)
sCMOS	scientific CMOS (Complimentary Metal-Oxide Semiconductor)
ICCD	Intesified CCD (Charge Coupled Device
APD	Avalanche Photo Diode
DCR	Dark Count Rate
PDP	Photon Detection Probability
TDC	Time-to-Digital Converter
DLL	Delay Locked Loop
TCSPC	Time Correlated Single Photon Counting
PCI	Peripheral Component Interconnect (Computer connection)
FWHM	Full Width Half Maximum
PoC	Proof of Concept
SNR	Signal to Noise Ratio
CAR	Coincidence to Accidental Ratio
ND	Neutral Density Filter

1 Introduction

Since the prediction of entangled states by Einstein, Podolsky, and Rosen [1], the nature and limitations of the resulting correlations have been discussed and researched in the physics community. The locality of these correlations has been disproven [2, 3], and their causality questioned [4].

As a result, several applications have been found where these correlations are used to outperform classical methods. Recently, there has been significant public interest in applications in quantum computing and quantum communication, which address problems unsolvable by classical methods. For example, quantum computing methods with the appropriate algorithms can solve problems such as path optimization (the "Travelling Salesman" problem) and the prime factorization of large numbers[1] ("Shor's Algorithm") in a foreseeable amount of time [5]. Quantum communication methods, on the other hand, use the correlation of photon pairs to ensure the data security of a communication channel. Since the information of a single photon cannot be "cloned", a potential eavesdropping attempt can be detected through statistical methods [6].

Somewhat less attention has been paid to applications in quantum metrology, although there are numerous applications where the correlation can be exploited [7], particularly in photonic methods [8–10]. This is partly because many classical equivalents exist that compensate for the accuracy of quantum correlation with higher light power. As a result, simpler detectors, which do not have single-photon sensitivity, can be used for many applications.

However, increasing light power is problematic for many applications. For example, many biological samples are altered or even destroyed by the light power itself. In addition, increasing

[1] Much of the encryption used today is based on the multiplication of large prime numbers, whose factorization would take extremely long with classical algorithms (several centuries).

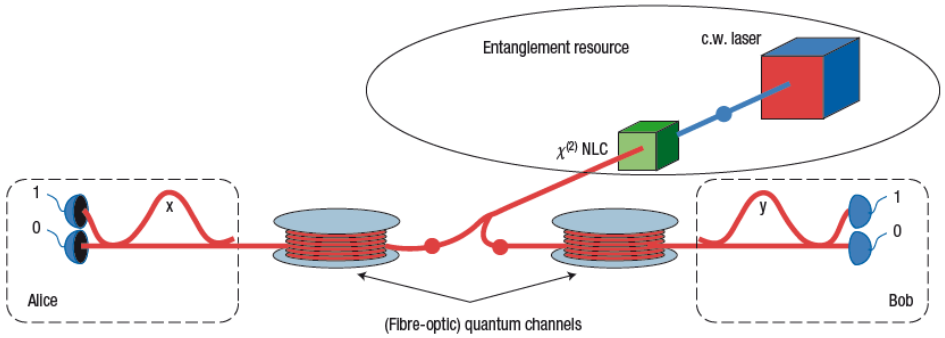

Figure 1.1: Quantum communication setup, using a Franson interferometer as an example. The image is taken from [6].

power can generally lead to environmental problems; for example, in drone swarms, the transmitters and receivers of the individual drones can strongly interfere with each other [11]. Here, photonic quantum metrology methods offer solutions, due to their very low photon dose requirements [12] and the interference resistance of the measurements [13].

Another significant advantage of quantum correlation is the ability to entangle photons of different wavelengths. Thanks to advances in crystal growth and manipulation, sources with a wide range of entangled wavelengths can now be realized. In combination with appropriate methods, it is possible to separate the illumination of the object from its imaging [14], allowing measurements to be made in wavelength ranges where no cameras or detectors are available. Superposition-based systems enable measurements in the spectral range from THz [15], MIR [16, 17], NIR [8] to VIS [18] by superimposing the emission of two entangled photon pair sources, without relying on detector technology in the corresponding spectral range. Some advantages of using quantum methods have already been demonstrated with these setups [19, 20], and first commercial applications are now available [21]. However, due to the principle of this measurement method—the superposition of two photon pair sources—the application of this method is likely limited to transmission or interferometric setups.

For applications in remote sensing, coincidence-based measurement methods are recommended. In these methods, both photons are measured, and their temporal correlation is used to identify photon pairs [22]. As a result, these applications are naturally limited by the corresponding detector technology, but they allow the separation of background noise from quantum light

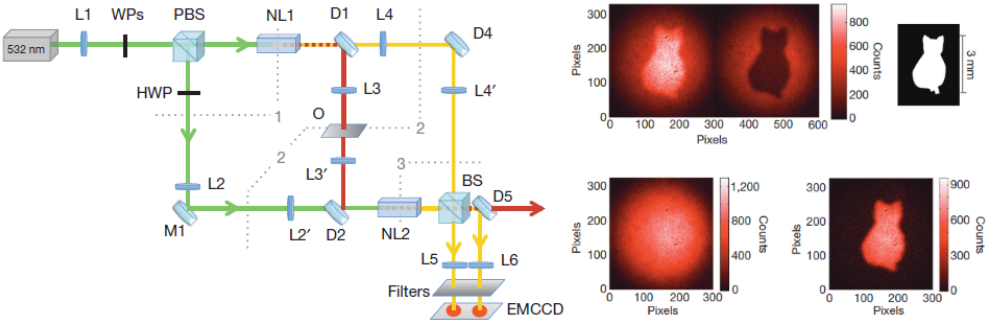

Figure 1.2: Superposition-based quantum imaging setup, also known as "Imaging with undetected photons". The setup is taken from [8].

[13]. Recent developments in single-photon detectors promise further progress, especially in the MIR range [23], where molecule-specific information can be obtained. For many applications, however, it is not only radiation measurement that is of interest, but particularly imaging. While this is possible with current quantum ghost imaging (QGI) setups [12], their application is limited.

The main limitation of current QGI setups is the camera technology used to capture image information. The fundamental problem is that high-resolution, single-photon-sensitive cameras are currently only available in "gated" configurations. To operate QGI, the photon interacting with the object must first be measured to activate the camera and measure the imaging photon. Since the idler photon "announces" the imaging photon, this system is also called "heralded" QGI. However, this means the imaging photon can only be detected after the idler photon has been detected and must be delayed accordingly. During this delay, the image information of the signal photon must be preserved, which makes the use of optical fibers impossible. Instead, a free-space delay line consisting of mirrors and finely tuned imaging lenses must be constructed to compensate for the camera delay. Due to this delay line and its corresponding alignment, heralded QGI can only be applied in transmission or controlled environments and is thus only marginally suitable for remote sensing.

Recent developments, particularly in the field of SPAD technology [24–29], and dedicated readout technology [30, 31], however, allow for the development of new cameras that can measure individual photons not only spatially but also temporally. Initially intended for use in LiDAR [32] and positron emission tomography (PET) [33], these detectors are increasingly

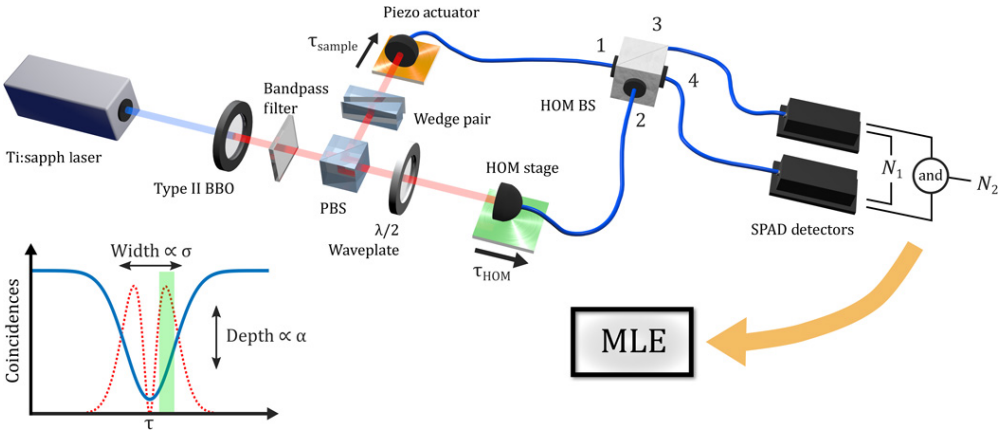

Figure 1.3: Coincidence-based depth determination using a Hong-Ou-Mandel interferometer. The setup is taken from [37].

being used to identify entangled photons [34–36]. These cameras register all incoming photons and identify related photon pairs based on their timestamps, or time of flight. Unlike heralded imaging, the coincidence detection of the systems is no longer determined by the geometry of the setup but can be evaluated from the data after measurement.

The use of a single, typically gated, detector significantly limits these systems, especially spectrally, as a uniform material system is required. However, QGI allows for the separation of an object's illumination from its imaging by synchronizing two detectors. In this work, a system is presented that achieves this synchronization not through the geometry of its setup, but by comparing the timestamps of two separate detectors. This allows QGI to be realized without predefining the time window for coincidence evaluation, eliminating the need for an (image-preserving) delay line. Instead, the coincidence time window can be freely chosen after the measurement data has been evaluated. This not only makes the delay line obsolete and enables application in remote sensing, but also allows for the determination of the flight time of the interacting photon. In reflection mode, this enables the depth determination of the investigated object or the 3D imaging of a scene. Since the detectors in this method operate independently of each other and do not need to be synchronized, it has been named "asynchronous quantum ghost imaging".

Brief Overview

To place this method in the current state of research, Chapter 2 first provides a general overview of setups for remote sensing, particularly the closely related field of single-pixel imaging. Then, the components used in this work are presented, starting with the entangled photon pair sources based on parametric fluorescence (SPDC) and the manipulation of their parameters through periodic poling of nonlinear crystals (QPM). The basics of QGI in general and asynchronous detection in particular are then discussed, followed by the single photon avalanche diode (SPAD) technology used for imaging, its properties, and current issues. Finally, the evaluation of the measurement data and the associated challenges are discussed.

The results of this work are summarized in Chapter 3, beginning with a detailed description of the photon pair sources and detectors used. Then, the necessary data corrections are addressed, explaining both their reasons and implementation, depending on the hardware setup of the camera. The results of this work are then presented, including already published results on transmission imaging [38] and 3D imaging [39], as well as investigations on the influence of the source on image resolution and the spectroscopic application of the method. Finally, a brief discussion is given on the use of evolutionary algorithms for evaluating the measurement data and reconstructing the object.

Due to the significant delays in the planned camera development caused by the COVID-19 pandemic, possible further developments of the asynchronous method and the corresponding boundary conditions were also examined in this work. The results of these investigations are summarized in Chapter 4, focusing particularly on the acquisition of spectroscopic information. This chapter also addresses current developments in detector technology, especially SPAD technology in general and SPAD cameras in particular. Since this technology will remain limited for the foreseeable future, particularly in the IR range beyond $1.7\ \mu\mathrm{m}$, other potential single-photon detectors or detection methods are also described.

Chapter 5 provides a summary of the findings of this work.

2 Theoretical Foundations

This chapter explains the basic principles of remote sensing, both classical and quantum, with special emphasis on ghost imaging. Section 2.1 first addresses the fundamentals of long-distance imaging. Next, Section 2.2 focuses on single-pixel imaging using structured light, while Section 2.3 describes imaging with entangled light, with particular attention to parametric fluorescence in nonlinear crystals (SPDC), the most commonly used physical effect for generating entangled photon pairs (Section 2.3.1). The influence of phase matching in these crystals, enabled by manipulating the nonlinear crystal to achieve almost free wavelength selection, is also discussed (Section 2.3.2).

The following Section 2.4 covers the main topic of this thesis, Quantum Ghost Imaging (QGI), detailing the fundamentals and limitations of the method, depending on the previously outlined physical and technical conditions. Subsection 2.4.2 briefly introduces the asynchronous QGI approach developed in this work, which is described in more detail in Chapter 3.

The time-resolved single-photon detection using SPAD (single photon avalanche diode) technology, utilized in the asynchronous approach, is discussed in Section 2.5. Finally, Section 2.6 describes noise influences relevant to QGI and possible improvements in contrast and 3D imaging. Optimization algorithms, particularly evolutionary algorithms investigated in this work for 3D imaging, are also addressed.

2.1 (Active) remote sensing

Remote sensing refers to the measurement and interpretation of radiation, usually electromagnetic, emitted by an object that is not directly accessible. Detection of the object occurs without direct contact. This radiation may come from the object itself, as in spectroscopic or astronomical applications, or be reflected or scattered by the object, as in photography. The techniques are divided into two groups: those in which the object is actively irradiated and those that measure the radiation passively emitted by the object. Passive

techniques, which generally utilize scattered radiation from distant stars or blackbody radiation as per Planck's law, are not covered in this work; further information can be found in specialized literature, such as [40].

This work focuses exclusively on active remote sensing methods for imaging, particularly single-pixel imaging, where a non-spatially resolving detector is used. Since this work compares the characteristics and peculiarities of various active systems, the following section briefly discusses the most well-known active remote sensing methods and their fundamental principles.

In active remote sensing, the object under investigation is illuminated by a radiation source directed at the object, after which the radiation scattered, reflected, or transmitted by the object is measured by one or more detectors. In transmission, the detectors are usually aligned optically with both the object and the radiation source, maximizing detection efficiency (DE). In reflection, it is often preferable to position the detector near the radiation source to enable compact systems.

2.1.1 Lidar

LiDAR is a general term for the most widely used active remote sensing setups. The acronym stands for "'**Li**ght **D**etection **A**nd **R**anging,"' similar to radar. It is used for various setups that extract depth information about an object from the properties of light reflected from the object. The most common are time-of-flight (ToF) systems, which use a pulsed laser and measure the time difference between the emission of the pulse and the detection of the reflected light. Using this so-called flight time difference, the distance between the source and the object can be determined based on the speed of light:

$$d = \frac{1}{2} \frac{c}{n_{\text{Medium}}} t_{\text{Pulse}}. \tag{2.1}$$

where c is the speed of light in a vacuum, t_{Pulse} is the time difference, and n_{Medium} is the refractive index of the medium through which the light pulse travels. The factor $\frac{1}{2}$ accounts for the round trip of the light pulse to the object.

Since the Maxwell equations underlying radar are linear, the basic principles can be transferred from radar to lidar in a first approximation. However, the significantly smaller wavelength in lidar requires a more differentiated approach. The interaction with the object can no longer be approximated as reflection by an antenna without absorption; instead, it must be considered a complex, wavelength-dependent scattering on the surface structure of the object. Thus, the radar equation changes to the lidar equation, used to characterize and evaluate a system: [41]

$$P(R) = KG(R)\beta(R,\lambda)T(R,\lambda) \tag{2.2}$$

$$K = P_0 \frac{c\tau}{2} A\eta \tag{2.3}$$

$$G(R) = \frac{O(R)}{R^2} \tag{2.4}$$

$$T(R,\lambda) = \exp\left[-2\int_0^R \alpha(r,\lambda)dr\right] \tag{2.5}$$

where the received power $P(R)$ depends on the system constant K, the distance function $G(R)$, the backscatter coefficient $\beta(R,\lambda)$, and a transmission term $T(R,\lambda)$. The system constant K depends on laser power P_0 and pulse duration τ, the size of the receiving optics A, and the system or detection efficiency η. The distance function combines the overlap of the sender's field of view with the object over the overlap function $O(R)$, and is weighted by R^2, which accounts for the general distance dependence of reflection. The overlap function itself depends on the distance, as the spot of the light increases with distance. Assuming the illumination spot is larger than the object itself, as is usually the case, the function depends on the spot's magnification, which is proportional to the square of the distance. The factor $\beta(R,\lambda)$ is the backscatter coefficient, describing the effect of surface structure and optical properties of the object. The last factor $T(R)$, the transmission term, generally accounts for the effect of the transmission path by integrating the extinction coefficient α, which describes both absorption and scattering losses along the optical path.

The main advantages of lidar compared to radar lie in the significantly smaller wavelength, which greatly reduces the fundamental diffraction limit:

$$\delta = \sin^{-1}\left(1.22\frac{\lambda}{D}\right) \tag{2.6}$$

where δ is the minimum resolvable angle and D is the aperture diameter of the system. This results in significantly better spatial resolution for a lidar system compared to a radar system of similar size, making lidar ideal for miniaturized, local ranging applications. Additionally, the coherence of laser light, combined with reduced diffraction, allows the source radiation to be more directed, making it more efficient for targeting a specific object.

This improved angular resolution enables spatially resolved lidar setups to quickly and efficiently scan arbitrary scenes. Depending on the application, there are various ways to achieve the corresponding spatial resolution, but laser scanners and time-resolved cameras or sensor arrays are the most common. Cameras or arrays have the advantage that a complex scene can be captured with a single measurement (so-called flash-lidar). This is especially advantageous for fast-changing and complex scenes, such as

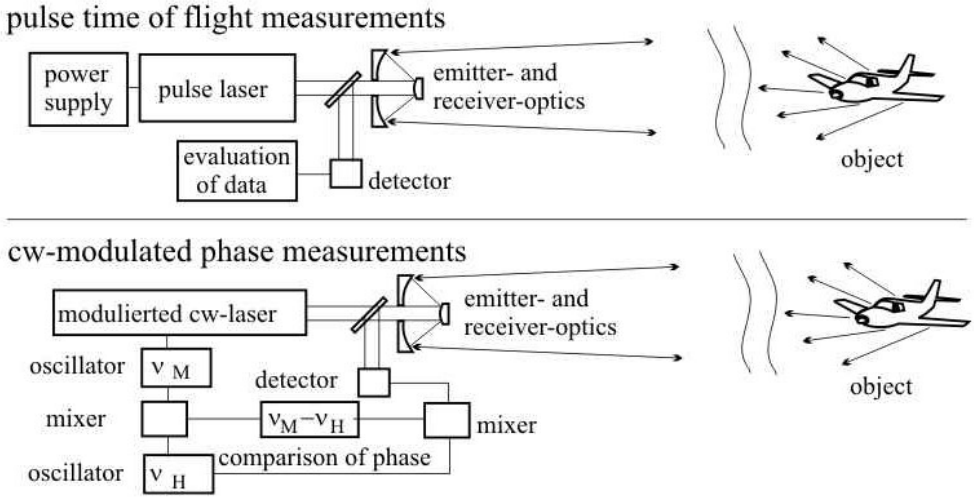

Figure 2.1: Examples of setups for Time-of-Flight measurement and phase comparison with modulated cw lasers. Pulsed ToF systems emit a laser pulse and record its emission time. The backscattering is also recorded in time and compared with the emission time, allowing the depth of the backscatter to be determined. In modulated laser systems, the backscattered radiation is superimposed with the emitted laser. Depth is then determined by the interference of both signals and depends on their phase relation. Due to the periodicity of the phase with 2π, depth determination is ambiguous, but this can be resolved, for example, through coarse determination based on ToF or by multiple modulation of the laser signal. The images are taken from [42].

those often encountered in traffic. However, these systems can be quite complex and costly, depending on the application. For static scenes where capturing motion is not crucial, scanners, which can capture complex scenes with very affordable components, have become more common. This is the case, for example, with many commercial robots, including both autonomous warehouse robots and vacuum cleaner robots.

However, since power decreases with the fourth power of distance (see Equation 2.4, where $O(R)$ also scales with $1/R^2$), the power of the transmitter must be scaled according to the application. At greater distances, this leads to significant problems regarding eye safety. Up to $1.4\ \mu\mathrm{m}$, the maximum permissible power is 5 mW, while in the mid and far-infrared regions, the thresholds are about 100,000 times higher [43]. As a result, the use of advanced silicon cameras, which are sensitive up to about $1\ \mu\mathrm{m}$, is limited to short distances ($\sim 1\ \mathrm{km}$ [44]) without appropriate safety measures. Imaging in the "eye-safe" infrared range (e.g., using InGaAs cameras) allows the use of higher powers compared to silicon-based systems, but this power is often needed due to the lower photon energy of longer-wavelength photons, which results in higher background noise [45]. Corresponding technologies are also less developed than silicon-based technologies. Nevertheless, with these cameras, the maximum range can be increased to several kilometers [46].

In addition to these pulsed time-of-flight systems, there are also cw-lidar systems, which do not measure the time-of-flight of a laser pulse but rather modulate a cw-laser and compare the phase of the emitted and backscattered light by superimposing the signals on a suitable detector (see Figure 2.1). The depth determination in this method suffers from the periodicity of the phase, leading to ambiguities in the measurement. However, appropriate methods, such as multiple modulations of the light, can improve or eliminate this issue. Since these setups are generally less relevant in remote sensing, they are not further discussed in this work. Further details can be found in the relevant literature, e.g., [42, 47].

2.1.2 Gated Viewing

Gated Viewing is a tomography technique related to lidar, enabling scenes to be captured at user-defined distances. The principle is based on a camera that is activated at precisely defined time intervals and does not register light outside these intervals. This camera is coupled with a pulsed laser, so the laser pulse and the camera's active time window are temporally offset by a specific user-selected delay. This temporal offset corresponds, due to the photon travel time, to a specific distance:

$$d = \frac{1}{2}\frac{c}{n_{\text{Medium}}}(t_{\text{Camera}} - t_{\text{Laser}}). \tag{2.7}$$

where t_{Camera} is the time at which the camera opens, and t_{Laser} is the time of the laser pulse emis-

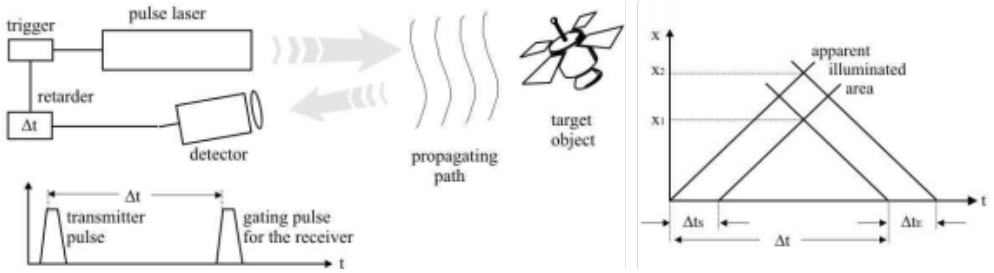

Figure 2.2: Setup for Gated Viewing and diagram for determining image depth, depending on signal delay and pulse length. Only the image section in the marked area can be captured. If objects in front of this area block the emission, they appear as shadow silhouettes [48]. The images are taken from [42].

sion.

This technique was developed to image scenes in highly scattering environments and to minimize unwanted background radiation. Conventional imaging is often subject to the problem of glare, where light produced or scattered by these environments saturates the detector so that the desired information is lost in this background signal and can no longer be detected. Gated Viewing uses the camera's shutter mechanism to ignore any light reflected or produced before or after the desired distance. This allows imaging through smoke walls [49] or imaging underwater objects beyond the classical water sightline [50].

Due to technical limitations, the depth to be imaged is not infinitely narrow. The achievable depth resolution primarily depends on the pulse duration of the laser and the camera's shutter speed, as shown by Equation 2.8.

$$\Delta x = \frac{1}{2}\frac{c}{n_{\text{Medium}}}(\Delta t_{\text{Camera}} + \Delta t_{\text{Laser}}). \tag{2.8}$$

where Δt represents the pulse width of the laser or the camera's shutter time. The laser pulse width can usually be neglected, as simple commercial lasers already achieve pulse widths in the picosecond to single nanosecond range. Camera technology, on the other hand, typically has shutter times in the hundreds of nanoseconds, which limits the resolution. In air, a shutter time of 100 nanoseconds corresponds to a depth resolution of 15 meters according to Equation 2.8. To improve this resolution, specialized cameras (e.g., ICCDs or time-resolved detectors, see 2.5.2) can be used, or multiple images can be taken at different depths by varying the temporal offset between the camera and laser, allowing depth resolution to be improved through multi-frame analysis [51].

2.2 Single-Pixel Imaging

Single-pixel imaging refers to any imaging method that uses a non-spatially resolving detector to capture spatially resolved images. There are three basic approaches:

Scanning: The scene/object is illuminated point-by-point. The single-pixel detector records the backscatter from each point, producing a single pixel of the overall image.[1] This process is repeated for each desired point in the image/scene, creating the overall image. A classical example of such a setup is a laser scanner.

Correlated light: The entire scene is illuminated with a light spot whose spatial structure is correlated with light in a spatially separate "second arm." By capturing the second arm's spatial distribution, e.g., using a camera, the spatial distribution of the emitted light can be inferred. The single-pixel detector captures the backscattered light from the scene and provides a grayscale value representing the correlation factor between the scene and the light structure. By varying the light structure, e.g., by transmitting through a rotating scatter plate, the various structures can be compounded, weighted by the corresponding correlation factor. A successive image of the scene is reconstructed.

Structured light: This technique is closely related to correlated light but does not use correlated light to determine the structure of the illuminating light spot. Instead, the light is modulated with appropriate spatial light modulators (SLM), such as digital micromirror arrays (DMDs) or liquid crystal displays (LCDs), with adjustable structures. The single-pixel detector measures a correlation factor, similar to correlated light, which weights the respective structures in the reconstruction process. It does not matter whether the spatial structure is imprinted before or after interacting with the scene.

The following sections focus on the basics of scanning, using a laser scanner as an example, and imaging with structured light. Since the principles of correlated light are analogous to those of structured light, correlated light is not discussed in detail.

2.2.1 Laser Scanner

As previously mentioned, a laser scanner sequentially illuminates individual points in the scene and measures the corresponding backscatter. After scanning all points, the intensity of the backscatter is normalized, defining a grayscale value for each pixel, which can be used to create a grayscale im-

[1] In modern systems, the distance is also determined by time-of-flight, providing not just a one-dimensional pixel but a "voxel," or a point in a 3D scene.

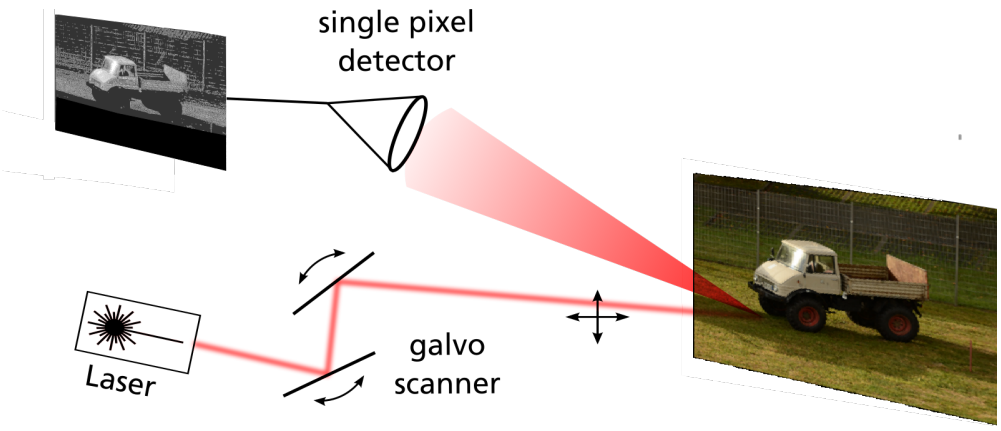

Figure 2.3: Laser scanner setup with two galvo mirrors. The laser is collimated and sequentially deflected by rotating the galvo mirrors. Each point in the scene is scanned, and the backscatter from each point is measured by a single-pixel detector. The grayscale values from each measurement can be used to reconstruct an image of the scene. Modern systems also use the time-of-flight of photons to obtain depth information and create a 3D image of the scene.

age.

Depending on the application, there are various ways to direct the laser beam and scan the scene. However, all common models use at least one mirror. Since this work focuses on imaging distant scenes, the principle is explained in Figure 2.3 using a two-mirror scan head, which is commonly used in controlled environments. However, the fundamentals also apply to one-dimensional line scanners or rotation-based scanners, provided the coordinate systems and boundary conditions are adjusted accordingly.

To scan the scene as accurately as possible, the laser is collimated to a small emission point. Collimation is necessary to prevent pixel size from varying with depth due to spot magnification. The spot is then directed to a specific point using an optical system (two galvo mirrors in Figure 2.3), and the backscattered light is measured by a simple single-pixel detector. The strength of this backscatter is then converted into a grayscale value for the illuminated point or pixel in the resulting image. Afterward, the laser point is deflected to another point in the scene using the optical system, and the measurement is repeated. The scene is scanned point-by-point, building up the image.

Modern systems additionally use pulsed lasers and time-resolved detection, allowing the 3D structure of the scene to be reconstructed using the photons' time-of-flight. Pixel size depends on the laser's finite divergence, pixel depth, and transmission path, but these parameters can be improved with stable scanning setups

and over-sampling through multi-frame analysis, similar to Gated Viewing [52].

2.2.2 Imaging with Structured Light

Imaging with structured light (also known as Ghost Imaging (GI), Compressive Sensing (CS), or Computational Imaging (CI), depending on the implementation) is similar to laser scanning but does not scan the scene point by point. Instead, the entire scene is illuminated with each pulse. Early experiments with ghost imaging used lasers transmitted through a rotating scatter plate, with a beam splitter directing part of the light to a camera and the other part to the object [53, 54]. The illuminated pattern was registered by the camera and could be compunded with previous patterns, resulting in an image of the scene. Since this method requires a camera at the desired wavelength and the patterns could not be actively adapted, it has largely been replaced by Compressive Sensing (also known as "Computational Ghost Imaging"). Here, light formers such as spatial light modulators (SLMs) or digital micromirror devices (DMDs) are used to actively imprint a desired structure on the light spot [55]. This approach has the advantage of allowing the reference patterns to be tailored to the application and optimized for subsequent mathematical processing [56, 57].

The spatial structure of the emitted light is thus known to the receiver and is projected onto the scene, changing with each new pulse. The single-pixel detector also measures a grayscale value, but instead of correlating between the laser spot and the scanned point, this value represents a correlation factor between the entire scene and the structure. Alternatively, the receiver can first illuminate the object and superimpose the scattered light with the known structure before measuring the correlation factor, rather than projecting the structure onto the object.

It is crucial that the light structure on the object, or the image of the object on the light former, is correctly mapped to maintain the correlation between the object and the structure. For example, if the image of the object is blurred, the measured grayscale value only reflects the correlation of the blurred image with the structure, resulting in a blurred reconstructed image. Moreover, the light falling on the SLM/ the object typically has a specific structure. Since lasers are generally used for illumination, the Gaussian distribution of light across the SLM and influences from speckle patterns should be considered.

The term compressive sensing comes from signal processing and generally refers to techniques for efficiently acquiring and reconstructing signals by finding solutions to underdetermined linear systems. The foundation of this approach is the assumption that the signal to be reconstructed is sparse. If this sparsity condition is not met, NxM measurements would be required to reconstruct an NxM-pixel image. However, due to the redundancy introduced by sparsity, such signals can be compressed without significant information loss. This principle is used, for example, in modern cameras, where the original raw data can be significantly reduced using encoding standards like JPEG.

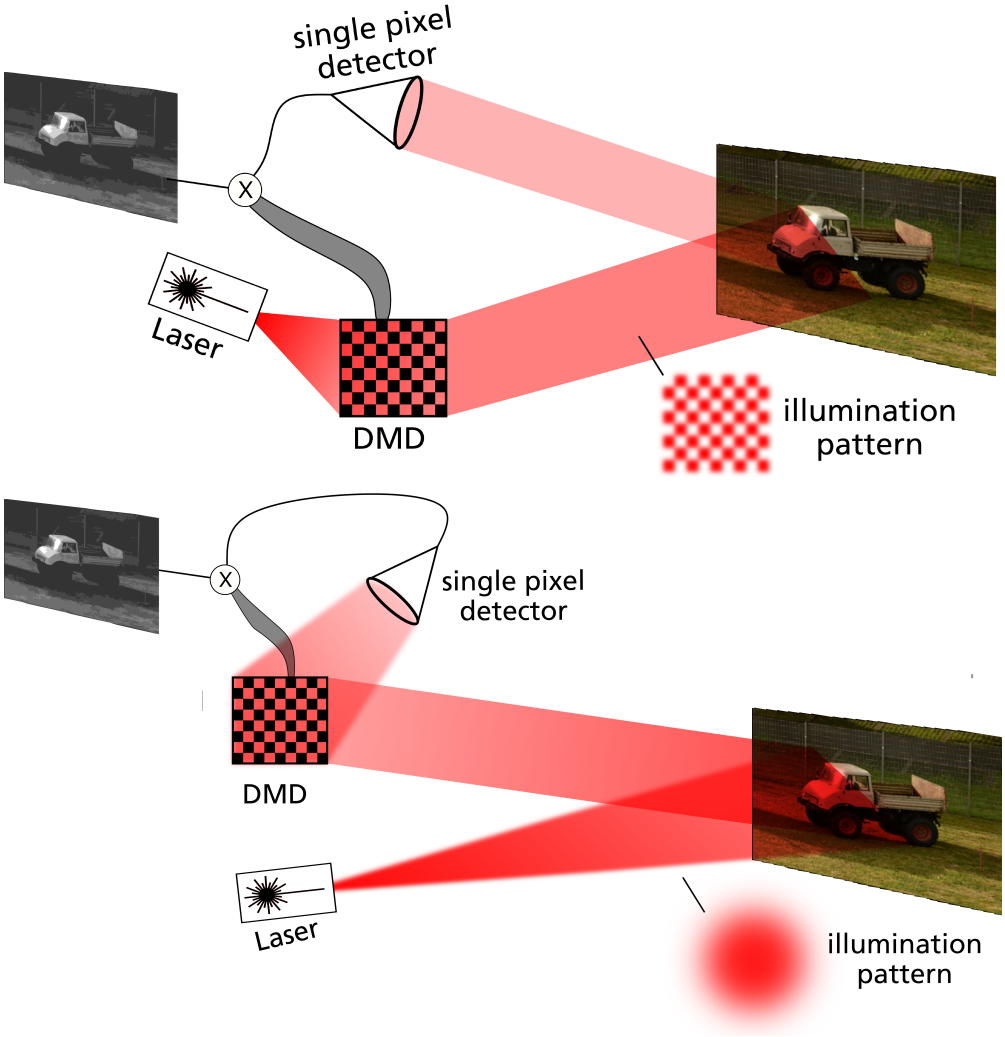

Figure 2.4: Compressive Sensing (Computational Ghost Imaging) setups. A spatial structure is imprinted on a laser beam using an SLM, and the scene is illuminated with this structured light. The scene's backscatter is recorded by a simple single-pixel detector, which provides a grayscale value representing a correlation factor between the illuminated structure and the scene. The structure is successively changed, and the correlation factors are combined, weighted accordingly, to reconstruct an image of the scene. The light structure can be imprinted before or after interaction with the scene. These setups typically require significantly fewer measurements and less laser power than comparable laser scanners.

Compressive sensing systems exploit the redundancy of the signal to reduce the hardware requirements. This allows for the use of simpler and therefore cheaper cameras or the potential reduction of power consumption. This is especially interesting for spectral ranges where no dedicated camera technology is currently available, as these systems can avoid the highly cost-intensive development of corresponding cameras.

Reconstructing the object requires corresponding matrix operations, which can be quite complex depending on the matrices and resolution involved. Therefore, Hadamard matrices, in which all rows and columns are orthogonal to each other, are commonly used, simplifying the computation of the image [58]. These matrices can be constructed for all $n \times n$ resolutions when n is a power of two. Additionally, the sequence and form of the matrices can be adapted to a specific application, allowing, for example, certain parts of the scene to be scanned in higher detail [56]. This enables object detection and tracking to significantly increase the frame rate without compromising the target object's resolution.

2.3 Imaging with Entangled Light

Imaging with entangled light is closely related to imaging with correlated light, but here the correlations between two entangled photons or the interference between entangled photon pairs are utilized. Instead of measuring a grayscale value and using it as a weighting factor for the macroscopic light structure, the direct point-to-point correlation of the photons is used to obtain image information. There are two principal ways of realizing imaging with entangled light.

Either the photons are individually detected, and their entangled partners are identified using specific correlations, or the partners are superimposed with other entangled photons in the same spectrum. The latter case uses two identical photon pair sources (A and B) to produce two separate but interferable photon pairs (A1 and A2, B1 and B2).

The photons from one source (A1) interact with the desired object and are then superimposed with the photons from the other source (B1). Since a spatial structure is imprinted on the photons from A1 by the object, the structure allows for distinguishability in the "which-path information," affecting the interference in this region. Due to the correlation of the photon pairs, this behavior also occurs when superimposing the entangled photons (A2 and B2). As a result, an image of the object examined with A1 is created in the superposition of A2 and B2, enabling imaging without detecting A1 itself. This effect, called "induced coherence," was first demonstrated by Zou et al. [60] and allows imaging without a camera in the spectrum of the interacting photon [8, 17, 18]. However, due to the required superposition of various emissions and its susceptibility to noise, this technique is poorly suited for remote sensing. In particular, the losses associated with remote sensing (see Section 2.1.1) would significantly limit the contrast of the interference

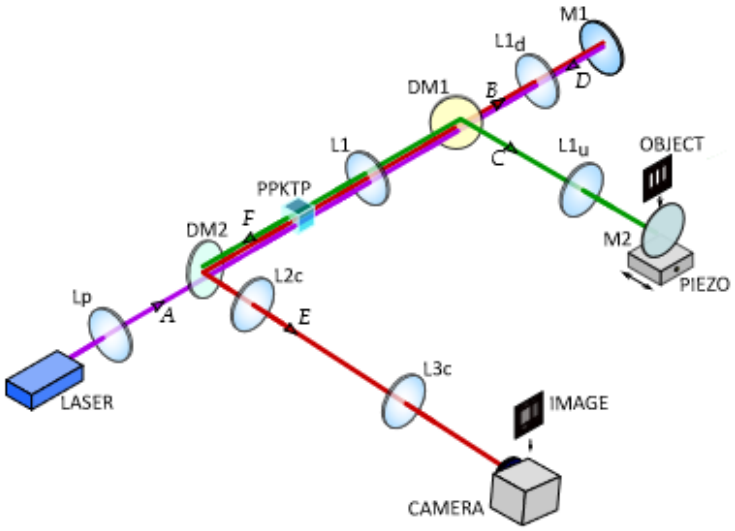

Figure 2.5: Setup for "Imaging with undetected photons," a superposition-based quantum imaging technique. The image information is obtained from the interference of the signal photons (red), not from the idler photons (green) interacting with the sample. The setup is taken from [59].

and thus the visibility of the object.

Therefore, this work focuses solely on the first type of imaging, specifically an effect first demonstrated by Pittman et al. [22] and known as "Quantum Ghost Imaging" (QGI). Although it is the most promising application for remote sensing, it is not the only form of quantum imaging with individual detection. In particular, "superresolution imaging" [34] and "Quantum optical coherence tomography" [10] should also be mentioned, although they are not discussed in detail in this work.

The following section first introduces entanglement in general, and specifically the generation of entangled photon pairs through parametric fluorescence, before describing imaging with QGI.

2.3.1 Spontaneous Parametric Down Conversion

Spontaneous Parametric Down Conversion (SPDC) is a second-order nonlinear optical effect. In a nonlinear medium, typically a crystal, a photon (pump) is converted into two photons (signal and idler). This process is governed by two fundamental physical laws: energy conservation and momentum conservation. Energy conservation determines the wavelengths of the photons involved:

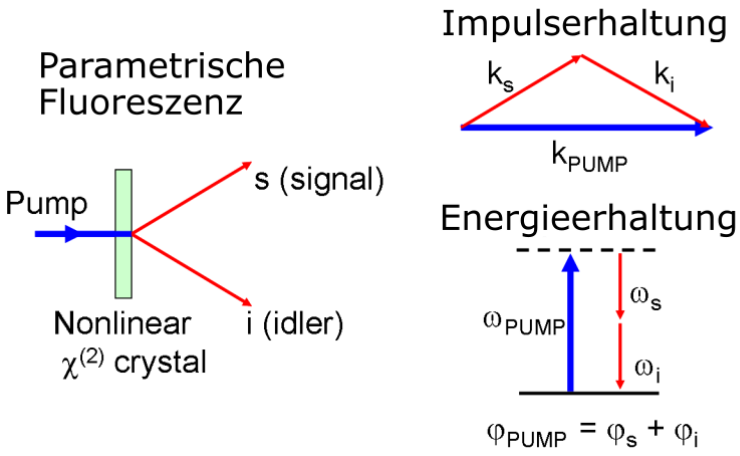

Figure 2.6: Spontaneous Parametric Down Conversion (SPDC). The refractive index, which is generally higher for higher photon energies, leads to momentum conservation only being achievable through an emission angle offset of the photon pairs.

$$\hbar\omega_p = \hbar\omega_s + \hbar\omega_i \tag{2.9}$$

Momentum conservation, in turn, requires the resulting signal and idler photons to have equal momenta:

$$\vec{k}_p = \vec{k}_s + \vec{k}_i \tag{2.10}$$

This condition, the simultaneous fulfillment of energy and momentum conservation, is called phase matching. The wave vector $\vec{k}$ is given by:

$$\vec{k} = \frac{n(\omega)\omega}{c} \tag{2.11}$$

and thus depends on the refractive index at the specific wavelength. Since most materials exhibit normal dispersion, the refractive index for shorter wavelengths (and thus higher photon energies) is generally greater than for longer wavelengths, as shown in Figure 2.7a. Due to this wavelength dependence, the condition for phase matching in isotropic media cannot generally be met, as there is always a mismatch in either photon energy or momentum. Therefore, materials that exhibit birefringence, i.e., materials whose

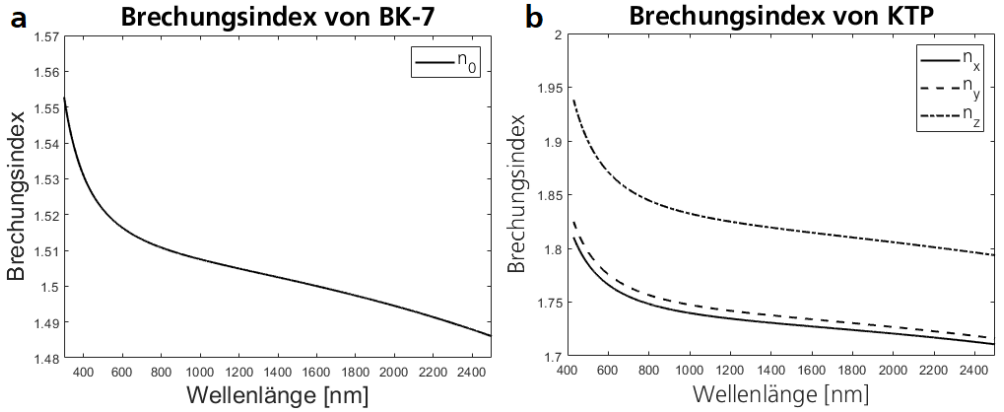

Figure 2.7: Refractive Indices of BK7 and KTP, calculated from their Sellmeier coefficients, taken from [61] (a) Refractive index of BK7, depending on the wavelength of light. Since BK7 glass is an isotropic medium, its refractive index is not dependent on the polarization of the incident light. (b) Refractive index of a KTP crystal, a birefringent material. The refractive index of this material depends on the orientation of the light's polarization relative to the crystalline structure of the KTP crystal.

refractive index depends on the polarization of light relative to the crystal orientation, are used to realize this effect. Phase matching is then achieved by polarizing one of the photons orthogonal to the other two, subjecting it to a different refractive index, as shown in Figure 2.7b. This leads to two main types of phase matching, depending on how the polarization of the generated photons is oriented relative to each other. In Type-1 phase matching, the resulting photon pair is orthogonally polarized, while in Type-2 phase matching, the pair shows parallel polarization.

Through careful selection of the crystal material, its orientation, and control of the pump light, various parameters of the photon correlation can be manipulated [62]. In particular, phase matching can be realized over a broad range of wavelengths, making this effect adaptable to many applications. This spectrum can even be deliberately shifted and finely tuned due to the temperature dependence of the refractive index by adjusting the crystal temperature [63].

The width of the emitted spectrum, however, strongly depends on the length of the crystal, as this significantly influences the phase matching. For a general photon triplet, the phase mismatch can be calculated using $\Delta k = k_{pump} - k_{signal} - k_{idler}$ (see Equation 2.10). This mismatch leads to a "rotation" of the nonlinear tensor in the complex phase space. Once a rotation of π is reached, this rotation causes destructive interference of its components, and after a rotation of 2π, the components effectively cancel each other out. Therefore, a so-called coherence length can be defined, up to which the components add constructively:

$$L_c = \frac{\pi}{\Delta k} \tag{2.12}$$

Beyond this coherence length, destructive interference begins, which suppresses the SPDC process. If the SPDC crystal is longer than the coherence length of the phase mismatch, the SPDC process is suppressed at the corresponding wavelengths. Consequently, the possible phase mismatch $\Delta k = \frac{\pi}{L_{crystal}}$ is significantly smaller for long crystals than for short ones, resulting in a narrower SPDC spectrum. A more detailed derivation of these relationships can be found in [64].

This behavior can, however, also be utilized to manipulate the crystal and achieve specific desired phase matchings. One widely used technique is periodic poling of the crystal, in which the crystal orientation is periodically inverted. This inverts the nonlinear tensor of the medium locally, changing the sign of its rotation. By periodically inverting after the coherence length L_c, the destructive interference that begins there is transformed into constructive interference. This makes phase matching possible for wavelength combinations that would otherwise be impossible in a uniformly oriented crystal. Of particular interest is the normally impossible Type-0 phase matching, where the pump, signal, and idler photons are all polarized in parallel. This topic is discussed in more detail in subsection 2.3.2.

Unlike the regular fluorescence used for lasers, there are no energy states of the medium excited in SPDC, which would typically decay radiatively after a certain time (fluorescence lifetime). Instead, the pump photon decays directly, generating the signal and idler photons simultaneously. Additionally, since the system is not bound to fixed, material-dependent energy levels and differences, a much broader spectrum can be emitted than with a fluorescence-based laser [65].

Although intensive quantum mechanical and electrodynamic analyses have already derived mechanisms in which the time and location of the partners do not coincide [66, 67], these considerations are omitted in this work, as their likelihood of occurrence is very small compared to regular SPDC due to the involved side effects. However, this nonlocality limits the fidelity of the entanglement, which, for example, limits quantum communication systems like Quantum Key Distribution (QKD). For imaging applications, depending on the system, this nonlocality could lead to additional noise or limit the achievable resolution. In coincidence-based measurements, the influence of these effects is especially questionable, as the temporal coincidence used to identify photon pairs could also be used to filter out these (in part) temporally nonlocal pairs.

2.3.2 Quasi-Phase Matching

Quasi-phase matching (QPM) describes a method for manipulating phase matching by introducing a periodic structure into the nonlinear medium. This structure is usually created by periodic poling of the

crystal, i.e., by periodically inverting its ferroelectric domains. This leads to a periodic inversion of the sign of the nonlinear coefficient [68] and, consequently, a periodic inversion of the corresponding tensor. The structuring can be achieved through several methods, but the most common is poling with strong, localized electric fields. This method is also used to align other optical materials, such as polymers [69, 70].

The required structure can be determined by the phase mismatch of the photon triplet,[1] given by the refractive indices at the desired wavelengths and polarizations. After a certain coherence length L_c, this mismatch corresponds exactly to π (see also Equation 2.12). In an unmodified crystal, the complex nonlinear tensor would begin to interfere destructively after this length, suppressing the nonlinear process. By inverting the crystal structure after this coherence length, the sign of the nonlinear coefficient is reversed, changing the destructive interference into constructive interference [70]. As a result, phase matching for wavelength combinations that are impossible in a uniformly oriented crystal can be achieved. The possible periods of the structure can be calculated by:

$$\Lambda = 2mL_c \tag{2.13}$$

where $m = 1, 3, 5, ...$ is the order of the matching and ensures that constructive interference is achieved. Several possible periods can be derived from this equation, but higher-order matching generally leads to lower conversion efficiencies, as also destructive interference of the nonlinear tensor occurs at these orders. Higher-order matching, however, can be advantageous in realizing the poling process, as larger structures are generally easier and more reliably fabricated.

This behavior is shown in Figure 2.8, but for a sum-frequency generation (SFG) process rather than parametric fluorescence. The behavior is comparable, but the intensity in SPDC does not follow an exponential curve as in SFG but rather a linear relationship. This is due to the spontaneous generation rather than the stimulated generation used in SFG. However, the generation of photon pairs still follows a sinusoidal pattern, as it is described by a projection of the rotating optical tensor in phase space. Therefore, the effective nonlinear coefficient in quasi-phase matching is also limited to $2/\pi$ of the actual nonlinear coefficient.

The influence of the periodic structure on the phase matching can be described by an additional wave vector k_Λ. By carefully adjusting this, a structure can theoretically be found for any photon triplet that satisfies energy conservation and ensures that momentum conservation, and thus phase matching, is achieved. This also allows for a wide variety of wavelength combinations with freely chosen types of phase matching. For instance, collinear Type-0 phase matching can be achieved, where the pump, signal, and idler photons all have the same polarization and are emitted collinearly. This type of matching allows the use of the

[1] see Equations 2.9, 2.10, and 2.12

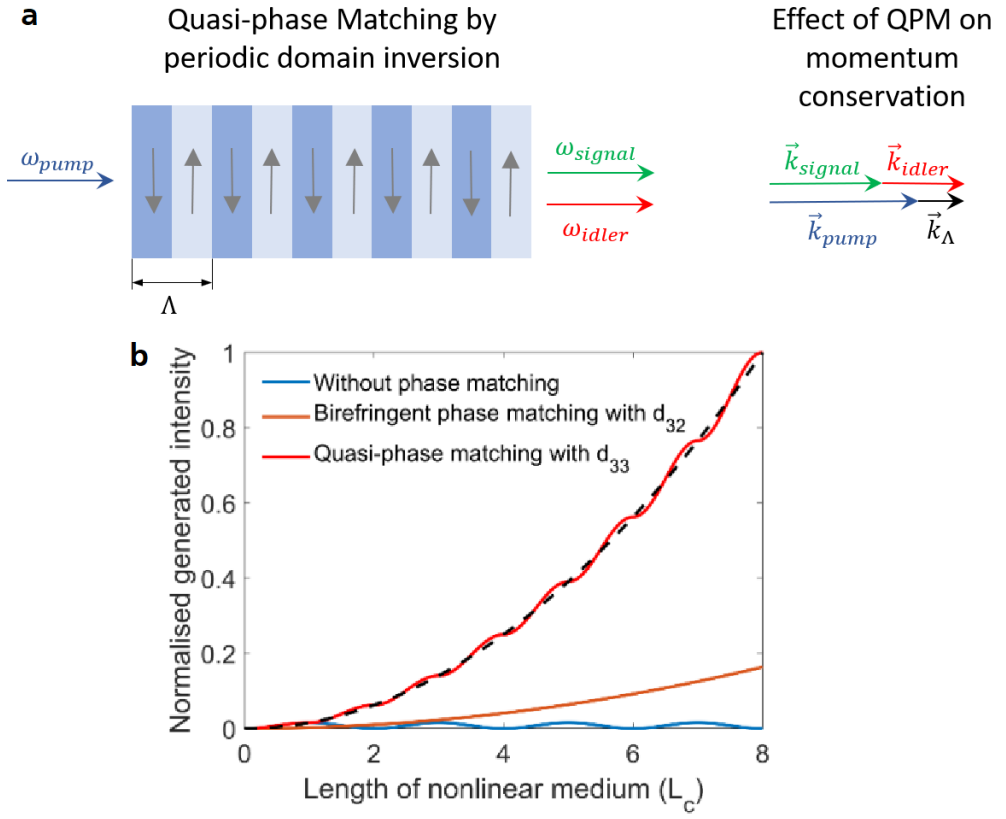

Figure 2.8: Quasi-phase matching and its influence on phase matching. (a) Quasi-phase matching structure in a nonlinear crystal. The orientation of the crystal domains is periodically inverted. Next to it: the influence of the structure on phase matching (collinear phase matching), expressed by the wave vector k_Λ. (b) Intensity of sum-frequency generation (SFG) for different phase matchings. The behavior is comparable to phase matching in SPDC. Blue: intensity without phase matching, orange: natural angular phase matching via the d_{32} coefficient, red: quasi-phase matching via the d_{33} coefficient. Image taken from [71].

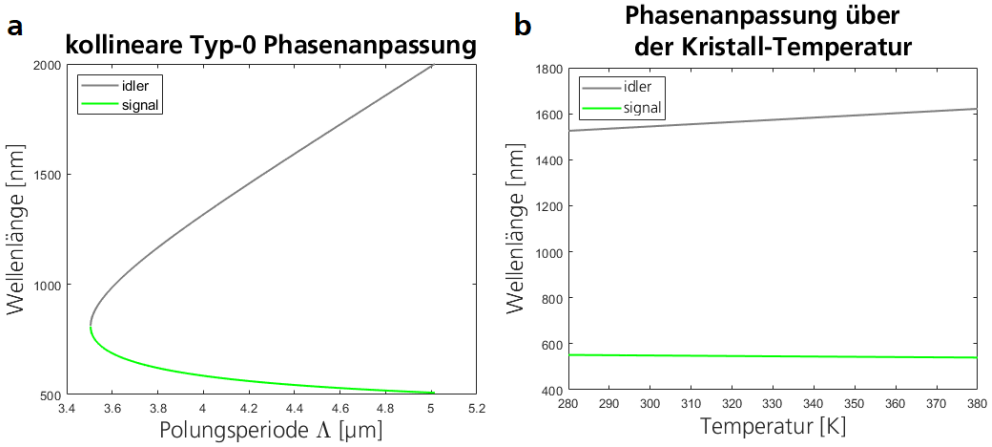

Figure 2.9: Influence of poling period and crystal temperature on phase matching, demonstrated with collinear Type-0 phase matching. (a) Influence of poling period on the wavelengths of collinearly emitted photon pairs from a KTP crystal. A 405 nm laser and a crystal temperature of $20°\mathrm{C}$ are assumed. (b) Influence of crystal temperature on the wavelengths of collinearly emitted photon pairs from a KTP crystal with a $4.25;\mu m$ period, at a pump wavelength of 405 nm. Data calculated with SNLO [78], based on measurements in [79].

d_{33} nonlinearity, which is particularly large in some nonlinear materials, promising higher conversion efficiencies (e.g., [72]).

Furthermore, phase matching can be achieved over a broad spectrum of wavelengths and combinations. Of particular interest for metrology is the entanglement of light in the visible spectrum (detectable by silicon, $< 1.1\mu m$) with light in the wavelength range where the measurement is to be conducted. This spectrum can be selected from the visible range [73] to the infrared [16, 74] and even up to the THz range [75]. However, for extremely long wavelengths (or low photon energies), the separation of the pump and signal photons becomes increasingly difficult due to the small wavelength difference [76].

Of course, the quality and "purity" of the periodic structure also play a crucial role. The biggest limitation for spectroscopic applications is the absorption of the nonlinear medium itself—not because phase matching in that spectrum would be impossible, but because the corresponding photon might be absorbed within the medium itself, rendering it unusable for measurement. Techniques such as using short crystals [77] can extend this range slightly, but it remains limited for most applications.

Even for periodically poled crystals, the emitted spectrum can be finely adjusted, especially through temperature tuning. However the intrinsic material parameters are less important for these crystals. Instead,

the emission is mainly affected by changes in the periodic structure. As the crystal expands thermally, this structure is stretched, and phase matching shifts to other photon triplets with the corresponding coherence lengths [69].

Of particular interest in metrology is the aperiodic poling of nonlinear crystals. In this case, the poling period of the crystal is not constant but changes along the length of the crystal. The resulting "chirped gratings" shift phase matching to new triplets continuously, allowing the design of ultra-broadband sources with a wide emission spectrum. This can be used, for example, to increase the number of modes at a given wavelength or to shorten the temporal correlation of the photon pairs [80–82].

2.4 Quantum Ghost Imaging

Quantum Ghost Imaging (QGI) leverages the strong correlations between pairs of entangled photons to image objects without directly detecting the photon that interacts with the object. This allows imaging at wavelengths where detector technology might be less developed, and can also increase information per photon, enabling sharp images with very few photons [12].

The foundation of QGI lies in the entanglement of position and momentum between the two photons in a pair. Under the right conditions this correlation allows to reconstruct the path of one photon by observing its entangled partner. In other words, by imaging one photon (hereafter called "signal") with a camera, an image of the corresponding partner (hereafter called "idler") can be obtained. By measuring the idler photon that interacts with the object using a bucket detector, the corresponding partner photons can be identified, and an image of the illuminated object can be reconstructed from the detections of the signal photons. To ensure a sharp image, the relationship between both partners must be clear. This results in two principal implementations of the photon source: the "far-field setup" (also known as a lensless setup) and the "near-field setup" (also known as an intermediate image in the crystal), shown in Figure 2.11.

The far-field setup focuses a laser beam into a nonlinear crystal. This focussing limits the generation of photon pairs to the focal region, but the emission angles of the emitted partners are very divergent. The term "lensless" arises because, theoretically, the focused source can act as a point source, allowing imaging without lenses and with extremely large depth of field[1]. In practice, however, imaging and focusing lenses are typically used, as the divergence of the photons is often large (several milliradians), and the apertures of typical single-photon detectors are small (on the order of micrometers).

Alternatively, the near-field setup uses a collimated laser beam to illuminate the entire aperture of the crystal. This generates photon pairs over the entire aperture, but their emission angles are limited. The

[1] similar to a pinhole camera

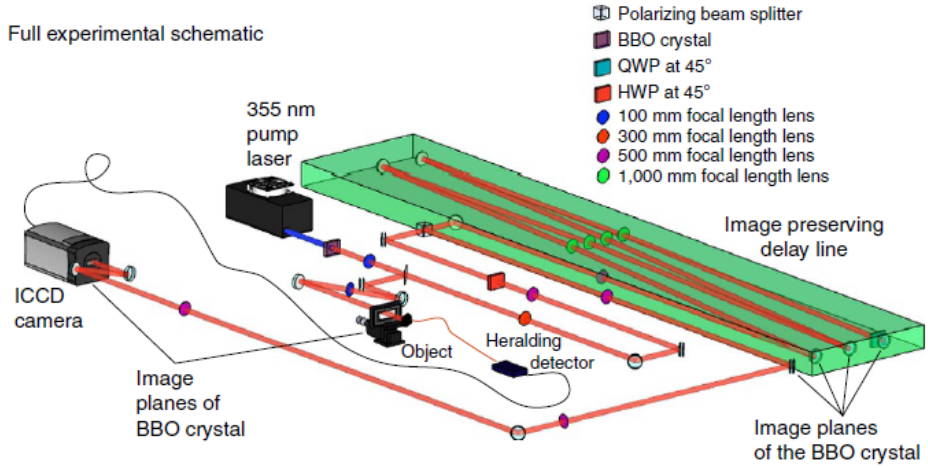

Figure 2.10: Setup for heralded Quantum Ghost Imaging, from [12]. An entangled photon pair is generated and the two partners are separated by their polarization. One partner (idler) is imaged onto the target object and then detected. This detection triggers a camera that spatially resolves the second photon (signal) (The signal photon is "heralded", hence the term "heralded" detection). The signal photon must be delayed to match the timing of the camera's exposure. To ensure a sharp image, the signal photon must be mapped onto the individual mirrors of the delay line to maintain the correlation.

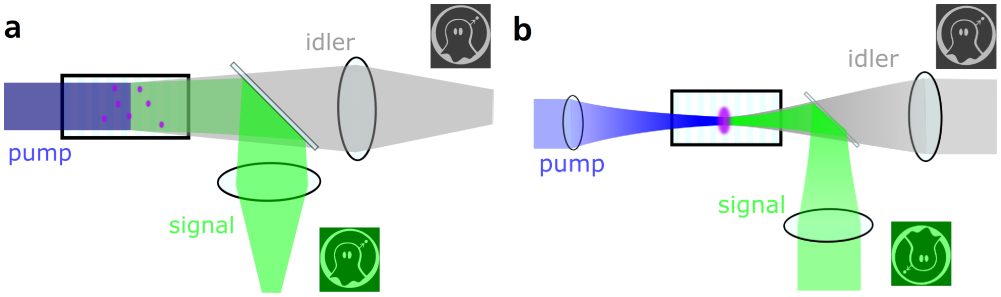

Figure 2.11: The two possible implementations of the photon-pair source and the resulting image correlation. To achieve clear momentum correlation of the photon pairs, plane phase fronts are needed [83], which can be achieved either in a collimated beam or in a focused laser. (a) Near-field setup. The laser is collimated and illuminates the entire aperture of the crystal. The resulting position correlation of the signal and idler photons leads, when imaged on the same plane, to an identical image in both signal and idler. (b) Far-field setup. The laser is focused into the crystal, limiting the emission of photon pairs to a small cross-section. The image is formed using the momentum correlation of the photons, which can be translated into a spatial correlation by collimation. Due to the anti-correlation of the momenta, the resulting image is inverted at the origin, similar to a pinhole camera [84]. For clarity, the crystal in the figure is shown much larger than in reality; for proper imaging, the crystal should be significantly smaller than the Rayleigh length of the laser [85].

resulting image of the "crystal plane" is then projected onto both the object and the detector to reestablish the point-to-point correlation of the entangled photons.

Both setups offer viable methods for QGI, and the choice between them depends largely on their respective advantages and disadvantages. For example, the near-field setup works well with very long crystals, while the lensless setup requires much smaller apertures. In this work, only the lensless setup was used, as the aperture of the crystals used, and thus the resolution achievable with the near-field setup, is limited due to the periodic poling of the crystal.

In the lensless setup, precise control of the laser focus is crucial. There is a trade-off between the size of the focus, which limits the precision of the position correlation, and its divergence, which, along with the length of the crystal, limits the clarity of the momentum correlation. The Rayleigh length of the focus can serve as a measure, which should be kept large in relation to the crystal length [80, 86–88].

Since in practical implementation many individual photons are detected, and it is not known which of the detected photons belong to a particular pair, a system for identifying the partner photons is required. Unlike "classical" quantum mechanical sources such as lasers, where the pump photon excites an energy level of the medium, which, on average, decays radiatively after the fluorescence time, in nonlinear processes, the pump photon interacts directly with the signal and idler photon [71]. Due to this direct interaction

of the radiation, the absorption of the pump radiation and the emission of the signal and idler photons occur instantaneously. In other words, the idler and signal photons are created at the exact same time. This common emission time of both photons is usually used to identify the entangled photon partners through coincidence detection.

2.4.1 Resolution Limits of QGI

The resolution of any imaging system is generally limited by the diffraction at the optics used before imaging, or by their point-spread function (PSF). The fundamental limit of resolution is described by the Abbe limit:

$$d = \frac{\lambda}{2n\sin(\alpha)} \tag{2.14}$$

where d is the resolution, n is the refractive index of the medium, and α is the half-opening angle of the optical system. In the case of QGI, the wavelength that determines the resolution is the longer wavelength, typically that of the idler photon [89]. Although there are methods to achieve resolution beyond this limit with entangled photons, such as "optical centroid measurements" (OCM) [34, 90], these methods require that multiple entangled partners interact with the object and be detected together. Since QGI spatially separates the participating partners, the Abbe limit still applies to these systems.

Depending on the system, however, not only the resolution of the receiving optics may matter; the characteristics of the illumination source may also limit resolution. In a laser-scanning system, for instance, the beam quality factor M^2 of the laser plays an important role. In the case of QGI, a similar limit is determined by the finite precision of the correlation between the two photons, which is itself influenced by the design of the source [91].

For the far-field setup, the photon source should approximate a point source as closely as possible. This means the laser should be focused as sharply as possible to reduce the size of the pump spot and thus the resolution. However, stronger focusing also increases the divergence of the laser, leading to greater uncertainty in the momentum correlation of the photons as they propagate through the crystal [86].

This dependency for a Gaussian pump beam with radius w_0 and the transverse momentum distribution of the pump light $\Xi(\rho_p)$ is described by the coupled biphoton joint amplitude $F(\rho_i,\ \rho_s)$:

$$F(\rho_i,\, \rho_s) = \Xi(\rho_p)\,\mathrm{sinc}\left(\frac{L}{2}\Delta k\,(\rho_i,\, \rho_s)\right)\,\exp\left(-w_0^2\frac{|\rho_i+\rho_s|^2}{4}\right) \tag{2.15}$$

where ρ_i, ρ_s, and ρ_p represent the momenta of the idler, signal, and pump light respectively, L is the length of the crystal, and $\Delta k\,(\rho_i,\rho_s)$ describes the phase mismatch of the three interacting waves. In the case of QPM tuning of the crystal, an additional term k_Λ must be included in $\Delta k\,(\rho_i,\,\rho_s)$, so that the phase mismatch is described as follows:

$$\Delta k\,(\rho_i,\ \rho_s) = k_{pz} + k_\Lambda - k_{sz} - k_{iz} - \frac{|\rho_i + \rho_s|^2}{2k_p} \tag{2.16}$$

where $k_{\mu z}$ represents the z-components (i.e., components along the propagation direction of light) of the wave vectors for the pump, signal, and idler. In the case of collinear phase matching, this indexing can be omitted for practical purposes, as the deviations of the transverse components from the propagation direction are small.

A more detailed derivation of these formulas can be found in [86], noting that the paper assumes degenerate entanglement in a non-phase-matched crystal. It is also worth mentioning that these formulas assume thin crystals, allowing the effects of beam walk-off from the pump's pointing vector to be neglected. This condition (crystal length significantly smaller than the Rayleigh length of the pump laser, $L_{\text{crystal}} \ll z_{\text{Rayleigh}}$) has always been met in this work [85].

For periodically poled crystals there is an additional uncertainty in the correlation caused by manufacturing variations. The width of the poled regions can fluctuate due to technical limitations, which sets a lower bound on the "line width" of the source or the spectral width of the correlated spectra. This uncertainty, especially when combined with refractive optics (used for imaging), can further limit resolution.

For a detailed, current experimental analysis of the achievable resolution of the SPDC process and its various influences, refer to [59]. While this study uses an "induced coherence" setup (see Chapter 2.3), which operates under different constraints, the fundamental considerations of SPDC can be extended.

2.4.2 Quantum Ghost Imaging with Asynchronous Detection

Modern QGI setups are typically based on a "heralded scheme", as shown in Figure 2.10. To filter entangled photons, the idler photon interacts with the object and is then measured by a bucket detector. This measurement triggers a single-photon camera, usually an ICCD or sCMOS camera, which captures the signal photon. Because the detection of the bucket detector and the triggering of the camera inherently lead to time delays, the signal photon must be "held back" long enough to be registered by the camera.

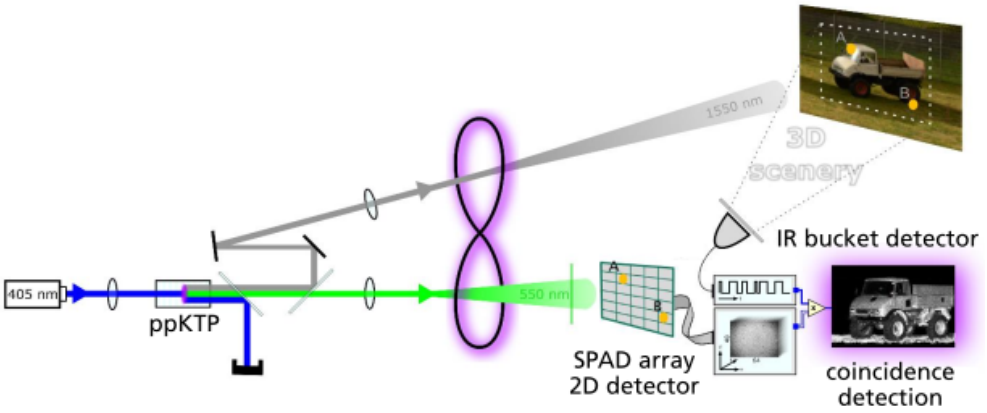

Figure 2.12: Setup for asynchronous Quantum Ghost Imaging, from [20]. The (ICCD) camera from the heralded setup (see Figure 2.10) is replaced by a spatially and temporally resolving camera (SPAD array). By projecting detection times onto a common time base (via TCSPC electronics), the detection times can be cross-referenced. Coincidence detection occurs after measurement through timestamp comparison. This eliminates the need for the delay line and allows 3D imaging using direct time-of-flight (dTOF) methods.

During this delay, however, the correlation between the images must be maintained. This is typically achieved by using a delay line that preserves the image, in which the signal photon is reflected multiple times off mirrors while being imaged onto the mirrors with corresponding lenses [12]. Since these delays are typically on the order of several nanoseconds (corresponding to several meters of optical path length), such delay lines are only feasible with significant alignment and space requirements. Due to the need to preserve the image during the delay, adapting these setups for practical use can be extremely challenging, making them most effective in controlled environments.

Recent developments in single-photon camera technology, particularly in the area of Single-Photon Avalanche Diodes (SPADs), now allow for not only spatially resolved detection of individual photons but also temporal resolutions on the order of picoseconds. This makes it possible to cross-reference the detection events within a measurement window, identify entangled photons by timestamp comparison, and use coincidence detection to identify photon pairs [34, 36].

In QGI, the detection of the bucket detector is typically related to the detections of the camera. The setup shown in Figure 2.12 uses external timing electronics (TCSPC, or time-correlated single photon counting) connected to both the camera and the detector. This allows to track the beginning of each measurement window of the camera and reference to their local detection times, projecting them to the timebase ofthe TCSPC. The detection of the bucket detector is registered directly by the TCSPC, allowing to reference the detections and seperate the acquisition of the signal photons from the idler

photons.

This in turn allows coincidence detection independent of the geometry of the setup [38]. Additionally, this method enables the use of various objects at different depths by distinguishing between the photon detections based on their timing, which allows 3D imaging using direct time-of-flight (dTOF) methods, similar to LiDAR applications. Since the detection of the photons is not synchronized in real-time with the bucket detector, unlike in heralded setups, this technique is called "asynchronous Quantum Ghost Imaging."

Developing and characterizing an asynchronous Quantum Ghost Imaging setup was a key focus of this work, which is discussed in detail in Chapter 3.4.

2.5 Single Photon Avalanche Diodes (SPAD)

SPADs are a specialized form of the widely used avalanche photodiodes (APD). APDs exhibit very high internal electric fields in a portion of the diode due to the geometry of their doping layers. These fields greatly amplify individual electron-hole pairs generated by photon absorption. This amplification allows even small signals, that would be drowned out by the dark noise in a conventional photodiode, to be amplified and processed by subsequent electronics. However, this amplification also introduces some uncertainty in the measured signals, as they can fluctuate significantly and be heavily reduced by previous detections [92].

Unlike APDs, SPADs are operated in a bistable state slightly above the breakdown voltage of the diode, known as the Geiger mode (see Figure 2.13). In this charged state, the SPAD is held until an electron-hole pair is created in the diode (either by photon absorption or thermal effects). Once this occurs, cascading impact ionization of additional pairs leads to avalanche breakdown and uncontrolled signal amplification. While this uncontrolled discharge, triggered by just a single absorbed photon, makes the SPAD unsuitable for measuring the intensity of incoming light, it is ideal for single-photon detection, amplifying the signal to a measurable level.

If the diode were operated above breakdown after detection, the avalanche discharge would sustain itself until the diode was destroyed. To prevent this, a quenching circuit is used to detect the sudden increase in diode current caused by the avalanche breakdown and immediately reduce the diode's voltage. This stops the discharge, clears out excess charge carriers from the APD, and allows the diode to be reset to the Geiger mode, with the voltage slightly above the breakdown point.

The simplest way to realize this control is with a discharge resistor placed in series with the diode. The sudden increase in diode current leads to a corresponding increase in the voltage drop across this

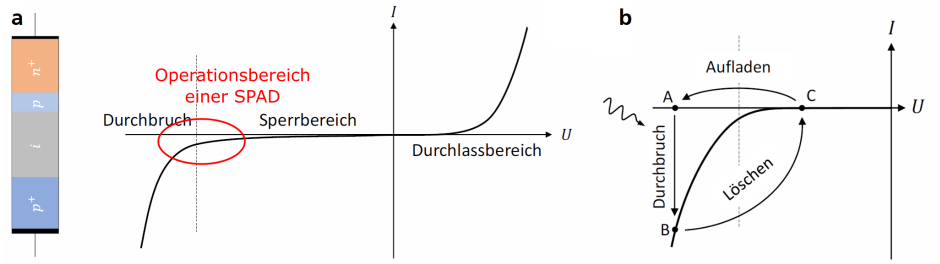

Figure 2.13: Operational principle and quenching of a SPAD. (a) Structure and voltage characteristic of an APD. The p-doped layer in front of the n^+-doped layer leads to a local increase in the electric field strength, resulting in the multiplication of absorbed charge carriers. APDs are typically operated just below the breakdown voltage U_{th} to achieve a defined amplification. SPADs, however, are operated above this voltage (red mark) to amplify a single detected photon into a measurable signal. (b) Quenching and reset scheme. After detection, the avalanche breakdown would sustain itself and destroy the diode. To prevent this, the operating voltage is reduced below U_{th} after detection, discharging the free charge carriers. The diode is then reset to its detection state. Additional details can be found in [93].

(preferably large) resistor, reducing the diode voltage below the breakdown threshold. This allows the diode to discharge, reducing the current and restoring the voltage across the resistor. The APD can then be recharged to the Geiger state (commonly referred to as "recharge" in the literature). Besides this passive quenching approach, there are more sophisticated active quenching circuits that can reduce the reset time of the diode and its dead time after detection [92]. These techniques can also address some of the problems associated with passive quenching [93, 94].

2.5.1 SPAD Design and Layout

Depending on the application and desired parameters, there are various designs and characteristics of SPADs. The most widely used are reach-through and planar SPAD structures, owing to their relatively simple design. Reach-through SPADs, which use the full thickness of the substrate, have advantages in detection efficiency due to their large absorption region. This effect is particularly noticeable in the near-infrared (NIR) spectrum [94]. However, the thick absorption layer also degrades time resolution and increases noise. Additionally, they are incompatible with CMOS processes, unlike planar SPAD structures, making them less suitable for LiDAR or QGI applications, where good time resolution and integration with on-chip electronics are important. Therefore, this work focuses primarily on planar SPAD structures.

The design of a planar SPAD is shown exemplarily in Figure 2.14, with the absorption region marked in red. The absorption region in these structures is typically several nanometers to a few micrometers

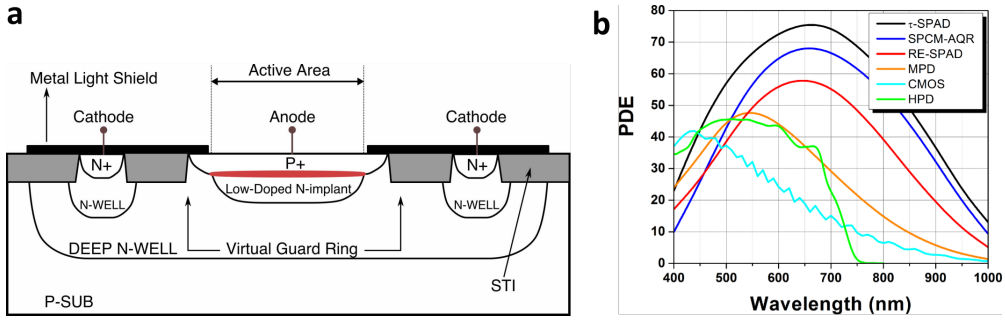

Figure 2.14: Cross-section of a thin-film SPAD and detection efficiency (DE) of various SPAD geometries. (a) Cross-section of a thin-film SPAD with labeled doping layers. The avalanche region is marked in red. The image was taken from [95]. (b) Photon detection efficiency (PDE) of different SPADs based on various technologies. The curves were provided by the manufacturers. τ-SPAD and SPCM-AQR: thick-film, reach-through SPADs. RE-SPAD: "Red-Enhanced" thin-film SPAD. MPD: commercially available thin-film SPAD. CMOS: CMOS (thin-film) SPAD array prototype. HPD: hybrid photodetector prototype with a GaAsP photocathode. Details can be found in the original publication [96].

thick, much smaller than in "reach-through" structures. This makes them significantly faster in terms of response time, capable of achieving resolutions in the double-digit picosecond range [97]. However, the size of the absorption region limits the detection efficiency of the detector, especially in the NIR range. This is due to the decreasing absorption coefficient of silicon for longer wavelengths [98], which means that longer-wavelength light is absorbed over larger volumes. As a result, for smaller structures, not only does the overall absorption decrease, but the peak detection efficiency also shifts toward the ultraviolet, as shown in Figure 2.14.

To generate the strong electric field required for detection, while maintaining uniformity across the entire active area, the active region of the SPAD serves as the anode. To realize thin active layers (necessary for good time resolution), the cathode is placed as a concentric ring around the anode. Normally, this design would lead to a collapse of the electric field at the edge of the active region, known as premature edge breakdown (PEB) [94, 99]. To avoid this, special insulating guard rings are placed between the anode and cathode.

These guard ring structures are used in nearly all SPAD designs. They help to homogenize the electric field across the active area, improving both dark noise and detection efficiency (DE). Furthermore, the guard rings isolate the SPAD's active region from the surrounding substrate, preventing free charge carriers from diffusing into the active region and causing additional noise.

The shift in detection efficiency for different layer thicknesses is a known effect, familiar from solar cell research, and there are ways to optimize efficiency for specific spectral ranges. However, it is important

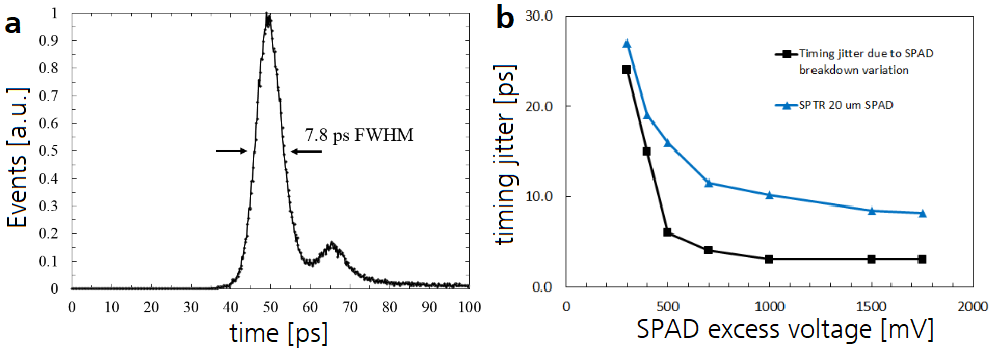

Figure 2.15: Timing characteristics of a SPAD. The images are taken from [103]. (a) Time jitter of a SPAD at an overvoltage of $1.75\,\mathrm{V}$. The second peak is caused by a reflection in the optical system. Details can be found in [103]. (b) Time jitter of the detector depending on the overvoltage (blue) and the uncertainty caused by the SPAD breakdown (black).

to ensure that such optimization does not adversely affect the fundamental properties of the SPAD. For example, a reflective coating on the back of the SPAD can enhance detection efficiency in the NIR without significantly affecting the time resolution, as the light's round-trip time is much shorter than the detector's time resolution. Scattering layers, however, which scatter normally incident light into the detector volume, are unsuitable for cameras as they can scatter photons into other parts of the detector, increasing noise.

To improve efficiency, especially in the UV and short-wavelength range, "backside illumination" is often used. In this configuration, the chip is illuminated through the substrate rather than from the front side. This avoids passing through the metallization layers on the surface of the semiconductor, which reflect and absorb more than the substrate itself [100, 101]. Furthermore, anti-reflection (AR) coatings are frequently employed because silicon has a much higher refractive index than air. Depending on the wavelength, this difference can lead to a reflection of $30 - 40\%$ [102]. These AR coatings are commonly used in optics but are typically highly material- and wavelength-dependent. Therefore, for such coatings, the intended application and, above all, the wavelength used should be known.

2.5.2 Time acquisition of a SPAD

As previously mentioned, SPADs can react very quickly due to the small dimensions of the active region [104]. The response time of the detector is fundamentally limited by the thickness of the active layer and the drift velocity of the electrons that initiate the avalanche breakdown. The drift velocity increases

with stronger electric fields, but saturates near the breakdown voltage, which is the operational range for SPADs. It is also temperature-dependent and decreases with rising temperatures. For silicon at room temperature—the most common operational condition for modern SPADs—the saturation occurs at a velocity of approximately $10^5 \frac{\mathrm{m}}{\mathrm{s}}$, which corresponds to a time resolution between 1 and 10 picoseconds for active layer thicknesses of 100 nanometers to 1 micrometer.

Simple SPADs can get very close to this fundamental limit [103, 105], though their exact time resolution is highly dependent on the applied voltage, specifically the excess bias above the breakdown voltage, as shown in Figure 2.15 [92, 103]. With increasing voltage, the detection probability (photon detection probability, PDP) of the detector also increases. However, this leads to higher dark counts (dark count rate, DCR), and it raises the likelihood of "after-pulsing," where residual charge carriers not fully drained during reset can trigger another avalanche shortly after the previous detection. This after-pulsing effect can be mitigated by longer reset times or more gradual recovery of the SPAD, though this limits the detector's overall detection rate [106, 107].

The choice of operational voltage and reset time depends largely on the specific application and should be optimized accordingly. For example, in this work, the dead time of the idler detector was adjusted to match the dead time of the SPAD camera used.

For SPAD arrays, which are needed for QGI, time resolutions in the single-digit picosecond range are generally not achieved [108]. This is because these arrays not only need to detect photons but also process the detections. It is crucial that each pixel registers the detection time independently of the other pixels in the array. This is accomplished using Time-to-Digital (TDC) circuits integrated into each pixel to capture both the spatial and temporal information of each detection. Depending on the requirements, several methods exist to implement these circuits. For an overview, refer to the relevant literature [109, 110]. The following sections focus on the techniques used in this work, including simple counter circuits based on a system clock combined with more precise flash-TDCs [32, 111], and differential TDCs based on ring oscillators. In most cases, TDCs are triggered by a detected photon, measuring the time until the end of the detection, rather than continuously counting from the start of the measurement.

Counter-based TDCs are relatively simple circuits that rely on a global system clock. A stable clock source (such as a quartz oscillator) is typically used, which is started before the measurement to avoid any transient effects and ensure a stable signal. The TDCs then count the clock edges (either rising or falling, depending on the application) that occur between the start of the measurement and photon detection, thereby providing a timestamp for each event. These circuits typically work well with clock frequencies in the tens of MHz range, corresponding to nanosecond-level resolution.

To achieve better time resolution (in the picosecond range), the clock frequency would need to be in the GHz range. Although this is now technically possible with integrated circuits, it is typically associated with

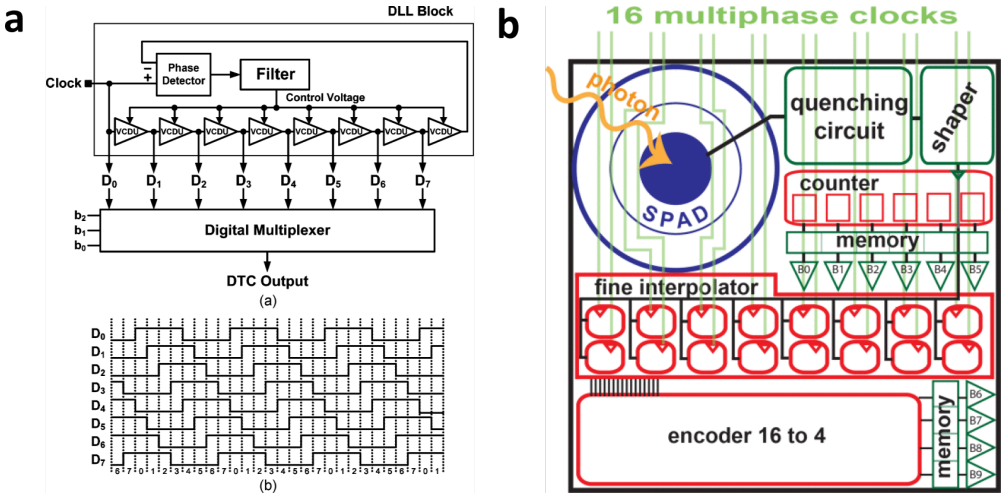

Figure 2.16: Delay-locked-loop (DLL) TDC Schaltungen. (a) Block Diagramm eines DLL TDC mit der Thermometer-codierten Ausgabe. Jede Kaskade verschiebt die Phase des Clock Signal um eine minimale Zeiteinheit (der Auflösung der TDCs). Bei einer Detektion wird der aktuelle Zustand des TDC ausgelesen und für die Datenübertragung Binär codiert. Das Bild stammt aus [111]. (b) Layout eines Pixel eines SPAD Arrays mit Zeitaufnahme (TDC). Exemplarisch gezeigt ist das Layout eines Pixels eines 32x32 Pixel SPAD Arrays mit einem groben Clock-Counter und einem Fein-Interpolator auf DLL-Basis. Der SPAD selbst, also die eigentlich zur Photonen-Detektion genutzte Fläche, ist dabei klein im Vergleich zur kompletten Peripherie des Pixels. Das limitiert den Füll-Faktor und damit die Detektionswahrscheinlickeit, kann aber durch entsprechende Methoden (z.B. Mikro-Linsen-Arrays) kompensiert werden. Das Bild wurde [112] entnommen.

significant cooling and power demands, making such systems impractical for many camera applications. Therefore, for finer resolution, a delay-locked loop (DLL) is often used. A DLL divides each clock period T_{Coarse} into x equal parts, with each part having a delay $T_{\text{DLL}} = T_{\text{Coarse}}/x$ [109]. A chain of flip-flops is used to delay the clock signal in increments, and when a photon is detected, the state of the flip-flops is read out to determine the phase of the clock signal at the time of detection. The resulting x-bit thermometer code is then converted into a binary code to optimize data transmission. The TDCs in the two-row array used in this work were based on this technique, with a finer TDC used for actual photon timing [32]. Using this method, highly accurate and stable TDCs can be implemented. However, due to space limitations in the detector, the number of flip-flops must be kept small, which limits the achievable resolution. This design is therefore most suitable for linear, one-dimensional arrays.

For two-dimensional arrays, ring oscillator-based TDCs are more commonly used due to their smaller footprint. These TDCs consist of a coarse counter that measures the oscillations of a base clock and provides an initial rough timestamp. The clock signal is then fed through a cascade of inverters, each of which shifts the phase of the clock signal by $2\pi/x$, where x is the number of inverter stages. When the measurement stops, the state of the inverters is compared to interpolate the timestamp. The condition of the inverters is typically stored in analog form (e.g., using capacitors) to suppress quantization errors during multiple measurements. The 2D-SPAD used in this work featured a three-stage ring oscillator with simple comparator circuits, where a signal served as the reference for the coarse counter [113]. The oscillation period, and hence the time resolution, could be adjusted via the power supply.

For higher time resolutions, the space required for the TDC increases significantly, as shown in Figure 2.16. This leads to a lower fill factor, reducing the overall photon detection probability. However, techniques such as microlens arrays can partially compensate for this limitation [114].

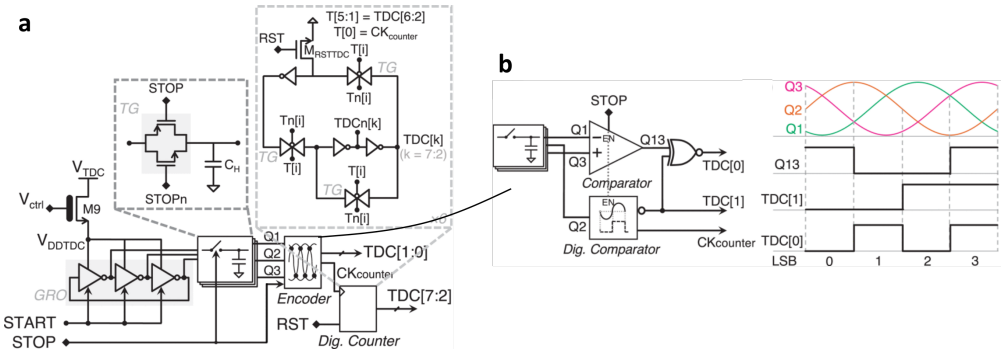

Figure 2.17: TDC design based on ring oscillators. The images are from [113]. (a) Block diagram of a three-stage ring oscillator, as used in this work. (b) Circuit diagram of the fine interpolator and the resulting output signal encoding.

2.6 Image Enhancement and Object Detection

Every imaging system is subject to noise, and its effects can be varied and numerous. Some of these noise sources, however, can be estimated and approximately corrected depending on the characteristics of the setup. For example, deterministic errors such as dark noise, which is typically due to electrical noise in the detector's individual pixels, can be approximated as independent of the illumination. This type of noise manifests as a constant offset in the recorded image and can be measured by taking a reference measurement in the absence of light, which can then be subtracted from the actual measurement. Other forms of noise, such as shot noise, which arises from fluctuations in the number of emitted and detected photons, cannot be easily predicted or compensated [94].

These noise effects typically result in a degradation of image quality or, in the case of 3D imaging, a deterioration in the 3D model produced. However, with the right assumptions, the images can sometimes be post-processed to improve quality. For example, object detection techniques can be used to classify the captured images and infer the likely shape of the object. In the case of 3D models, additional assumptions like a smooth surface or a comparison to known structures can help refine the generated models.

It is important to note, however, that such manipulations can be a double-edged sword. While they can improve detection, they can also cause details of the object to be lost, and in some cases, they may even cause the classification to fail. The noise effects relevant to QGI will be briefly described below, along with possible image optimization techniques.

2.6.1 Noise Effects in QGI

Any imaging system that integrates optical power or counts the number of photons detected is inherently subject to shot noise. This effect arises from fluctuations in both the number of illumination photons and the charge carriers generated by detection and follows a Poisson distribution. This is especially dominant in low-light conditions because the standard deviation Δn, given by [115]

$$\Delta n = \sqrt{\bar{n}}, \tag{2.17}$$

with $\bar{n}$ being the average number of detections, is quite large compared to the number of detections or the measured signal. This is the dominant noise process for most systems that work with few photons, both due to signal uncertainty and detection uncertainty. To reduce this effect, single-photon imaging techniques are increasingly being employed, where the arrival time of individual photons is recorded rather than the photon count. QGI is such a single-photon system. Since only one photon is measured at a time, the uncertainty due to shot noise is eliminated, allowing for noiseless, digital readout.

However, while the photon count is noiseless, the arrival time of photons remains uncertain and is dependent on the setup. In the case of pulsed lasers, for instance, the photon arrival times also follow a Poisson distribution. In QGI, however, this uncertainty is determined by the temporal correlation between the two photons, and due to their simultaneous emission, there is no inherent statistical uncertainty in their arrival times. The uncertainty is primarily determined by the finite time resolution and accuracy of the two detectors. Depending on the system, the time delay due to photon dispersion may also play a role [16]. Dispersion effects are largely dependent on the emission bandwidth and therefore on the properties of the photon source, such as the length of the nonlinear crystal. Unlike in conventional photon integration systems, this temporal distribution can be analyzed and, to some extent, compensated during measurement.

In contrast to the temporal information, which assumes the involvement of only two photons, the spatial information from coincidence detection—and thus the resulting coincidence image—exhibits uncertainty in the number of photons per pixel. This number, or signal level per pixel, follows the statistical distribution of the object's backscattering, overlaid with a Poisson distribution. While the temporal statistics of backscattering can be determined through the possibility of 3D reconstruction of the object, the spatial Poisson statistics cannot be separated from the process.

Dark noise from the imaging detector also overlaps with the QGI-generated image, but as previously mentioned, it can be approximated through a preliminary characterization and subtracted from the image. However, QGI introduces an additional noise term due to so-called "false coincidences." These refer to detections that the system registers as coincident photons, arriving within the same time window but

without any physical connection to one another.

These false coincidences can be triggered by random noise events or real photons whose partners were not detected (e.g., due to missed detection in one arm). They typically appear as a superposition of dark noise and SPDC (spontaneous parametric down-conversion) emission. Their influence can be estimated by adjusting the time delay between the idler and signal detections so that only false coincidences are measured, instead of detecting real coincident pairs.

This measurement allows for the extraction of the false coincidence rate, similar to the method used to estimate dark noise. However, unlike dark noise, determining the false coincidence rate requires a fully constructed and calibrated QGI setup to measure the SPDC emission accurately. With the widely-used heralded QGI setups, this characterization requires an additional measurement, whereas with the asynchronous QGI setup developed in this work (see 3.4), this information can be directly extracted from the imaging data itself.

Additional effects and limitations relevant to this discussion can be found in the literature, e.g. [116].

2.6.2 Object Detection and 3D Optimization

The techniques described here for object detection pertain mainly to the setup described in Chapter 3. Some of these techniques can also be applied to classical heralded QGI setups, although in those cases the identification of coincident photons and temporal analysis are less critical, since coincidence detection is inherently guaranteed by the setup design. In classical setups, no 3D imaging can be achieved, as the timing information of the photons is lost.

For QGI, object detection can be split into two major parts: identifying coincident photons from the individual detections in both arms and reconstructing the 3D shape of the illuminated object. These two methods can also be combined to support or improve 3D reconstruction, where necessary.

The first task—coincident photon identification—is a one-dimensional problem that involves comparing the time stamps from both detection arms to identify the so-called coincidence peak. This peak appears as a maximum in the distribution of time differences between the two detection arms and represents the arrival time of the photon pairs (assuming a static object). In the case of multiple objects at different depths, multiple coincidence peaks may appear, corresponding to their spatial positions. A straightforward, fast optimization algorithm such as gradient ascent can be applied to detect these local maxima [117].

However, selecting the appropriate optimization algorithm is more complex than it might initially seem. The distribution of detected false coincidences is determined by the convolution of both the detector

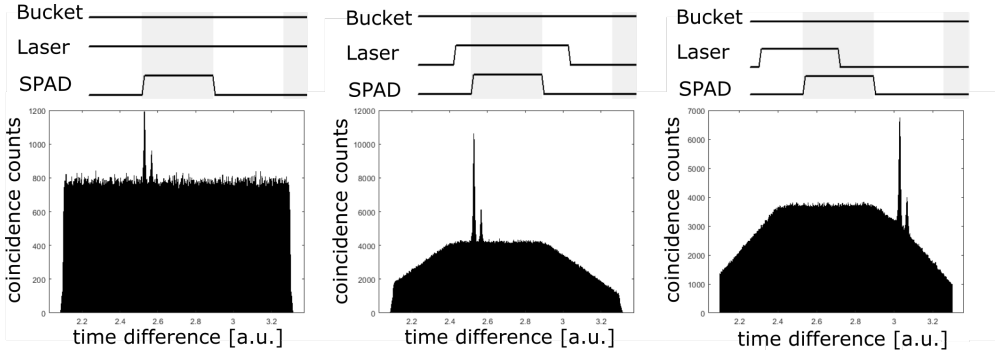

Figure 2.18: Coincidence analysis depending on the detection/emission characteristics of the detectors or the source. If only one device is gated, the analysis is no different from the continuous-wave (cw) case. When two gated detectors are used, the distribution of uncorrelated coincidences changes from uniform to a trapezoidal function (convolution of two rectangular signals). Poor synchronization of the gating windows can cause the coincidence peak to fall on the slope of the trapezoidal function, which may lead to issues with the optimization algorithms used for peak detection. This can be mitigated by combining faster algorithms with convergent methods or by adding appropriate constraints.

response functions and the characteristics of the photon source. These convoluted detection functions can sometimes lead to incorrect results if the optimization algorithm is not properly tuned, as shown in Figure 2.18.

Ideally, if both detectors are free-running and the photon generation rate is constant, the false coincidence rate would follow a uniform distribution, and the coincidence peak would be (theoretically) the only deviation in this function. However, due to the need for gated SPAD arrays, this scenario is rare, although the resulting distribution still resembles a uniform distribution.

If, however, a gated SPAD array is synchronized with a reference detector or pulsed laser, as is often done to reduce data volumes or optimize coincidence detection, the convolution of the two response functions produces a trapezoidal distribution instead of a uniform one. As shown in Figure 2.18, poorly chosen gate times can cause the coincidence signal to no longer coincide with the global maximum. This is problematic for simple, fast optimization algorithms, which may either get stuck in local maxima or fail to detect peaks due to insufficient sampling resolution.

The problem of object reconstruction is closely tied to the temporal analysis of the data. Closely positioned objects can cause difficulty in differentiating or classifying the detections. This issue can be mitigated by applying appropriate constraints, such as assuming smooth object surfaces or analyzing signal strength. In particular, the temporal change of the images within the coincidence peak plays an important role in reconstructing the 3D scene and distinguishing objects. In some cases, it is even possible to infer surface

details.

However, it is important to remember that such assumptions and manipulations can also distort the measurement and reconstruction. For instance, if a depression in an object is mistakenly projected as part of the object's surface, it could lead to erroneous 3D models.

3 Asynchronous Quantum Ghost Imaging

This chapter presents and describes the first realization of a Quantum Ghost Imaging (QGI) setup with asynchronous detection. The development and optimization of this setup are central to this dissertation and are shown schematically in Figure 3.1. As a photon-pair source, an optically nonlinear, periodically poled potassium titanyl phosphate (KTP) crystal was used, pumped by a 405 nm indium phosphide (InP) laser. The poling period of the crystal was chosen to achieve collinear Type-0 SPDC with photon pairs at 549 nm (signal) and 1550 nm (idler) at the selected pump wavelength of 405 nm. The choice of Type-0 phase matching allowed for the use of the highest nonlinear coefficient (d_{33}, [118, 119]) of KTP, thus achieving the highest conversion efficiency.

The idler photons were separated from the signal and pump photons via dichroic mirrors, interacted with a scene, and were then temporally recorded by a fiber-coupled, cooled indium gallium arsenide (InGaAs) detector. The signal photons were also separated from the pump light using dichroic mirrors and then detected both temporally and spatially using a SPAD camera (single-photon avalanche diode, see section 2.5) based on silicon. To avoid disturbing light scattering, the remaining pump light was directed into a beam trap and absorbed.

For coincidence detection, the temporal information from two independent detectors (bucket and camera) must be referenced to each other. For this purpose, both detectors are connected to dedicated time-correlated single-photon counting (TCSPC) electronics, which are integrated via PCI in a measurement computer. These electronics register the measurements from both detectors and allow the temporal information to be transferred to a common time base. Since the detection of the photons occurs independently of each other, unlike the "heralding" approach, and the data from two asynchronously operating detectors are synchronized, this type of scheme was named "asynchronous quantum ghost imaging."

Since they share the same time base, the resulting timestamps for signal and idler detections can be

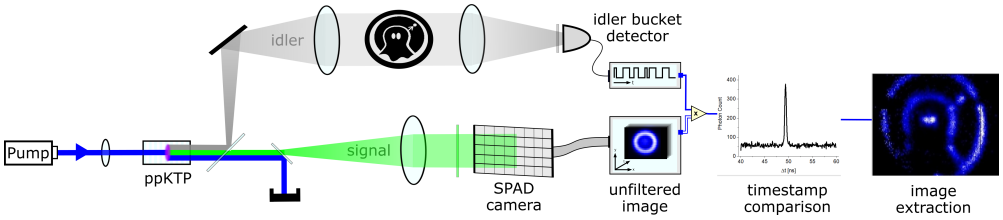

Figure 3.1: Setup for asynchronous Quantum Ghost Imaging. The photon pairs are generated via SPDC using a pump laser. The resulting idler and signal photons are separated and collimated. The idler photons are first imaged onto the object and then temporally recorded by a single-element detector. The signal photons are imaged onto a camera and detected both temporally and spatially. Both detection times are referenced to a common time base using TCSPC electronics, allowing them to be correlated. By comparing detection times, entangled pairs can be identified, and an image of the object can be obtained.

compared. Due to the fixed time of flight and simultaneous emission of both photons in a pair, the comparison of entangled partners leads to a constant difference. This allows the entangled photons to be identified and the image information from the signal photons to be obtained. Due to the spatial correlation of the partners, this corresponds to the image of the scene from the "perspective" of the idler photons[1].

The following sections describe the individual components of the setup and then the entire system in detail.

3.1 Photon-Pair Source

In this work, periodically poled KTP crystals were used as the photon-pair source, pumped by a near-UV laser. Due to energy conservation in SPDC, the pump photon must be the highest-energy photon in the photon triplet. Since KTP crystals become opaque at $\sim 350\ \mathrm{nm}$, a pump wavelength of 405 nm was chosen. This wavelength has the advantage of being used in Blu-ray technology, making highly developed off-the-shelf lasers available. Additionally, these lasers are still visible and pose fewer health risks or issues with crystal opacification (gray tracking) than higher-energy photons.

Two lasers were used in this work: a "simple" diode module with optional pulse operation and a very narrowband, single-frequency laser (Toptica TopMode 405). Both lasers were designed to operate at a central frequency of 405 nm, though manufacturing tolerances can cause slight fluctuations. The emission was verified through spectroscopic investigations (see section 3.4.5), as shown in Figure 3.8. The spectrum

[1] By using momentum correlation for imaging, the size of the emission spot of signal and idler scales approximately in proportion to their wavelengths.

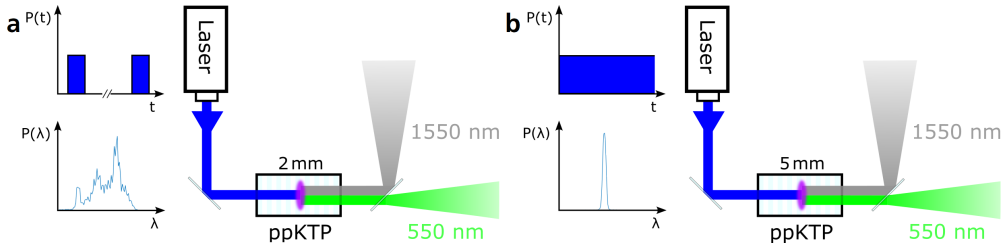

Figure 3.2: Photon-pair sources used in this work. The crystal was temperature-stabilized during measurements. (a) Source used for imaging. A pulsed laser diode (Obis LX405, $\lambda_p = 404$ nm, $\Delta\lambda \approx 0.6$ nm) pumps a 2 mm long periodically poled KTP crystal ($\Lambda = 4.25$ μm). The laser pulses are synchronized with the detector measurements. (b) Source used for spectroscopic investigations. A very narrowband SLM laser (Toptica TopMode 405, $\lambda_p = 404.84$ nm, $\Delta\lambda < 0.01$ nm) pumps a 5 mm long ppKTP crystal ($\Lambda = 4.25$ μm). The narrowband laser achieved a very defined spectral correlation of the photon pairs. See Section 3.4.5 for details.

of the pulsed laser is significantly broader, with a total width of about 0.6 nm, compared to the SLM laser, which has a width of ~ 0.02 nm, though the actual width is expected to be smaller due to measurement resolution (0.01 nm, for details see section 3.4.1).

The pulsed laser was chosen to avoid issues with detector gating. The SLM laser, on the other hand, was used to analyze the spectroscopic properties of the source (see section 3.4.5) and the effects of pulse operation, with particular interest in the instability of the central frequency and bandwidth of the pulsed laser, which can vary from pulse to pulse.

The poling period of the crystals was chosen at 4.25 μm to achieve collinear Type-0 phase matching at room temperature for the combination 405 nm (pump) - 549 nm (signal) - 1550 nm (idler) (see Figure 3.3). The idler wavelength was chosen to use a fiber-coupled single-pixel InGaAs-SPAD developed for quantum communication as the bucket detector, which is already a well-established technology [120]. The signal wavelength was adjusted so that current silicon-based SPAD cameras offer good detection efficiency (DE) in this spectral range (see Figure 3.5 or [106]). These wavelengths also allowed for imaging in the SWIR based on a VIS camera.

Due to the nature of phase matching, pump, idler, and signal photons share the same polarization, with signal and idler photons having only a slight angular offset in their emission. Additionally, Type-0 phase matching uses the relatively large d_{33} nonlinearity of KTP's nonlinear tensor. This allows for particularly high conversion efficiency, as SPDC sources with similar parameters generate photon pairs at rates up to $1.1 * 10^4$ pairs/s/mW$_{\text{pump}}$ [121].

However, the aperture of the crystals is currently technically limited by the poling process, here to a

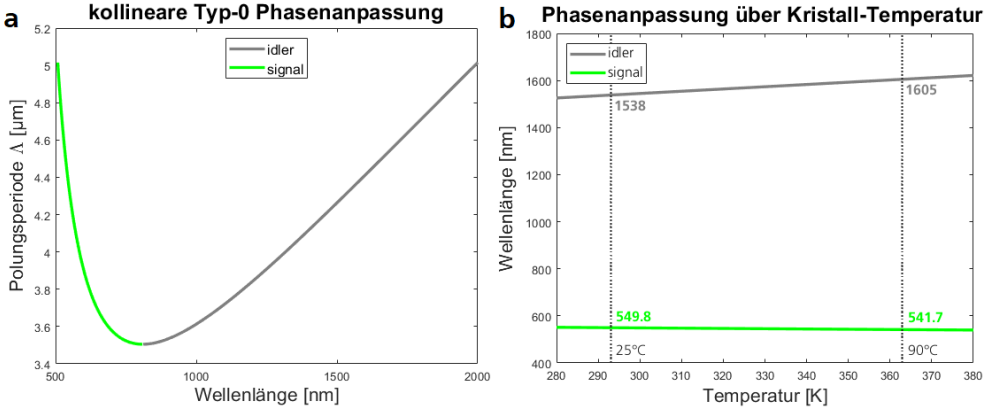

Figure 3.3: Dependence of KTP phase matching on various poling periods and temperatures. (a) Signal and idler wavelengths for collinear Type-0 phase matching of KTP, depending on the poling period. A pump photon at 405 nm and a temperature of 293 K ($\hat{=}$ 20 °C) are assumed. (b) Shift of signal and idler wavelengths, depending on crystal temperature. The source used in this work, with a laser at 405 nm and a poling period of 4.25μm, was assumed.

cross-section of $2x1\ \mathrm{mm}^2$. This significantly limits the resolution of a "near-field" setup using a collimated laser beam and the resulting spatial correlation of the photons for imaging. Instead the "far-field" setup was used (see section 2.4, Figure 2.11). In this setup, a laser is focused into the crystal, and the momentum correlation of both photons is used to obtain spatial image correlation. The possible spatial resolution of this setup is primarily determined by the size of the pump spot and the length of the crystal [122]. Focus control also plays a significant role, as described in section 3.4.4.

For imaging, the crystal was placed in a special crystal oven (Ekspla TK8), which allowed temperature stabilization between 25 °C (maximum temperature of the air-conditioned lab) and 90 °C. This allows the collinear phase-matching condition (described in section 2.3.1) to be shifted between $550 \ldots 542$ nm (signal) and $1538 \ldots 1605$ nm (idler), as shown in Figure 3.3. This condition describes only the photon pairs emitted collinearly with the laser beam.

The overall spectrum of emitted photons is, however, significantly broader. The wavelength of the signal and idler photons strongly depends on their emission angle, especially when the pump spectrum is narrow. The reason for this is that the phase-matching condition can be fulfilled with a slight angular deviation of the wave vectors (see section 2.3.2) for photon pairs with different wavelengths (see Figure 3.4)).

Since the photon momentum of the longer-wavelength idler photons is lower (see Equation 2.11), but the sum of both momenta must still equal the momentum of the pump photon, the emission angle of the

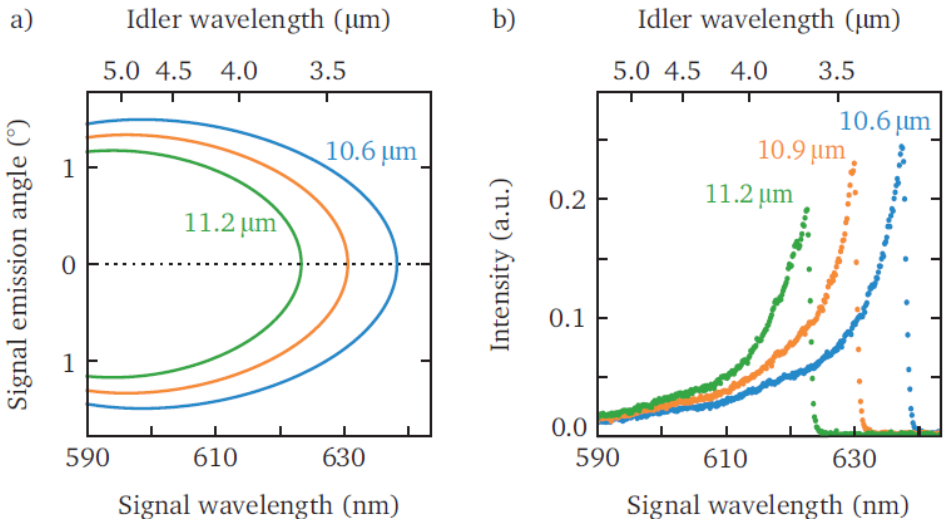

Figure 3.4: Spectral-spatial emission characteristics of a lithium-niobate SPDC source, comparable to the emission of the KTP source used here. The image was taken from [16]. Here, a temperature of 40 °C and a pump laser at 532 nm were assumed. (a) Phase-matching curves for different poling periods. Note the scaling of the idler wavelength, which is linked to the signal wavelength by Equation 2.9. Additionally, this graph shows the emission angle of the signal photons, not that of the idler photons. (b) Intensity of the SPDC process as a function of wavelength, measured in the visible range. It can be seen that the intensity is maximized in the collinear case and decreases toward shorter signal wavelengths/larger emission angles.

generated idler photons is significantly larger than that of their entangled partners. As photon energy, or wavelength, and momentum are linked by the refractive index $n(\lambda)$—which shows only a slight difference for KTP at the chosen signal and idler spectra—the emission angle scales approximately in proportion to the wavelengths. Thus, when the same focal length is used to collimate the emission, the size of the emission spot also scales with this ratio.

The spectral width of the emitted spectrum can also be influenced by manipulating the source. For instance, longer crystals typically lead to a narrower spectrum, as the acceptable phase mismatch Δk decreases (see Equation 2.12). In longer crystals, the nonlinear tensor χ^2 begins to interfere destructively for smaller phase mismatches instead of constructively, thus spectrally narrowing the emission.

However, the length of the crystals is also subject to limitations, especially in the "far-field" setup. Here, the crystal length should be significantly smaller than the Rayleigh length of the pump laser used ($L_{crystal} << z_{Rayleigh}$) to maintain the momentum correlation of the SPDC process. However, by choosing a larger pump focus, and thus a larger Rayleigh length, the achievable resolution is limited (see

section 2.4.1, [59]).

Therefore, in this work, relatively short crystals, up to 5 mm in length, were used. For the main topic of this dissertation—imaging and investigations into the resolution of the correlation—only 2 mm-long crystals were used, while the following spectroscopic studies used 5 mm-long crystals.

After generation, the photon pairs were separated by a dichroic mirror and individually collimated. An attempt was made to collimate both signal and idler photons together using an appropriate system. However, off-the-shelf achromatic doublets were found to be unsuitable for most experiments, especially for the spectroscopic investigations, due to their limited bandwidth. The use of reflective optics, especially for collimation, remains very interesting however.

3.2 Detectors

All detectors in this work were single-photon avalanche diodes (SPADs), whose operation is described in section 2.5.

For the idler, a special low-noise InGaAs detector was used (ID230, [120]). To reduce noise, this detector was cooled, allowing operation at up to $-90\ ^{\circ}\mathrm{C}$. Additionally, this detector can be operated at various bias voltages and dead times, which affect the detection efficiency (DE) and dark noise. Since the dark noise averaged $5 * 10^4$ cps at a minimum dead time of 2 μs (used for the measurements in section 3.4.3) and a maximum DE of $25\ \%$, the detector was mainly operated at $15\ \%$ DE in this work. At this DE, the noise was significantly reduced to an average of $1 * 10^2$ cps, and the dead time of the detector was adjusted to the dead time of the camera used.

A major disadvantage of this detector is its connection to an optical fiber (graded-index fiber with $62.5\ \mu\mathrm{m}$ diameter), which stems from its development for quantum communication. For imaging, or for remote sensing applications, this fiber coupling is disadvantageous because the emitted light must first be coupled into the fiber. This usually results in high losses, especially for non-cooperative targets, where the photons are not reflected but diffusely scattered. Additionally, the modes are limited by this coupling, resulting in a loss of detail in the resulting image. Although an "open" detector would be preferable for imaging, such detectors only recently became available in the desired spectral range and were not available for this work. More details on potential improvements and other idler detectors can be found in section 4.2.

Silicon SPAD arrays were used as cameras. These arrays typically operate in a gated mode, meaning they record measurements in discrete frames. They often have two operating modes: counting mode and timing (or Geiger) mode. In counting mode, these cameras count all detections registered per frame in

each individual pixel. As such, they are used as extremely sensitive cameras, for example, for investigating phototoxic materials [123, 124] or as night vision devices [125]. In Geiger mode, they can only detect one photon per pixel and frame, but with temporal resolution. This makes them very interesting as LIDAR detectors and for measuring fluorescence lifetimes, depending on the design and implementation of the detectors [32, 126].

For the first proof-of-concept measurements, a detector developed for automotive LIDAR applications by the Fraunhofer Institute for Microelectronic Circuits and Systems (IMS) was used. This detector is characterized by its extremely low dark noise [38, 127] and allows the detection of individual photons with a time resolution of 312.5 ps. It consists of two rows of 192 pixels each and will henceforth be referred to as "2-line detector". Each pixel consists of four individual SPADs arranged in a line to increase the fill factor to $5.32\ \%$ without significantly impacting time resolution and dark noise.

To enable 2D imaging with this detector, it was mounted on an automated translation stage and scanned along one image axis. This scanning routine obviously reduces the fill factor compared to a corresponding two-dimensional detector, with the reduction proportional to the number of scan steps. For the measurements in section 3.4.2, 80 scan steps were used, reducing the fill factor of the measurement[1] to about $0.05\ \%$. Due to the correspondingly long measurement times and high losses—which would increase significantly in reflection—this detector was only used as a proof-of-concept in transmission.

For the demonstration of 3D imaging, a true 2D detector was developed by Fraunhofer IMS. The design of the proof-of-concept detector had to be revised because the delay-locked-loop (DLL) TDCs used in the 2-line detector were not suitable for a 2D detector (details can be found in section 2.5.2). This development was carried out in parallel with our proof-of-concept setup, with the TDCs designed as ring oscillators. However, the resulting detector [128] showed issues regarding time resolution. The main reason for this was fluctuations in the operating voltage of the individual TDCs across the entire chip. These fluctuations led to significant blurring of the time signal, preventing coincidence detection and thus making the detector unsuitable for QGI.

Instead, a detector from another partner, Fondazione Bruno Kessler (FBK), was used, which was developed for a wide range of quantum applications [34, 129] (referred to as "2D detector"). While its resolution is limited to 32x32 pixels, it is more than sufficient for a proof-of-concept demonstrator. The fill factor is very high at $20\ \%$, mainly achieved through miniaturization of the peripheral electronics. This miniaturization, however, limits the size of the TDCs and thus both the time resolution to about 200 ps and, especially, the frame length of the detector to about 60 ns [129, 130]. The TDCs here are also based on ring oscillators and show fluctuations in the time resolution of each pixel. These could be estimated and compensated for,

[1] To reduce dark noise and improve image resolution, only one SPAD per pixel was activated, and the scan step size of $\sim 50\ \mu\mathrm{m}$ corresponded to about a quarter of the pixel height.

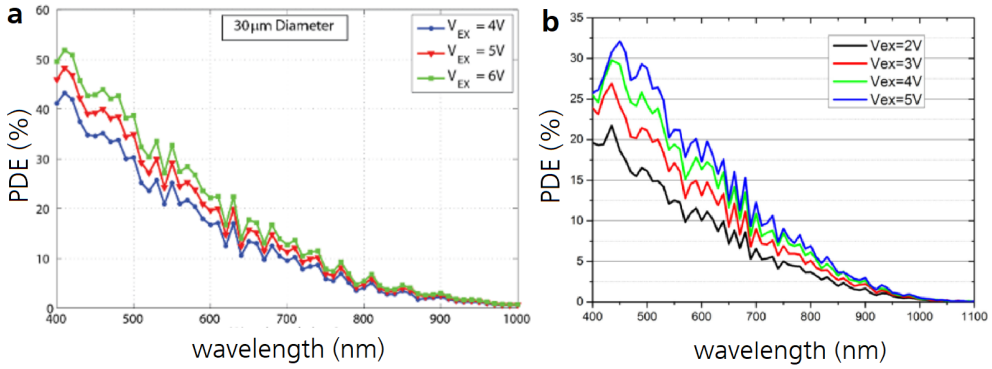

Figure 3.5: Detection efficiency of the SPADs used in this work. (a) Detection efficiency of the SPADs of the 2-line detector, taken from [106]. Due to the thin absorption layer of the SPADs, the DE of the SPADs decreases at longer wavelengths (see section 2.5). With increasing overvoltage, the DE increases, but this voltage also affects the dark noise and time behavior of the detector. Details can be found in the original publication [106]. In this work, an overvoltage of 5 V was used. (b) Detection efficiency of the SPADs of the 2D detector at various overvoltages, taken from [107]. Details can also be found in [107].

as discussed in section 3.3.

A disadvantage is also the difference in the SPAD architecture itself, or rather, the fabrication technology used. The 2-line detector was manufactured with 350 nm CMOS technology, while the 2D detector was manufactured with 150 nm CMOS technology [106, 107]. The SPADs of the 2D detector are also smaller, with a 10 μm diameter compared to the 12 μm diameter SPADs of the 2-line detector. This generally reduces detection efficiency due to the relatively larger guard rings, which reduce the effective fill factor, but also increases the dark noise [106]. As shown in Figure 3.5, the detection efficiency of the detectors increases with increasing overvoltage. However, this voltage also influences the dark noise and time behavior of the detector, as described in section 2.5. Data on the specific detectors can be found in the original publications [106] and [107].

In this work, an overvoltage of 5 V was chosen for the 2-line detector, which results in a DE of approximately $25;\%$ (at 550 nm) and a dark noise of about $10;\mathrm{counts/s}$ per pixel [131]. For the 2D detector, an overvoltage of 2.7 V was chosen, corresponding to a DE of approximately $17;\%$ and a dark noise of about $20;\mathrm{counts/s}$ per pixel [107].

3.3 Temporal Resynchronization and Correction

For temporal resynchronization of both detectors, a special time-correlated single-photon counting (TCSPC) card was used (TimeHarp 260 PICO). This card can be integrated into a measurement computer via PCI and allows the registration of electrical pulses from the SPAD camera and the infrared detector with a time resolution of 25 ps, assigning a timestamp to each pulse (32-bit data format).

To enable sufficiently long measurements, it is necessary to convert the timestamps into a sufficiently large file format. Since the 32-bit system used by the TCSPC card could only measure for $2^{32} * 25\ \mathrm{ps} \approx 0.1\ \mathrm{s}$, the timestamps were instead converted to 64-bit ($2^{64} * 25\ \mathrm{ps} \approx 5338\ \mathrm{days}$). The timestamps from the TCSPC electronics were directly converted to 64-bit via dedicated timestamps used to detect overflows.

Using the TSCPC the timestamps of the infrared photons could be registered directly, but not the visible-light/camera photons. These photons were instead temporally measured by the camera itself and assigned a timestamp (8 to 12 bits), which corresponds to the start (or end) of the measurement window. At the beginning of each measurement window, the camera outputs a trigger pulse, which is used in the originally designed LIDAR application to trigger the laser. In asynchronous QGI, this pulse is instead registered by the TCSPC card, placing it on the same time base as the infrared detections (referred to as the global time base/global timestamp).

To correlate the detections, the locally referenced timestamps of the SPAD camera must be combined with the global timestamps of the measurement windows. The number of measurement windows is used for this purpose. The camera counts the windows, and the respective window number is transmitted along with the local timestamps of the measurements. This number is then used to retrieve the global timestamp of the window from the TCSPC data, which is then combined with the local timestamp of the detection.

The problem with this method is its susceptibility to errors. The assignment of the measurement window to the global timestamp is obviously based on the chronology of timestamps and measurement windows. This means that even a single "incorrect" or missing timestamp can lead to incorrect assignments of all subsequent timestamps. This not only prevents coincidence detection (due to the falsified temporal information) but also leads to all subsequent detections being classified as noise, as uncorrelated detections are compared. This not only prevents further coincidence detection but also increases the general noise level, causing the coincidence peak to be lost in the noise.

Detailed analyses of the time capture have shown that the problem of additional timestamps (e.g., due to noise or after-pulsing) is practically nonexistent. However, the issue of missing timestamps prevailed. Depending on the detector used, approximately one timestamp is missing for every 100,000 to 1 million

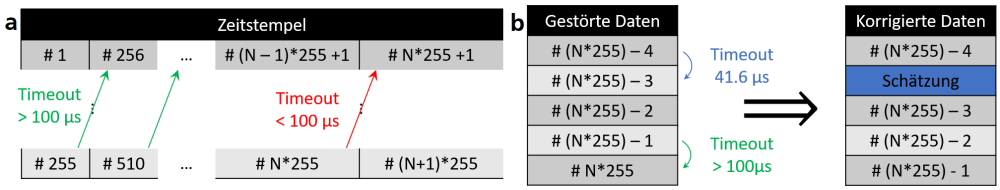

Figure 3.6: Identification and correction of missing timestamps for the single-line SPAD. (a) Due to data readout, the detector shows a significantly longer timeout after a predetermined number of measurements. Here, the number of measurements was set to the maximum of 255 frames. Afterward, the timeout between every 255th and 255+1st timestamp is checked and compared to a threshold (here 100 μs). If the timeout is below this threshold, at least one timestamp was missed in this 255-frame block. (b) Successively, the timeouts within the block are checked until the readout timeout is found. The number of iterations corresponds to the number of missed timestamps. Subsequently, all timeouts within the block are checked, and based on them, the correct timestamp is estimated.

measurements. For the 2-hour measurements in section 3.4.3, for example, approximately 840 million frames were recorded, with 881 missing timestamps—about one missing frame every 8.2 seconds. Since this time is generally insufficient to gather enough data for imaging, these missing timestamps must be detected and, if possible, reconstructed. The temporal characteristics of the camera or its frames are used for this reconstruction.

Since the 2-line detector [32] reads out the entire chip after each measurement, the timeouts between its measurement windows are very constant, at 20.8 μs, although some individual timeouts were slightly larger ($\sim$ 30 μs). This is likely due to memory access or the programming of the control FPGA, although we were unable to investigate further. However, these timeouts are not sufficient to transfer the collected data to a measurement computer. Instead, the data is stored in intermediate memory in the control FPGA. This memory is read out after a user-defined number of windows (in this work, the maximum of 255 frames) to prevent data loss. This transfer results in significantly larger timeouts of several hundred μs.

These characteristics were used to quickly detect missing timestamps by examining the timeout between every 255th and 255+1st timestamp. If this timeout deviated from the pattern, the timeout to the previous timestamp was checked until the expected timeout was found. The number of iterations indicated the number of missing timestamps x in this 255-frame block. In the next step, all timeouts in this block were examined. If enough timeouts of approximately 41.6 $(2 * 20.8)$ μs were present, additional timestamps were inserted between them. However, if no suitable timeout was found, an appropriate timestamp was inserted before the first timestamp of the block. Thereby it was assumed that the first pulse of the block was not recognized, and the corresponding timeout was lost in the readout timeout. This correction routine is shown schematically in Figure 3.6.

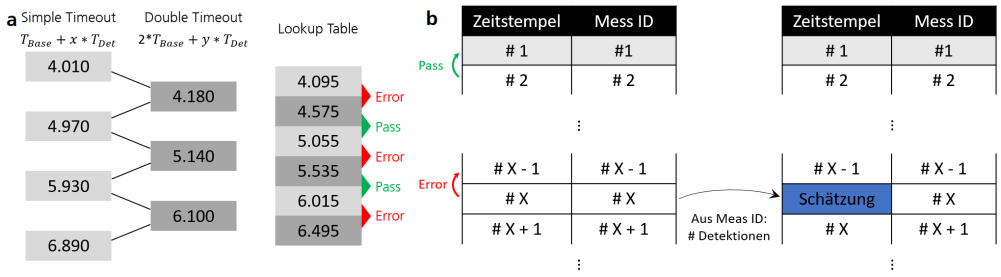

Figure 3.7: Identification and estimation of missing timestamps for the 2D detector [113]. (a) The expected timeouts between the next and second-next measurement are calculated using the median of the base timeout and readout timeouts. A lookup table is created by interpolating adjacent values, which is used to classify timeouts between timestamps. (b) The timeouts of the timestamps are classified successively. Once a missed timestamp is detected, the detection count for that measurement is checked, and the start time of the measurement is estimated.

In contrast, the 2D detector uses a special readout routine that does not read out the entire chip but only the rows with detected photons [113]. As a result, the timeouts between frames are no longer constant but depend on the number of detected photons or the detector rows with detections. Furthermore, the detector does not record a predefined number of frames before reading out its intermediate memory. Instead, the memory fills up to a specified limit and is then completely read out. Since the data size of a frame depends on the number of detections, there is no clear correlation between the memory size and the number of frames. These differences, of course, require changes to the timestamp correction process.

Through corresponding analysis, it was found that the base timeout is about 2.09 μs, with slight fluctuations from measurement to measurement. Additionally, it was found that each detected row adds an additional timeout of 960 ns, which remained constant across all measurements. Therefore, the timeout between two frames of this detector is:

$$T_{timeout} = T_{base} + x * 0.96\ \mu\text{s} \tag{3.1}$$

with $T_{base} \approx 2.09\ \mu$s and x being the number of rows with detections in the measurement window. In the case of a missing timestamp, the timeout is:

$$T_{timeout} = 2 * T_{base} + (x_1 + x_2) * 0.96\ \mu\text{s} \tag{3.2}$$

with $T_{base} \approx 4.18\ \mu$s and x_y being the number of rows with detections in the first/second measurement

window.

Since the base value fluctuates slightly from measurement to measurement but remains very stable within a measurement, the base value is first determined from the timeouts of detectionless frames. A "detectionless" frame is defined as any timeout below $2.8\ \mu$s, excluding frames with at least one detection ($\sim 3.05\ \mu$s) and double timeouts (minimum $\sim 4.18\ \mu$s). The median timeout is then calculated and used as the base timeout for further processing.

This timeout is used to calculate the expected timeouts for regular and missed timestamps according to Equations 3.1 and 3.2. A lookup table is created from this information and compared with all timestamps. This allows missed timestamps to be detected and appropriately corrected by estimating the missing timestamp. In addition to the timeout itself, the number of detected rows is also used for the estimation, which is given in the measurement data. The timeout is calculated according to Equation 3.1 and subtracted from the larger timestamp to estimate the missing timestamp as accurately as possible. The correction routine is schematically shown in Figure 3.7.

3.4 Results

The photon-pair source, SPAD detectors, and TCSPC electronics were combined to realize quantum ghost imaging for remote sensing applications. The key to this is the asynchronous detection of both partners of a photon pair and the reconstruction of their temporal coincidence. With this approach, QGI can be realized without synchronized detectors, overcoming some limitations of previous setups and enabling 3D imaging and remote sensing [20]. Since the detection of both photons is independent of each other, in contrast to the frequently used "heralded" approach, this type of setup was named "asynchronous quantum ghost imaging."

The setup is based on the temporal measurement of both photons of an entangled pair on a common time base and the comparison of their arrival times. Due to the simultaneous emission of the entangled partners (see section 2.3.1), all entangled detections show a specific time delay, depending on the flight time of the photons. In contrast, uncorrelated detections show random delays relative to each other, as they are unrelated. This effect is used to identify the entangled partners. By comparing all timestamps, a so-called "coincidence peak" appears at that specific delay, while uncorrelated photons manifest as a uniform background.

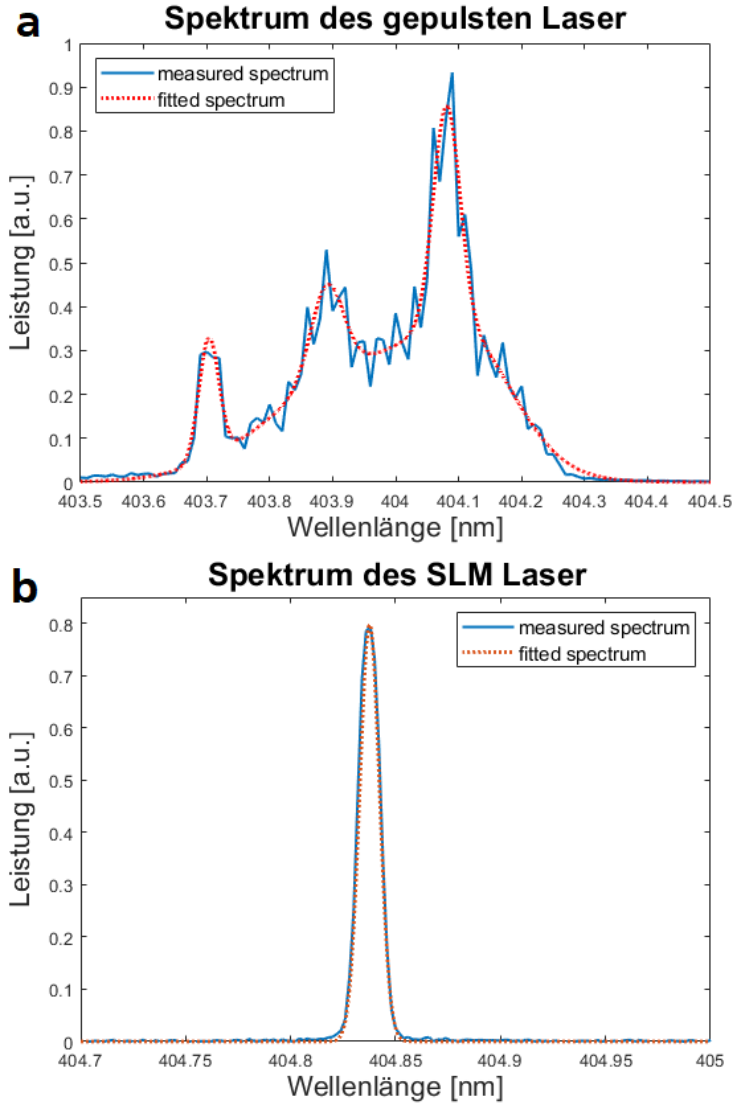

Figure 3.8: Spectra of the lasers used in this work. Both lasers were measured with an optical spectrum analyzer (OSA) and approximated by Gaussian functions for further processing. (a) Spectrum of the pulsed laser. The spectrum was averaged over several pulses and remained constant across several parameters (repetition rate, pulse width, output power). The emission clearly consists of multiple spectral lines, with the main emission at $404.1\ \mathrm{nm}$ and several side lines, with an overall width of about $0.6\ \mathrm{nm}$ and a full width at half maximum (FWHM) of about $0.25\mathrm{nm}$. (b) Spectrum of the SLM laser. The measurement yielded a central frequency of $408.84\ \mathrm{nm}$ with an overall emission width of $<\ 0.02\ \mathrm{nm}$. Due to the resolution (maximum resolution of the OSA: $0.01\ \mathrm{nm}$), this measurement only provides a lower limit for the spectral width, which is expected to be even narrower.

3.4.1 Choice of Pump Laser

Due to the cameras used for imaging, which were designed for LIDAR applications, the use of a pulsed, camera-triggered laser significantly improved the QGI setup. Since the bucket detector in the idler arm has a very long dead time ($> 2\ \mu$s), especially compared to the measurement window ($\leq 1.28\ \mu$s), a detection before the start of the measurement could block the idler detector and prevent coincidence detection. By using a pulsed laser, it is ensured that photon pairs are only generated during the camera's acquisition. Therefore, outside this window, the idler detector is only exposed to the general (negligible in these laboratory setups) background noise. This significantly reduces the probability of blocking, at least under the current low-noise lab conditions. Additionally, the number of idler detections and, consequently, the required memory is reduced, though this is of little importance due to the significantly larger data volumes of the camera.

However, using a pulsed laser does not increase the coincidence-to-accidental ratio (CAR). It merely improves the overlap of the detections, leading to more data in the coincidence time window. When using and especially analyzing the data, however, the effect of a pulsed laser on the noise distribution must be considered, as it corresponds to a convolution of two rectangular functions (see Figure 2.18).

It should also be noted that pulsed lasers should only be used for applications where the spectral properties of the source can be neglected. Since the wavelength of a pulsed laser is typically unstable and fluctuates from pulse to pulse [132], the boundary condition of a fixed pump wavelength for phase matching is blurred. This makes the exact correlation of idler and signal wavelengths only partially possible. Instead, the spectral properties within this uncertainty, which is about $0.6\ \mathrm{nm}$ for the laser used, are washed out. The uncertainty of the signal and idler photons scales approximately with the ratio of their wavelengths. Since in most spectroscopic applications the wavelength of the idler photon is determined from the signal photon, the uncertainty of such a measurement corresponds to the convolution of the individual uncertainties.

This uncertainty in spectral correlation is not only due to the uncertainty of the emission itself, but also due to the spectral uncertainty of the signal photon detection. Assuming perfect determination of the signal wavelength, this uncertainty corresponds to the indeterminacy of the pump spectrum. This indeterminacy is given by its linewidth, which describes an uncertainty in photon energy via:

$$\Delta E_{pump} = h * c * \left(\frac{1}{\lambda_{p,\ higher}} - \frac{1}{\lambda_{p,\ lower}} \right) \tag{3.3}$$

where $\lambda_{p,\ higher}$ and $\lambda_{p,\ lower}$ represent the upper and lower boundaries of the pump band. Due to the $1/\lambda$

dependence of photon energy, the uncertainty only scales approximately with the linewidth; thus, the uncertainty of the correlation can only be estimated over the linewidth for narrowband lasers.

The spectral uncertainty of the signal photon measurement is instead described by:

$$f(\lambda_{sig}) = f_{filter}(\lambda_{sig}) * f_{emission}(\lambda_{sig}) \tag{3.4}$$

where $f_{filter}(\lambda_{sig})$, $f_{emission}(\lambda_{sig})$ represent the spectral characteristics of the filter and emission, respectively. In most spectroscopic applications, however, the spectrum of the signal emission is much broader than the transmission of the filter and is approximately constant across its width. Therefore, the spectrum reduces to $f(\lambda_{sig}) = f_{filter}(\lambda_{sig})$.

The correlation uncertainty can be calculated from the phase mismatch via [133]:

$$f(\Delta\omega) = sinc\left(\frac{\Delta k(\Delta\omega)L}{2}\right) e^{i*\frac{\Delta k(\Delta\omega)L}{2}} \tag{3.5}$$

where Δk is the wave vector mismatch, dependent on the spectral mismatch of the photon energy $\Delta\omega$. By integrating over the pump laser spectrum and considering the filter function of the signal, the spectrum of the associated idler can be determined. Figure 3.9 shows this characteristic for the lasers used in this work (see Figure 3.8) and different filter widths. Due to the minimum achievable idler bandwidth of $\sim 12\ \mathrm{nm}$ with the pulsed laser (see Figure 3.9), a very narrowband SLM laser was used for the spectroscopic characterization of the source in section 3.4.5.

For imaging, however, using pulsed lasers is unproblematic, at least at laboratory-scale distances, as only the momentum correlation of the photons is used. The wavelength only has limited influence on this, via the position of the laser focus and the size of the photon momentum (see Equation 2.11). For long-distance imaging, the spectral uncertainty, as well as the bandwidth of the SPDC process, could limit the system's resolution, for example, through dispersion effects of the imaging optics. However, this influence needs to be experimentally investigated.

Recent developments in SPAD camera technology (see section 4.2.1) could make the use of pulsed lasers obsolete for many measurements.

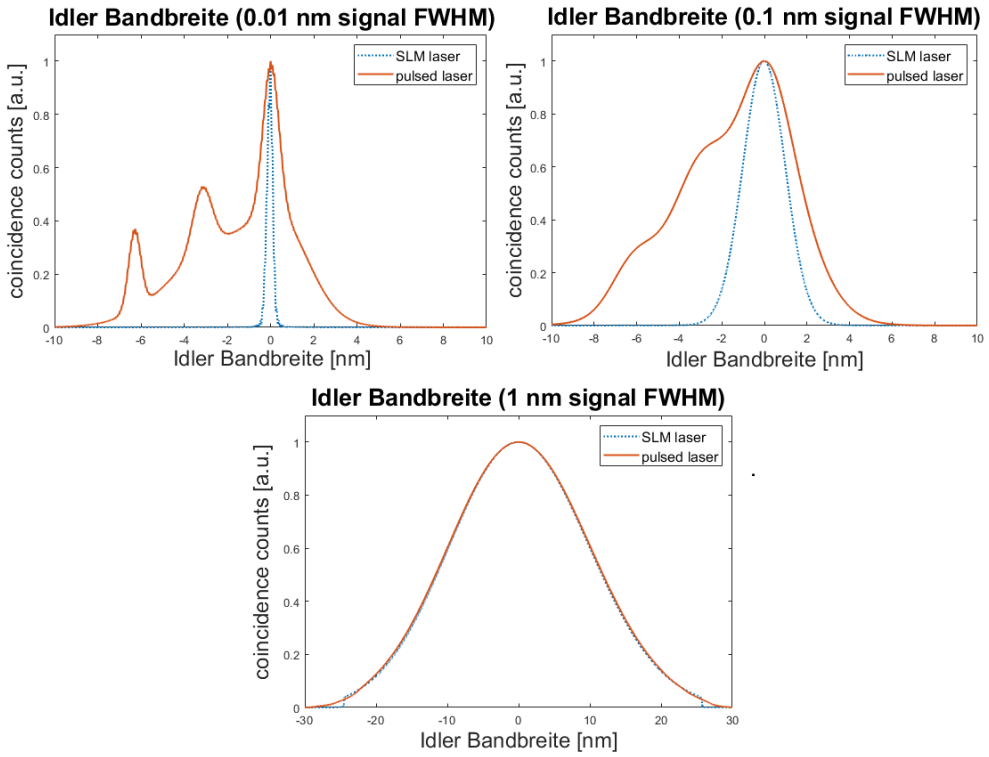

Figure 3.9: Simulation of the achievable spectral resolution of the idler, depending on the emission spectrum and signal filter bandwidth. A Gaussian filter with a freely chosen bandwidth (FWHM) and the pump spectra shown in Figure 3.8 were assumed. The spectra were normalized to the respective central frequency of the laser. From left to right: expected bandwidth of the idler/coincidence detection with filtering of the signal photons using 0.01, 0.1, and 1 nm bandwidth (FWHM). The correlation of the SLM laser is generally very fine, corresponding to the laser's bandwidth. The pulsed laser, however, is significantly broader, and its emission characteristics are clearly seen in the correlation.

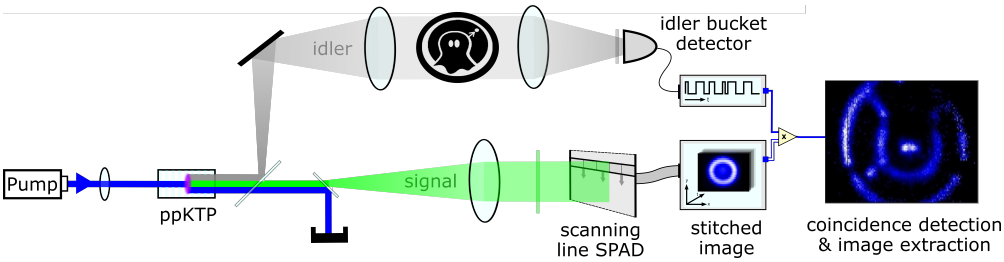

Figure 3.10: Proof-of-Concept setup for asynchronous quantum ghost imaging. To enable 2D imaging with the existing, quasi-1D SPAD array, the detector was mounted on an automated translation stage. This stage allowed the detector to be scanned vertically, with the step size adjusted to the pixel pitch of the detector. Due to the increased losses associated with scanning and the correspondingly increased measurement time, this setup was only realized in transmission [38].

3.4.2 Proof-of-Concept

As a proof-of-concept, a setup was developed that used a 2-line detector combined with an automated scan routine for imaging [127], as shown in section 3.2.

Due to the very high losses associated with scanning and the limited fill factor, this detector was only used for transmission imaging, as shown in Figure 3.10. The use of reflection, which is the main goal of this work, is theoretically possible but would require significantly longer measurement times due to the increased losses in reflection.

To analyze and optimize both the optical system and the evaluation, initial tests were performed using a cylindrical lens. In these tests, all signal photons were focused onto a single line to reduce measurement time and facilitate statistical analysis. In this way, in addition to the problems with the TCSPC card's time capture described in section 3.3, issues with the SPAD's time capture were also discovered.

Corresponding analyses of a prototype of the detector, shown in Figure 3.11, revealed an offset in the coincidence peak, depending on the values of internal registers of the measurement. Additionally, for some register values, a slight drift with increasing measurement time was observed, which, without correction, would integrate and lead to broadening and weakening of the coincidence peak. Through this analysis, a lookup table was created to compensate for both the offset and drift. As a result, the FWHM of the coincidence peak was reduced from 1.7 ns to about 400 ps.

In addition to the temporal component, initial investigations into the resolution and sharpness of the imaging were also conducted. Problems with alignment were discovered during these tests, which are

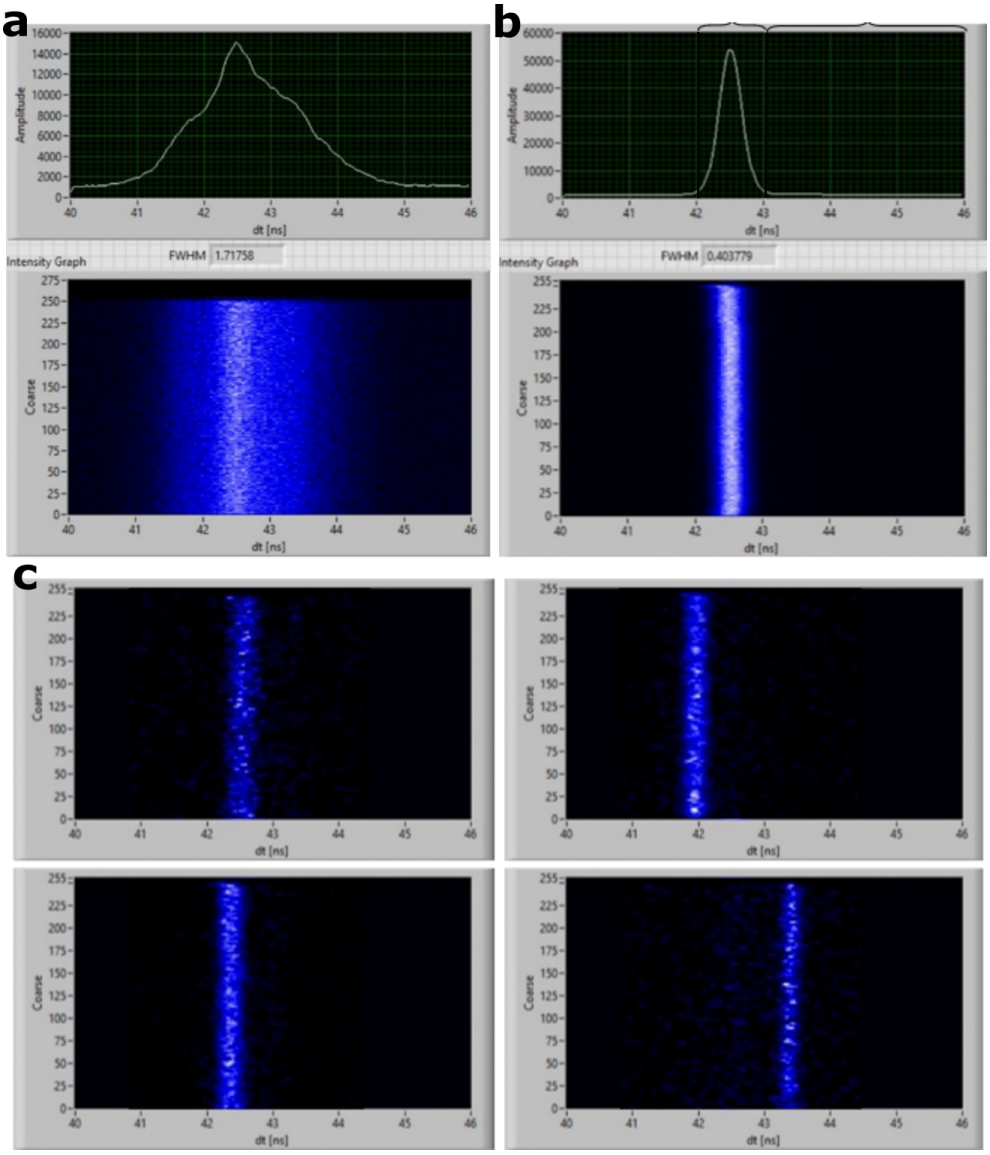

Figure 3.11: Improvement of the SPAD line's time capture through correction of temporal offsets. (a) Coincidence peak without time correction. The coincidence peak is visibly broadened and does not show the expected Gaussian behavior. (b) Corrected coincidence peak. The FWHM of the peak is approximately 400 ps, very close to the detector's minimum time resolution of 312.5 ps. (c) Coincidence peaks filtered by individual registers and displayed over the acquisition time. The different positions of the coincidence peaks, which lead to the broadening of the overall peak, are clearly visible. In addition, a temporal drift is visible in some peaks, although this is secondary in the broadening of the peak. A pixel- and time-dependent correction of these drifts results in an overall peak width of approximately 1 ns.

Figure 3.12: Results achieved with the proof-of-concept setup, shown in Figure 3.10. Two images are actually generated during measurement with this setup since the array consists of two sensor lines. However, only the image from the lower line is shown here. Further details on the measurement and image improvements can be found in the original publication [38]. (a) Coincidence evaluation of a line (line 26). The coincidence peak was reduced to 1 ns thanks to the corrections shown in Figure 3.11, and the CAR increased to about 4. (b) The transmission mask used for imaging, consisting of a "ghost." (c) Coincidence image after background subtraction and image enhancement, as described in [135]. Due to the coupling, part of the image was cut off (bottom left). The dark vertical stripes were caused by noisy pixels that were filtered during data acquisition.

discussed in more detail in section 3.4.4. However, these issues were not further investigated due to the limited significance of the one-dimensional measurement. Nevertheless, these measurements were used to align the optical system.

In the first step, the idler arm was aligned by maximizing the coupling into the fiber of the detector. For this, a collimator with a numerical aperture matched to the fiber was used, and its collimation properties were finely adjusted with appropriate alignment lasers (Schäfter+Kirchhoff 60FC-M40). As a result, the count rate of the idler detector, which depends on the collimator's coupling into the fiber, provides a good measure of the collimation of the idler emission [134].

To align the signal arm, a paperclip was placed in the idler arm, i.e., an object consisting of three parallel wires. This paperclip was aligned vertically to the focus of the cylindrical lens, so three defined stripes would appear in the coincidence image, approximately corresponding to the resolution of a 2D image. In this way, the position and orientation of the collimation lens in the signal arm and the focusing lens of the laser were further investigated and optimized.

The setup, which was aligned in this way, was then expanded with an automated stage for 2D imaging. For the proof-of-concept, the cylindrical lens was removed, and the paperclip was replaced with an appropriate mask (see Figure 3.12). With this system, images of this transmission mask with a resolution of $192\ x\ 80$ pixels were recorded. The lateral resolution was achieved by the step size of the stage used for scanning (SmarAct XYZ-CLS52:52) and matched to the pixel size. As described in [127], a pixel of this detector consists of four SPADs arranged in a row with the respective periphery, making it significantly taller in

the vertical direction ($\sim 200\ \mu\mathrm{m}$) than in the horizontal direction ($\sim 40\ \mu\mathrm{m}$). To avoid highly noisy pixels, whose probability increases with each additional activated SPAD, only one SPAD per pixel was activated. Thus, the minimum achievable resolution corresponds to the active area of the SPAD, i.e., $\sim 11\ \mu\mathrm{m}$. However, since this resolution involves considerable scanning and thus time expenditure, a scan step corresponding to a quarter of the vertical resolution of the pixels ($\sim 200/4 = 50\ \mu\mathrm{m}$) was used instead.

To generate sufficiently large datasets for coincidence analysis, each scan step was measured for 2 hours. Thus, the total measurement time for the images shown in Figure 3.12 was 160 hours, or just under a week. Due to detector issues during extended measurements, the measurements had to be restarted multiple times (from the corresponding scan step), extending the measurement time to 10 days. Due to the significantly longer measurement times for 3D imaging as a result of the associated losses, a planned application of this setup with the 2-line detector was discarded. Instead, a 2D SPAD array with lower lateral resolution was used for this demonstrator to enable imaging within a 2-hour measurement.

3.4.3 3D Imaging

To demonstrate 3D imaging, the 2-line detector was replaced by a two-dimensional array. Since this array is based on a different hardware design (see section 2.5), the correction routines and optical system also had to be adapted.

The SPADs of this detector also exhibit differences in the temporal acquisition of the pixels, mainly due to an uneven power supply to the independent ring resonators. Further influences on the temporal acquisition are detailed in [136]. However, the drift could only be analyzed in its temporal dependency, as the detection time was the only parameter transmitted by the camera. For the first, rough correction of the timing information, a correction routine developed by the chip manufacturer [113] was used. With this approach, a coincidence peak with a total width of 3 ns was achieved. This linear correction was further improved through the analysis of initial QGI measurements, allowing coincidence peaks with a total width of about 2 ns to be achieved (see Figure 3.13).

To further improve the timing, the coincidence signal was analyzed for each pixel, as shown in Figure 3.14. The optical system was adjusted so that the signal photons illuminated the entire chip, enabling a coincidence signal to be measured across the entire chip. To obtain enough data for a more accurate analysis and to avoid potential reproducibility issues, several measurements were performed and the results were summed.

The measurement data were then filtered by individual pixels, grouped by the values of the TDCs, and the groups were evaluated separately. A Gaussian distribution was fitted to the data to characterize the

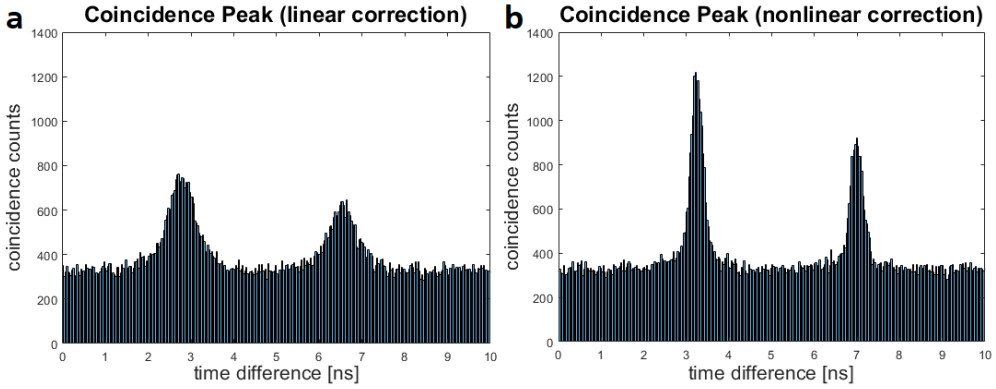

Figure 3.13: Coincidence peak of the 2D detector and improvement through drift correction. The data shown comes from the measurement in Figure 3.16. (a) Coincidence peak with linear correction. In this measurement, the TDC values were merely pixel-weighted to correct for differences in time resolution (caused by differences in the power supply, see section 2.5.2). The determination of the weighting is described in [113] but was subsequently improved through QGI measurements. (b) Coincidence peak after correcting the non-linear drift, shown in Figure 3.14 and described in [136]. The coincidence peak has been reduced to approximately 800 ps, and the CAR value has improved to around 4.

coincidence peak, and the position of the peak was determined from its mean. This position was then used to determine the temporal evolution of the coincidence peak (or its dependence on the TDC value) for each pixel. A non-linear dependence of the coincidence peak on the TDC value was identified, as shown in Figure 3.14.

To correct this behavior, it was first approximated with a second-order function, and the variables were made available for the analysis. However, due to the dependency on the pixel and TDC value, this correction proved to be very computationally intensive and unsuitable for practical use.

Instead, a fixed coincidence value was chosen, and the difference between this value and the drift for each pixel and TDC value was calculated (see Figure 3.14). With these values, a lookup table with 32x32x255 values (columns x rows x TDC values) was created, which could be used to correct the timing information.

With this correction of the drift and timing information, the total width of the coincidence peak was reduced from 3 ns to approximately 800 ps, and the FWHM was reduced from around 1 ns to 400 ps. This time resolution is very close to the fundamental limit of the SPAD camera's time resolution, which is approximately 205 ps. Based on the FWHM, this correction enables a depth resolution of around 5 cm. Additionally, the CAR value was improved from around 2 to about 4 (see Figure 3.13).

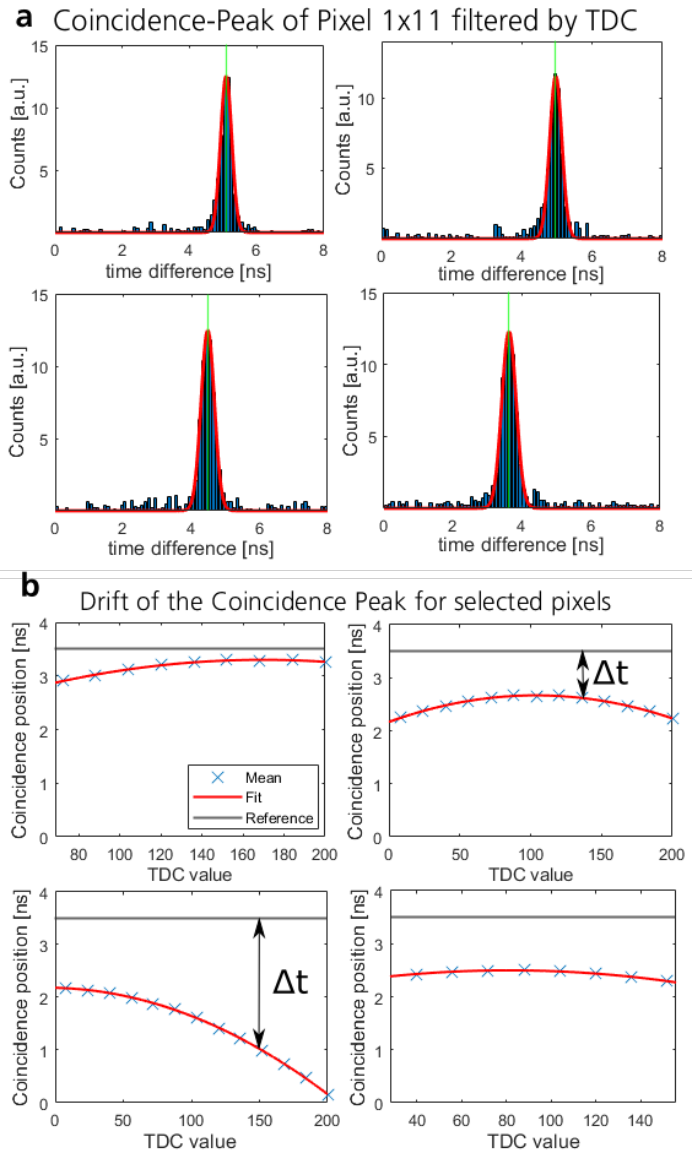

Figure 3.14: Temporal behavior of the 2D detector and drift of the coincidence peak. Since the detector only transmits the timestamp as information, only the evolution of the coincidence peak as a function of measurement time could be analyzed. (a) Coincidence evaluation for a single pixel (column 1, row 11) and selected TDC groups. A Gaussian curve was fitted to the coincidence data (red), and its mean value (green) was used for further characterization. (b) Position of the coincidence peak as a function of the TDC value of the pixel. To characterize the behavior and calculate the individual offset, the data were fitted with a second-order function. Subsequently, the difference from a general reference was calculated for each pixel and TDC value and stored as a lookup table.

Two proof-of-concept setups were designed and constructed with this detector, as shown in Figure 3.15. Since the idler detection was performed with a fiber-coupled detector, using diffuse reflection, as typically occurs in real-world applications or general 3D scenes, was problematic. Therefore, cooperative objects were used as targets in the 3D scenes, consisting of (partially blocked/prepared) mirrors and beam splitters. Their directed reflection allowed efficient detection of their return by the idler detector, but care had to be taken to ensure that the individual objects were coupled similarly well.

The name of the "Michelson setup" comes from its similarity to widely used Michelson interferometers. However, here, the interference of the idler beam with itself was not of importance. Instead, this setup was chosen because it provides two separately adjustable and optimizable arms with few optical elements.

For imaging, mirrors were used in both arms, each with attached transmission masks. These were positioned at different distances from the beam splitter, and their coupling into the idler detector was optimized individually. The distance to the beam splitter was varied multiple times to investigate the timing behavior of the camera and validate the depth information[1]. The easily determinable arm length of the setup, due to the associated time of flight of the photon , was particularly advantageous.

In order to show a more application-oriented realization of the technology, a "free space setup" was also designed, as shown in Figure 3.15. In this setup, a 3D scene was imaged, consisting of a beam splitter and a mirror that had been slightly modified (see Figure 3.17). Unlike the Michelson setup, this setup demonstrates the reconstruction of a real 3D scene, allowing to investigate limitations and improvements of the system.

With a 2-hour measurement, the results shown in Figure 3.17 were achieved. The image of the beam splitter shows the general SPAD emission, with the attached "eye" clearly visible. The image of the mirror shows the projection of the beam splitter's image onto the mirror, the taped "smile," and a second "eye." This second "eye" originates from the re-transmission of the image through the beam splitter, which is slightly shifted spatially due to the arrangement.

This shift of the incoming and outgoing beams is also indicated in the image of the beam splitter in Figure 3.17b and leads to problems with the detection of the reflections from both elements with the idler detector. Due to the arrangement of the setup (with the mirror placed behind the beam splitter), the reflections from both the beam splitter and the mirror cannot be adjusted independently in terms of coupling into the fiber of the idler detector.

Since both reflections are recorded with the same detector, they should ideally show as much spatial

[1] The non-linear correction shown in Figure 3.13 was not implemented for this measurement, as the non-linear drift was not known at the time of the measurement. Instead, the improved correction shown in (a) was investigated and validated using this setup.

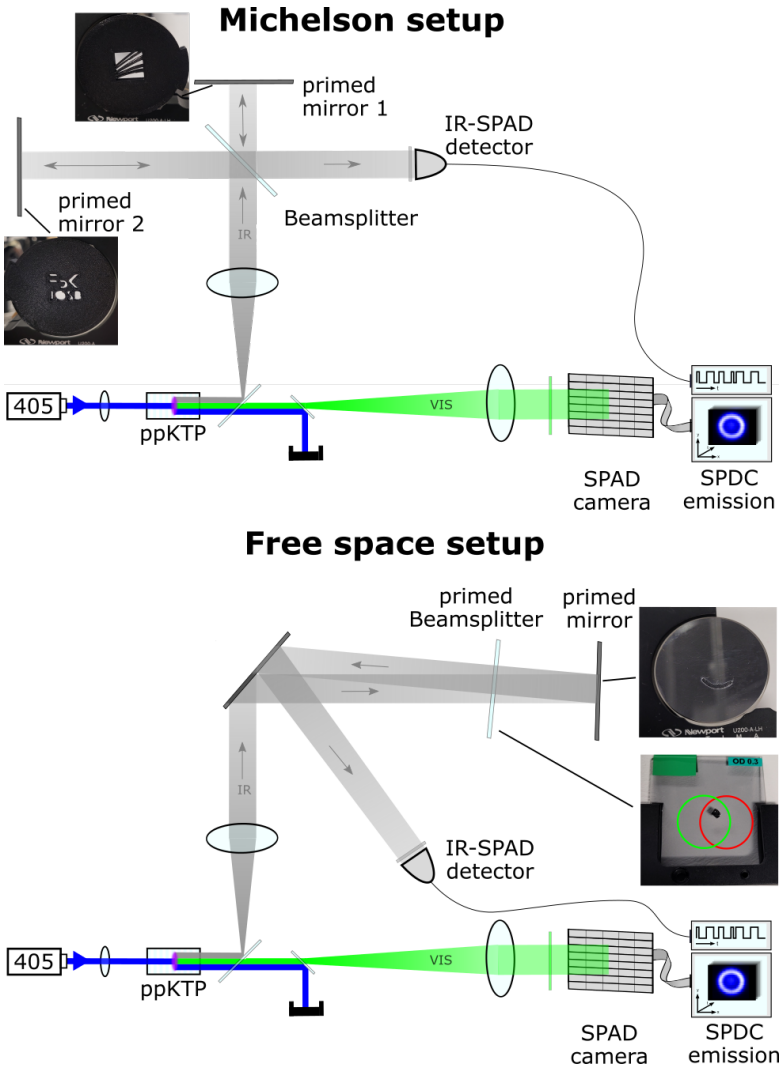

Figure 3.15: Proof-of-concept setups for 3D quantum ghost imaging. Telescopes were also used to match the SPDC emission to the detector apertures, which are not shown here. Top: Michelson setup. This setup was chosen because it provides two arms that can be adjusted independently. For imaging, mirrors with attached transmission masks featuring the logos of Fraunhofer and FBK were used. Bottom: Free space setup. This setup was chosen as a more application-oriented realization (in terms of remote sensing). A beam splitter and a mirror, which were prepared with tape, were used for imaging. The constructed scene consists of the beam splitter in the front, with the mirror placed behind it. The reflection from the mirror passes through the beam splitter again. The reflection of the beam splitter into the bucket detector is omitted for clarity. This arrangement was chosen to minimize the offset between the two reflections and to couple both as well as possible into the fiber-coupled idler detector. The spots of the incoming radiation (from the source) and the outgoing radiation (the reflection from the mirror) are shown on the beam splitter.

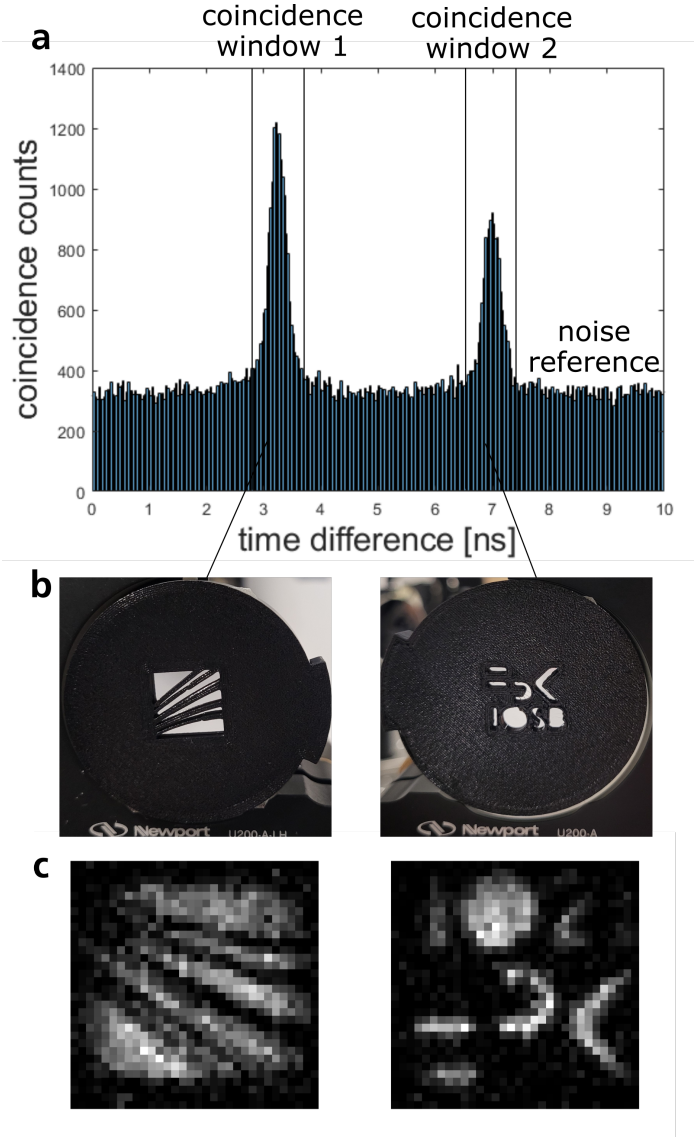

Figure 3.16: Results of the Michelson setup. (a) Coincidence evaluation of the measurement. The peaks have a total width of approximately 800 ps and a full-width at half-maximum (FWHM) of about 300 ps. To evaluate the image information, the two indicated coincidence windows, each with a width of about 1 ns, were used, while the data outside were used as a reference for background noise. The distance between the two peaks corresponds to an optical path length difference of 60 cm $(2 * 30\ \mathrm{cm})$. (b) Mirrors used for imaging. Each was covered with a transmission mask, featuring the logos of Fraunhofer and Fondazione Bruno Kessler. (c) The resulting images of the Fraunhofer and FBK masks. Both images were obtained by evaluating the indicated coincidence windows and subtracting the background noise. The letters "S" and "B" in the IOSB inscription are partially cut off due to the limited coupling of the idler detector.

overlap as possible at the detector. However, due to the different paths and path lengths, this can only be achieved with a certain angular deviation, which in turn negatively affects the coupling into the fiber of the idler detector [134].

To keep this angular deviation as small as possible, the distance between the beam splitter and mirror in the 3D scene should be as small as possible compared to the distance between the beam splitter and the idler detector. However, the distance between the 3D scene elements should not be too small, as the coincidence peaks (and thus the separation of both reflections) are only resolvable with a finite sharpness.

At the time of the measurement, the non-linear correction shown in Figure 3.14 had not yet been implemented. Instead, an (improved) linear correction of the coincidence data was applied, with which a coincidence peak width of approximately $2\ \mathrm{ns}$ was achieved. This corresponds to a depth resolution of about $30\ \mathrm{cm}$. To ensure a clear separation of the two peaks, the distance between the beam splitter and the mirror was set to $40\ \mathrm{cm}$ ($\triangleq\ 2.67\ \mathrm{ns}$). The distance required for proper coupling of both reflections to the idler detector was empirically determined to be about $4\ \mathrm{m}$. As a result, this setup had to be constructed across two optical tables.

Despite these relatively large distances, the effect of sub-optimal coupling (of the beam splitter) is clearly visible in Figure 3.17 in the one-sided "cutoff" of the SPAD emission on the left side. This becomes especially apparent in comparison with the image of the prepared mirror, the reflection upon which the detector was optimized.

Several measurements were conducted with both setups to align the optical system. The control of the source proved to be particularly critical, as discussed in section 3.4.4.

For the results shown, each measurement was taken for 2 hours using a pulsed 20 mW laser synchronized to the SPAD source[1]. The laser was focused into the crystal with a 150 mm lens, and the crystal was stabilized at $28\ ^\circ\mathrm{C}$. Both the signal and idler emissions were collimated with individual lenses (aspheres with $f = 150\ \mathrm{mm}$), and the lenses were finely adjusted using appropriate translation stages and verified through corresponding measurements. A 2.5:1 telescope was also set up in front of the signal camera to match the SPDC emission to the aperture of the SPAD camera. A similar adjustment was not necessary for the idler detector's collimator.

Using these setups, 3D imaging was achieved with a time resolution (FWHM) of about $300\ \mathrm{ps}$ and thus a spatial resolution of approximately $5\ \mathrm{cm}$. The CAR was similar in both measurements at around 4, but the number of coincidence photons was approximately three times higher in the free space measurements.

[1] 20 mW corresponds to the "peak power" of the top-hat profile

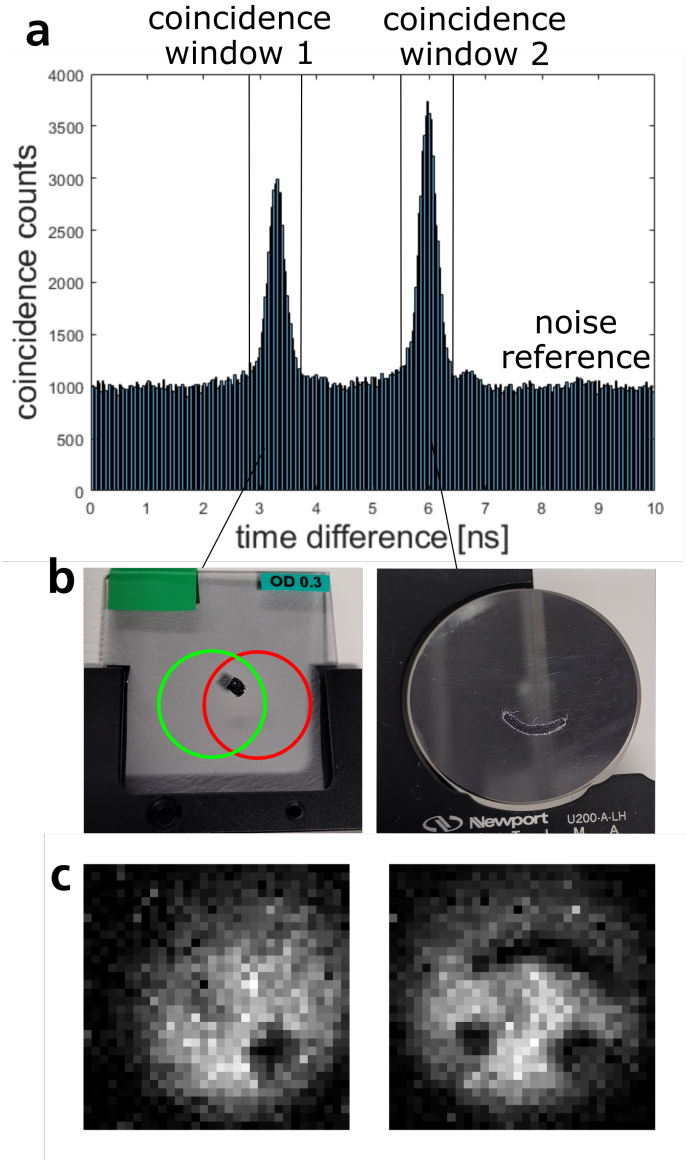

Figure 3.17: Results of the free space setup. (a) Coincidence evaluation. As in Figure 3.16, a coincidence peak of 800 ps total width and 300 ps FWHM was achieved with this setup. The distance between the two peaks corresponds to approximately 2.7 ns or 40 cm distance between the mirror and beam splitter. (b) The beam splitter and mirror used for imaging. The beam splitter was decorated with an "eye," and the mirror with a "smile." The spots of the incoming and outgoing beams are also marked on the beam splitter (see Figure 3.15). (c) The obtained coincidence images. The image of the beam splitter clearly shows the "eye." The image of the mirror shows the same eye, the "smile," and a second "eye," resulting from the spatially slightly offset re-transmission of the beam through the beam splitter.

This is primarily due to the inherent losses in the Michelson setup's design, as well as the increased losses from the masks. In the Michelson setup, a reflective ND filter ([137], ND 0.3) was used as the beam splitter, which at 45° corresponds to about a 55:17 $(T : R)$ beam splitter. This means that only about $19\ \%$ of the idler photons reach the bucket detector, calculated as $2 * (T * R)$.

In the free space setup, however, the losses were limited to those from the mirror's reflection through the beam splitter (excluding fiber coupling losses). The same ND filter was used, but its reflectivity increases to about $30\ \%$ for perpendicular incidence[2], corresponding to a 55:30 beam splitter. Therefore, the transmission to the bucket detector can be estimated as $R + T * T \approx 60\ \%$.

In total, for the Michelson setup, 22,372 detections were used for the first image and 18,799 for the second image. The background noise was estimated at 10,929 detections, so the actual coincidences amount to 11,443 and 7,870 detections, respectively. This gives an average photon count of approximately $11.2(7.7)\ \mathrm{photons/pixel}$ for the images. In the free space setup, 59,846 (68,568) photons were used from the coincidence windows, overlaid with an estimated 33,059 noise events. The coincidence images thus consist of 26,787 (35,509) coincidence photons, or about $26.2(34.7)\ \mathrm{photons/pixel}$.

The object itself was illuminated with approximately $1 * 10^6\ \mathrm{photons/s}$[3] over a spot diameter of approximately $1\ \mathrm{in}$ ($\approx 6.5 * 10^{-4}\ \mathrm{m}^2$). This gives an illumination intensity of about $1.54 * 10^9\ \mathrm{photons/s/m}^2$, which corresponds to roughly $1 * 10^{-9}$ times the natural daylight illumination at 1550 nm [139], assuming a 1 nm filter, or roughly the illumination of a moonless night [140]. Using a continuous-wave (cw) laser, the photon rate would be about 100 times higher, approximately $1.5 * 10^{11}\ \mathrm{photons/s/m}^2$. Even with this increase, the illumination intensity would still fall below the sensitivity threshold of even modern infrared cameras [13], thereby enabling significantly more sensitive investigation methods.

Due to the extremely low photon dose, these QGI setups are particularly suitable for applications where illumination power is severely limited, such as investigating phototoxic materials. Another advantage is the spectral breadth of the emission, which will be further investigated in section 3.4.5. Corresponding concepts for using spectral correlation are also discussed in chapter 4.1.

3.4.4 Resolution

In the "far-field" setup, control of the laser focus is crucial, as even small misalignments significantly blur the correlation, resulting in loss of image information. To investigate this effect, the setup shown

[2] The manufacturer provides only the reflectivity at 45°; for the reflectivity here, measurements of a similar filter were assumed, [138]

[3] Estimated from detection rate, efficiency, fill factor, and duty cycle of the laser and detector

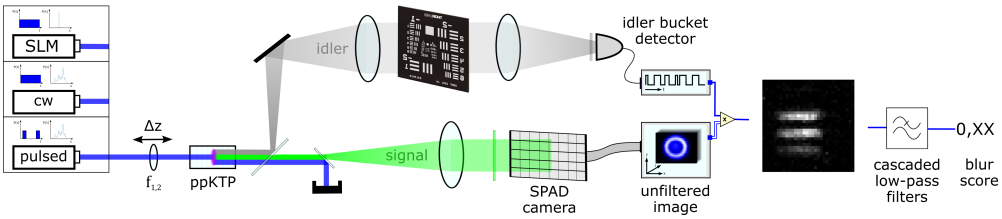

Figure 3.18: Setup for investigating resolution, depending on the focus of the laser. To analyze the laser's influence, both lasers were used for the measurements, with the OBIS laser operated both in pulsed and cw modes. Additionally, two different focusing lenses with $f_1 = 100$ mm and $f_2 = 150$ mm were used to investigate the influence of focusing. This lens was moved along the propagation direction in each case to shift the focus position. A USAF target was used as the object, where, due to the limited resolution of the SPAD camera, the largest pattern was selected for imaging. The resulting image was then filtered with several low-pass filters and compared with itself, providing a measure of the image sharpness [141]. A 2 mm-long crystal was used as the photon-pair source in all laser measurements.

in Figure 3.18 was used, where the pump lens was moved along the direction of the laser propagation, thereby shifting the position of the focus. It should be noted that, due to the limited resolution of the camera used, these results only allow (rough) qualitative conclusions regarding the resolution capability.

A standard USAF target was placed in the idler arm for imaging, and the resulting image was evaluated in the signal arm. Due to the low resolution, a method based on low-pass filters was used to estimate the resolution, rather than the more commonly used edge detection. In this method, the image is filtered with several low-pass filters and compared to the original image. Since sharp images have stronger edges, they are composed of higher spatial frequencies, and thus are more significantly affected by low-pass filtering. This change provides a measure of image sharpness, or the blurring caused by focus misalignment. For comparability of the values, it is crucial that the same section of the target is evaluated consistently, as changing the stripe spacing would significantly affect the image frequency and distort the measurement.

As shown in Figure 3.19, even a slight shift of the pump spot outside the crystal leads to a blurring of the resulting image, up to the complete loss of information. It also becomes clear that this effect is more pronounced with stronger focusing. An interesting aspect of these experiments is that neither the count rate of the SPAD camera nor the general SPDC emission visible on the camera changed significantly during the tests[4]. Only the "filtered" image and the count rate of the fiber-coupled bucket detector changed during the tests, which can be explained by the coupling of the bucket detector into the fiber.

This blurring effect can be explained by the blurring of the momentum correlation due to the pump

[4]Except for slight lateral shifts due to lenses not being optimally centered

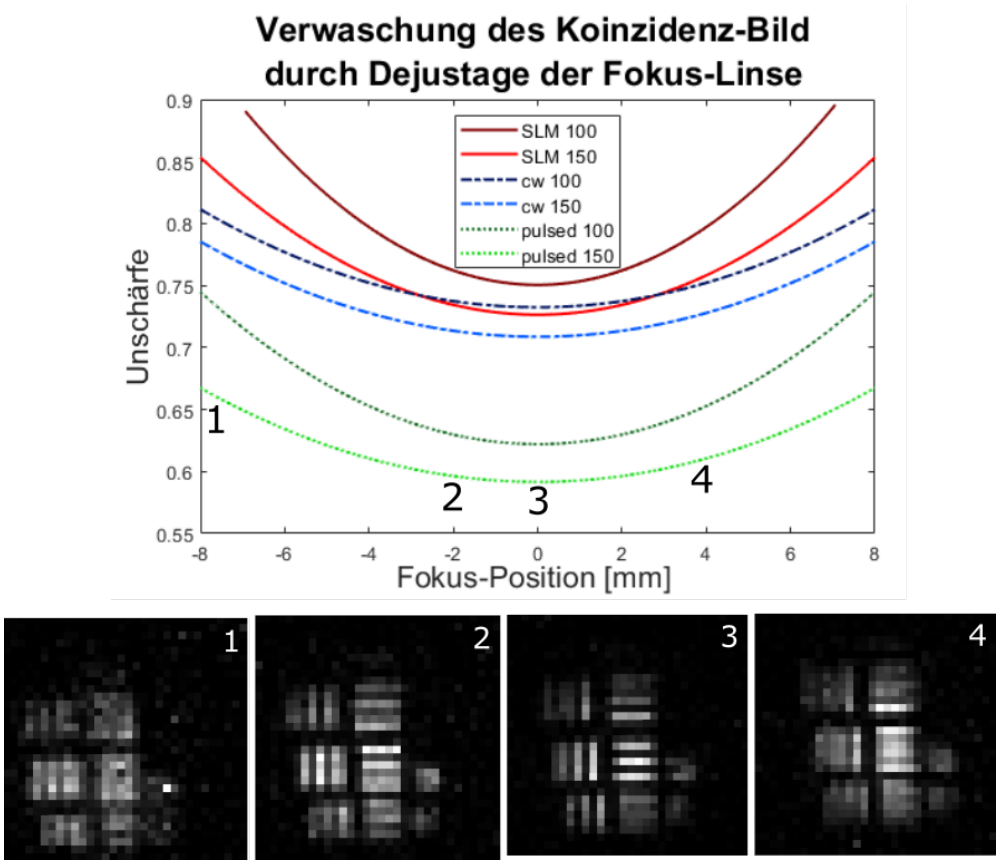

Figure 3.19: Results of the resolution investigation. Top: Evaluation of the "blur score" for different lasers and focusing lenses. The influence of stronger focusing is evident by a steeper curve and thus lower tolerance for misalignment. The measurements of the pulsed laser, due to the larger number of coincidence detections, were less noisy and therefore scored significantly better than the cw mode and SLM laser data. Bottom: Images of a detailed section of the target at different focus positions. The corresponding positions are marked in the "blur score" evaluation, but the evaluation itself was applied to a low-frequency section of the image, as shown in Figure 3.18.

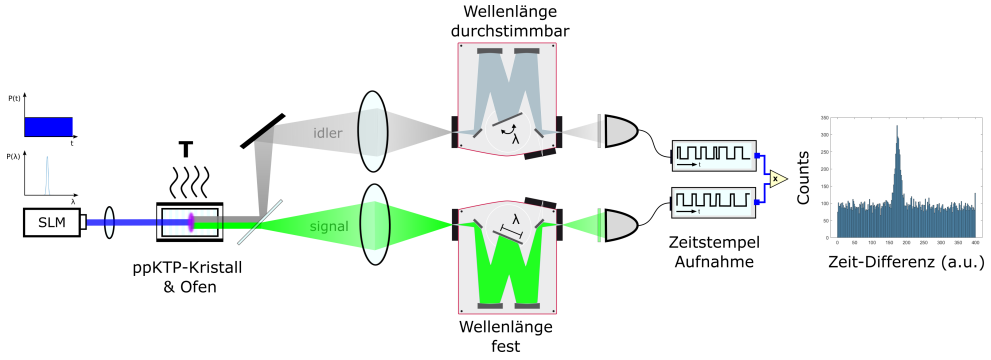

Figure 3.20: Setup for investigating the emission spectrum and spectral entanglement. The temperature of the crystal is varied parametrically to shift the phase matching and thus the emission spectrum (see section 3.1). To measure the general idler spectrum, a programmable monochromator is placed in the idler arm, and its wavelength is varied parametrically. To characterize the entanglement, a second monochromator is used in the signal arm as a fixed spectral filter. From the general count rate of the idler detector, the emission spectrum can be determined, while the entanglement is characterized by the coincidence signal (CAR).

beam's unfocused momentum. Since the wavefront of the beam is flat only in the focus of the laser beam, only there the directions of all photons are the same. When the phase front is curved, the momentum correlation becomes ambiguous, and the image information in the far-field setup is destroyed [142, 143].

However, this effect can also be used advantageously. Shortly after the first publications on quantum ghost imaging, Pittman et al. [83] began working on concepts for lensless imaging using a focused laser. With this, a clear position correlation can be achieved in a plane for both the signal and idler photons, corresponding to the curvature of the pump beam's wavefront. Furthermore, the object in the camera arm is magnified according to the pump focus, similar to the magnification of the object in relation to the wavelength that is achieved in the focus (see section 3.1).

3.4.5 Spectral Properties

To investigate the spectral entanglement of the photon pairs, the setup shown in Figure 3.20 was used. Two monochromators were employed, one in the idler arm and one in the signal arm, to filter the respective photons spectrally with fine resolution and tunability. The filtered emissions are then detected by simple bucket detectors, and evaluated via coincidence analysis.

The aim of this setup was to demonstrate the spectral shift of the emission with crystal temperature, while

preserving the spectral information from the filtered signal photons. The signal emission was filtered with a monochromator at a fixed wavelength (Mini-Chrom monochromator, slit width $100\ \mu\mathrm{m} \mathrel{\widehat{=}} 0.73\ \mathrm{nm}$ resolution), while an automated, tunable monochromator with adjustable resolution (Bentham TMc150) was used in the idler arm. Further investigations into the spatial-spectral distribution of the emission, as described in section 3.4.1 and [16], are planned but have not yet been completed. Additionally, as high temperatures are expected to cause issues with the coatings of the crystals used for imaging, they were replaced with uncoated $5\ \mathrm{mm}$-long crystals.

To avoid issues with alignment and ensure optical isolation, the measurements were largely automated. The programming interface of the idler monochromator was used to scan the idler spectrum while stabilizing the crystal at a specific temperature. From the count rate of the idler detector as a function of the monochromator's wavelength, the general idler spectrum can be determined, while the coincidence analysis (CAR) characterizes the spectral entanglement (see Figure 3.21 and section 2.3.1). The expected spectrum can be estimated based on the considerations in section 3.4.1.

To characterize the entanglement, the idler monochromator was scanned with a step size of 1 nm. In order to gather sufficient data for coincidence analysis, each point was measured for 400 seconds. To minimize background noise and conduct the measurements undisturbed, they were performed at night in a darkened lab.

The results of the measurements at various crystal temperatures are shown in Figure 3.21. It shows how the general idler spectrum shifts significantly with crystal temperature, while the position and shape of the coincidence signal remain largely unchanged. The width of the coincidence peak, with a full width at half maximum (FWHM) of approximately $7\ \mathrm{nm}$, corresponds well with the signal estimated in section 3.4.1, assuming a $0.73\ \mathrm{nm}$-wide Gaussian filter in the signal arm. The slight broadening of the measured coincidence peak compared to the simulation can be attributed to the assumption of a perfect Dirac-function filter for the idler in the simulation. In reality, the idler is subject to a (relatively narrow) Gaussian filter characteristic, which causes a slight broadening of the signal.

The spectrally resolved coincidence peak was reproducible at various crystal temperatures, with neither the position nor the shape of the peak changing significantly (see Figure 3.21b). The coincidence-to-accidental ratio (CAR) was generally constant across most measurements but showed a significant increase, from around 2 to 6, particularly at crystal temperatures of $85\ ^\circ\mathrm{C}$ and $95\ ^\circ\mathrm{C}$. This increase does not result from an improvement in entanglement or the measurement itself, but rather can be explained by the shift in the emission spectrum.

As the detected photon rate decreases, the background noise in the coincidence time window also drops, leading to an improvement in the CAR, despite the coincidence signal itself weakening. This is also reflected in the shift of the coincidence maximum to higher wavelengths, where the emission

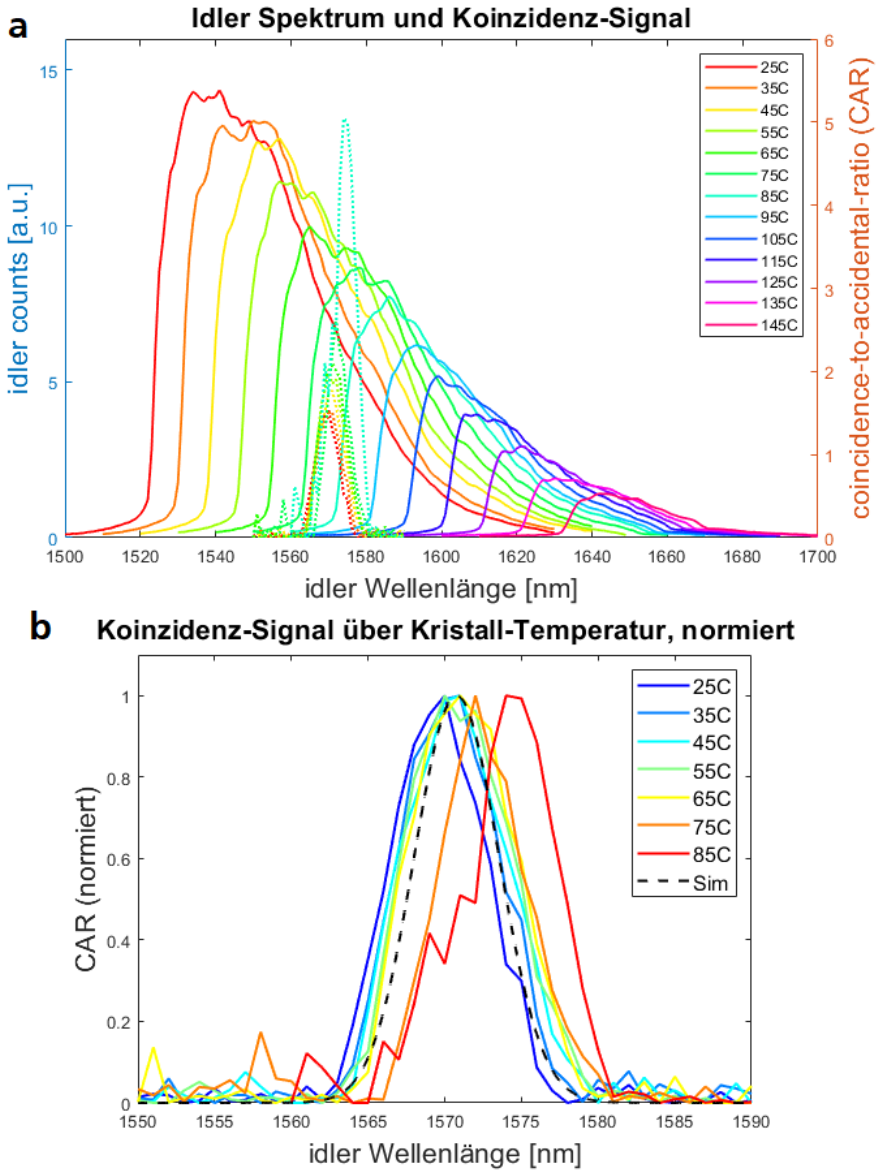

Figure 3.21: Results of the spectroscopic investigation of the photon-pair source at different crystal temperatures. (a) Measured general emission spectrum and coincidence signal at different temperatures. The idler photons were scanned in 1 nm steps, with each wavelength measured for 400 seconds. The signal photons were filtered at 546 nm with a 0.73 nm FWHM filter. (b) Measured coincidence distributions, compared to a simulation based on section 3.4.1. The emissions were normalized to their respective maxima. The coincidence peak shifts with temperature due to the change in overall detection rate at the corresponding wavelengths.

spectrum's edge appears in the measurement window, reducing noise from lower-wavelength emitted photons. Additionally, the probability of detecting both photons of a pair increases, as the dead times of both detectors play a lesser role. A similar, though inverted and much less pronounced, shift can also be observed at lower temperatures. This shift arises from the drop in detection rates at higher wavelengths at these crystal temperatures. It is therefore essential, when evaluating such measurements in a spectroscopic context, to interpret the results carefully and consider these effects.

The filters typically used in the idler arm cut off the spectrum starting from approximately $1620\ \mathrm{nm}$, which distorts the measurements. Therefore, they were removed. Nonetheless, the idler arm measurement is still limited by the (spectrally dependent) detection efficiency of the idler detector. The detection efficiency of the InGaAs-SPAD used in this work drops significantly beyond $1600\ \mathrm{nm}$ [120], effectively truncating the measured spectrum. To estimate the true emission, the measured spectrum was weighted by the detection efficiency and is shown in Figure 3.22.

It is also suspected that the measurements at higher crystal temperatures are subject to increasing losses. The spectral filtering of a monochromator relies on focusing the light onto a very small slit (width $< 100\ \mu\mathrm{m}$), making the position and size of the focus crucial. Since the idler photons are collimated and focused through multiple dispersive optics, the focus is expected to shift slightly with wavelength. Therefore, it is likely that the setup becomes increasingly misaligned at higher temperatures. This effect is planned to be examined in further investigations.

In particular, the spatial-spectral distribution of the photons, as described in section 3.1 and [16], will be investigated. For this, the VIS monochromator will be replaced with a 2D-SPAD array, and the emission will be imaged via QGI. It will also be explored whether this distribution affects the measurements presented here, for example, through the coupling into the monochromator slit. In this way, the spectroscopic measurements and especially the real emission spectra estimated in Figure 3.22 will be verified. These measurements are currently being planned and are set to begin shortly.

For validation, the measurements were compared with the temperature-dependent phase matching shown in Figure 3.3, as depicted in Figure 3.22b. The end of the signal rise shown in Figure 3.21 was used as a benchmark, as this is where the collinear emission is assumed to occur, to which the phase-matching curve corresponds. As seen in Figure 3.22b, the measurements align well with the prediction, though they show a slight offset. This offset is attributed to uncertainties in determining the idler wavelength, particularly in the central frequency of the filter. The exact uncertainty of the grating used is unknown but is estimated to be around $1\ \mathrm{nm}$. The determination of the collinear emission is also influenced by the drop in detection efficiency at higher wavelengths, as well as a shift to higher wavelengths due to the overlap of the corresponding emission (similar to the CAR evaluation in Figure 3.21).

The idler wavelength measurement is inherently described by a Gaussian function, given by the filter

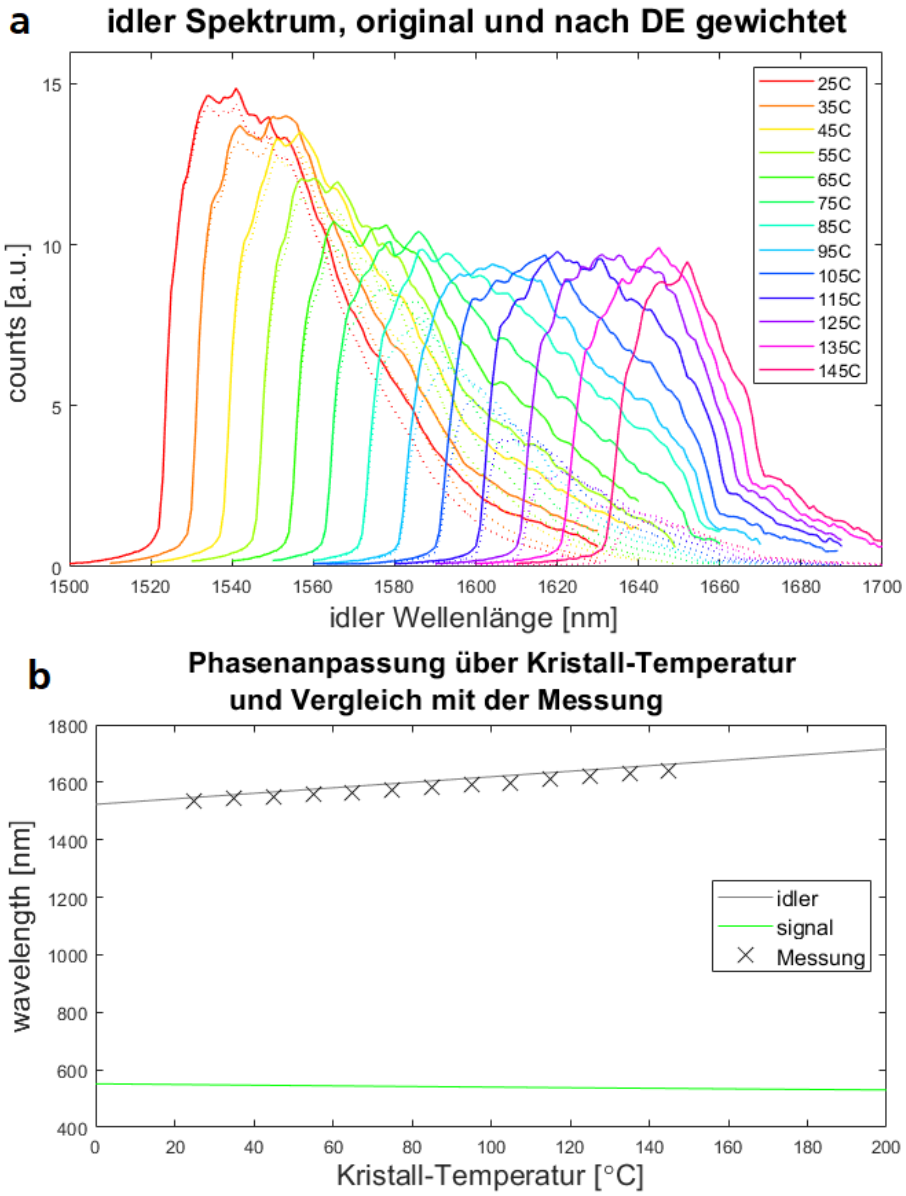

Figure 3.22: Interpretation of the results of the spectroscopic investigation. (a) Estimated (l) and measured (:) idler spectra. To estimate the true idler spectrum, the measured spectrum was weighted with the detection efficiency of the idler detector [120]. (b) Comparison of the measurement (X) with the idler spectrum calculated from phase matching (l) (see section 3.1). The measurements align well with the expected characteristics, with the offset likely due to the limited calibration of the monochromator's central wavelength.

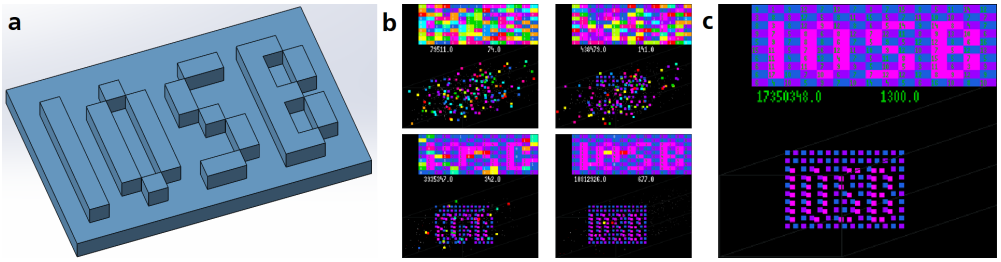

Figure 3.23: Simulation of the evolutionary algorithm. For this simulation, a target object was provided, and the timestamps of the detections were statistically distributed based on the measurements from section 3.4.2. (a) Object used for imaging in the simulation. (b) Evaluation of the evolutionary algorithm at various stages of evaluation. (c) Final result of the evaluation.

characteristic of the idler monochromator (FWHM approximately $1\ \mathrm{nm}$). It is expected that the collinear emission determined in this way will be slightly shifted to higher wavelengths, as it is overlapped by emission from non-collinearly emitted, longer-wavelength photons (see also Figure 3.4 and [16]). This effect can also be seen in Figures 3.21 and 3.22, in the "bending" of the signal edge just before the maximum. The effect is estimated to be less than $1\ \mathrm{nm}$ and will be addressed in the investigations into the spatial-spectral distribution.

3.4.6 Automated Coincidence Analysis and Object Recognition

In this work, the scenes and objects used were known in advance, so the positioning of the coincidence peaks was trivial. This allowed for significant reduction of the data and computational load by filtering the data accordingly. However, as the original goal of this work was to image "real" 3D scenes that were unknown prior to the measurement, methods for automated coincidence analysis and object recognition were also considered as managing and evaluating large datasets requires appropriate methods.

For evaluation, an evolutionary algorithm proved highly suitable, an area in which the research group already had expertise. An appropriate algorithm was also developed in the course of this work, although the primary work was done by a colleague. This algorithm will be briefly described here, but will not be discussed in detail, due to a potential planned patenting process.

Evolutionary algorithms are optimization methods inspired by natural evolution. Candidate solutions (in this case, a combination of signal and idler detection) are randomly modified ("mutated") and evaluated

using a fitness function. Mutations can have positive, negative, or neutral effects on the result. By combining ("recombining") various successful mutations, the result (in this case, the detected object) can be progressively improved, generation by generation. More detailed information about evolutionary algorithms and their limitations can be found in the literature, e.g., [144, 145].

The central problem in coincidence evaluation can be described as the detection of discrete objects within the detection data. Therefore, not only the detection time but also the spatial information is used for evaluation, with the assumption that a detected object has a closed surface. This assumption is represented in the algorithm by spatial "clustering" of the detections.

Additionally, the depth information of the detections is used for evaluation. It is assumed that a closed 3D object has a gradually changing surface over its depth. In the algorithm's programming, this assumption is taken into account by incorporating the temporal evolution of the coincidence images into the fitness function. Jumps in the time or image information relative to the estimated object negatively affect the evaluation, while detections that are spatially and temporally close to each other have a positive impact. A more detailed description of the problem and the corresponding fitness evaluation can be found in [146].

Depending on the application, i.e. in cuvette analysis, this assumption may not hold. For such applications, the algorithm would need to be adapted and optimized for a suitable fitness function. For test cuvettes, for example, it could be optimized for the spatial distribution of the cuvettes themselves, providing a spatial reference.

A simulation of the algorithm is shown in Figure 3.23. The displayed object was simulated as a coincidence dataset, with the timestamps statistically distributed based on the measurements in section 3.4.2. The CAR matched the measurements, with a value of about 4.

4 Further Developments and Outlook

In addition to the realization of the asynchronous quantum ghost imaging setup, this work also involved an investigation in possible adaptions of both individual components and the entire setup. The goal was not only to improve the setup itself but also to identify other potential problems and application areas and design appropriate solutions. The development and investigation of these setups beyond the concepts and boundary conditions would exceed the scope of this work, but some are (partially) planned at Fraunhofer IOSB.

4.1 Setups

Of particular interest for the further development of the setup are the spectral properties of the photon-pair source. As already shown in Section 3.4.5, the emission spectrum is controlled by phase matching and can be modified by the crystal's temperature. Moreover, unlike a laser, the spectrum is not dependent on the discrete energy levels of the crystal but can cover the entire electromagnetic spectrum. Thus, the emitted spectrum can be very broadband, while the spectral entanglement of the photon pairs can be very narrowband if the right laser is used (see Section 2.3.1).

The usable spectral range is limited only by the transparency of the crystal material and the achievable poling period. However, the poling period itself is only a minor limitation, as higher-order periods can also be used, although the efficiency of the SPDC suffers as a result (see Section 2.3.2).

4.1.1 Ghost Spectroscopy

For spectroscopic applications, the QGI setup can be relatively easily adapted. To do this, the signal arm is extended with a dispersive element, and the camera array is replaced with a simple linear array. The idler arm remains unchanged. The dispersive element (e.g., a diffraction grating) causes a spatial

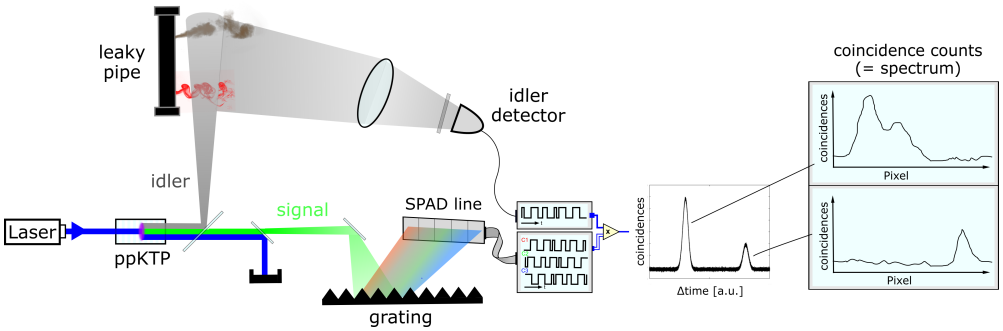

Figure 4.1: Quantum Ghost Spectroscopy using the example of a leaky pipe. Through temporal entanglement, the position of the leak can be determined using ToF (Time of Flight). Spectral entanglement is used to deduce the wavelength of the idler photon from the signal photon's wavelength and thereby determine the spectral properties of the analyte. To do this, the signal photon is spectrally split, its individual spectral lines detected using a linear array, and then compared with the bucket detector's detections. To realize spectral entanglement as precisely as possible, the pump laser must be as narrowband as possible, ideally an SLM laser. Therefore, pulsed lasers should be avoided in this case, as they usually have a broader, pulse-to-pulse varying spectrum. Accordingly, the SPAD array should also be implemented as a free-running detector. Since the momentum or position correlation of the photons is not important in this setup, at least some components can be implemented in fiber technology. This reduces alignment and energy consumption and allows for compact setups.

splitting of the signal photons, sorted by their wavelength. These photons are then imaged onto the linear array, with each pixel of the array corresponding to a specific wavelength or spectral channel of the signal photons.

In the coincidence evaluation, as with QGI, all idler detections are compared with the signal detections. However, here, the pixel position does not correspond to an image point but to a specific wavelength of the signal photons (and thus also to a wavelength of the idler photons). The size of the coincidence peak, or the CAR (coincidental-to-accidental ratio), provides insight into the object's absorption or backscattering, depending on the setup configuration. The effects discussed in Section 3.4.5 must, of course, be considered. In reflection, depth resolution of the object or its backscattering can also be achieved, enabling the investigation of complex mixtures.

A significant advantage of this setup is that the momentum correlation of the photons does not need to be preserved. This allows for the use of fiber technology for all components of this setup, enabling a highly compact, integrated layout of the entire system. In particular, the design of the SPDC source as a waveguide allows for the use of other, more widespread materials and techniques, such as those for MIR spectroscopy [147].

The design of the signal detector as a linear detector also allows for more flexibility in the design of the de-

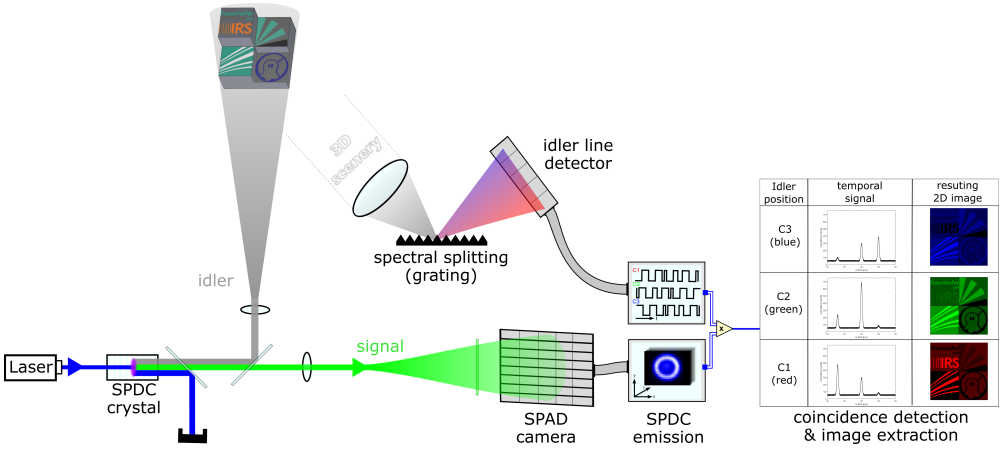

Figure 4.2: Hyperspectral Quantum Ghost Imaging. This setup is an advancement of asynchronous quantum ghost imaging, where the idler detection is equipped with spectral resolution. This is achieved by spatial-spectral splitting of the collected idler photons using a dispersive element and subsequent spatially-resolved detection. As in the setup described in Section 4.1.1, each pixel of the idler detector constitutes a specific spectral channel of the photons, whose detections are compared with all the photons captured by the camera. This setup, in contrast to conventional hyperspectral setups, allows all spectral channels to be recorded and imaged simultaneously. This setup is particularly interesting for MIR applications, as fingerprint spectroscopy is enabled in this range. However, due to the limited options for single-photon detectors in this range, the realization is problematic. One solution could be optical conversion of the photons, followed by detection, e.g., in the visible spectrum (see Section 4.2.3).

tector, promising both a larger fill factor and better temporal resolution (see Section 2.5).

4.1.2 Hyperspectral Quantum Ghost Imaging

Building on the considerations for "Ghost Spectroscopy," the QGI concept was expanded into Hyperspectral Quantum Ghost Imaging (HsQGI). To achieve this, the idler arm is extended with a dispersive element and split according to its wavelength. Ideally, the bucket detector in the idler arm would be replaced by a linear detector array to capture the emerging spectral channels in parallel. However, since these linear detectors have limited availability depending on the spectral range, a scanning approach using a single-pixel detector is also possible. Naturally, this compromises measurement time and efficiency.

Here too, all idler and signal detections are compared, where the signal position corresponds to an image point and the idler position to a spectral channel. This allows for not only depth- and spectrally-resolved

imaging but also for capturing images across the entire spectrum in parallel. Thus, transient processes can also be spectrally analyzed within short measurement times, which is a limitation of widely used conventional push-broom methods.

Since this approach enables hyperspectral imaging under minimal light conditions, it is highly interesting for life science applications and corresponding analytics, particularly in the MIR range, where hardly any camera technology exists, and the spectral range allows for molecular-characteristic fingerprint spectroscopy [148]. However, in this spectral range, the use of single-photon detectors is also limited; for instance, SPADs are currently only available up to $1.7\ \mu\mathrm{m}$ (InGaAs technology). There is potential for superconducting detectors (SNSPD - superconducting nanowire single-photon detector), which could also be used for QGI [149], as well as optical converters [71], in combination with, e.g., silicon SPADs. Both are discussed in more detail in Section 4.2.

4.1.3 Hyperspectral Single Photon Imaging

Through considerations for applications in the field of eye-care, the concept of "Hyperspectral Quantum Ghost Imaging" was adapted into a concept for "Hyperspectral Single Photon Imaging" (HSPI), as the visible spectrum is of particular interest in eye-care applications. In this case, the interacting photon can be directly captured by a SPAD camera, while the reference photon is captured by a spectrally-resolved detector. Since the image information in this setup comes from the interacting photon, it is not a "Ghost Imaging" setup.

For this reason, the momentum correlation of the photons is irrelevant, similar to the considerations in Ghost Spectroscopy (see Section 4.1.1). This offers the advantage that many components can be implemented using fiber technology. Additionally, the realization of a delay line is significantly simplified and can be determined or freely chosen, based on the fiber length.

This enables, in practical applications, the use of gated cameras like ICCDs, sCMOS, or SPADs [150, 151], allowing this method to already promise spatially and spectrally high-resolution images. The use of time-resolved SPADs would allow for the acquisition of 3D information, but the depth resolution would not be sufficient for the intended application in the eye-care field. However, the electronics required for timing significantly impact the potential resolution and detection efficiency of the camera. Gated SPADs, on the other hand, already offer good spatial resolutions with low dead times [150], enabling fast measurements. While ICCD and sCMOS promise better images due to their currently higher resolution, the relatively long dead times limit the measurement time.

Since the required measurement times and resolutions vary depending on the application, there is no "optimal" camera for this setup; the choice should always be tailored to the application.

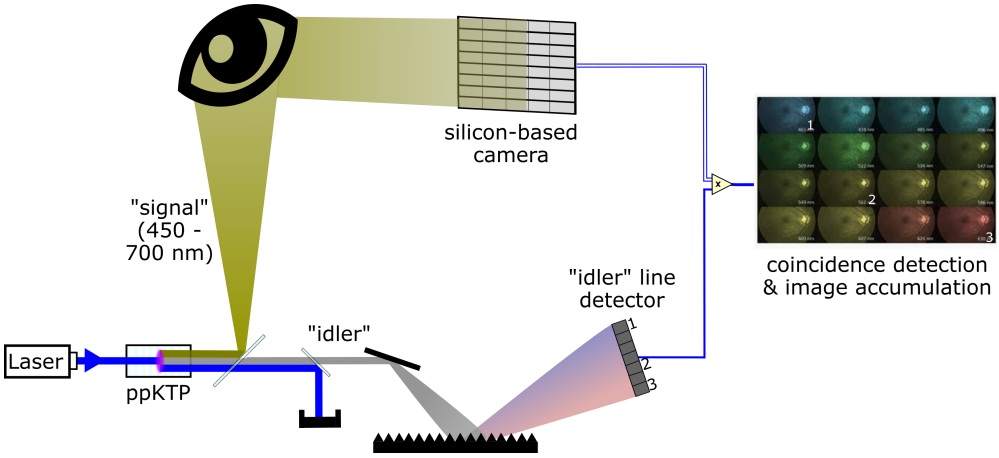

Figure 4.3: Hyperspectral Single Photon Imaging, using the example of ophthalmology. This concept was developed from considerations for hyperspectral quantum ghost imaging, for applications in the visible spectral range. However, it is not a "Ghost Imaging" setup since, in this case, the image information is obtained directly from the interacting photon, not from the partner photon. Instead, only the spectral information is obtained from the partner photon, allowing the camera detections to be spectrally classified. Since image preservation is not required for this setup, many components can be implemented in fiber technology. This also allows for easy realization of photon delays, which is why this setup could also use gated single-photon cameras such as ICCD or sCMOS or corresponding SPADs [150, 151]. The use of time-resolved detections, e.g., through IDC-based SPADs, also allows for the capture of 3D information.

As a reference spectrum, the visible range would also be suitable, based on the possible idler detectors. For a spectrum ranging from 450 nm to 900 nm, as is used in hyperspectral imaging [152, 153], a pump photon of approximately 300 nm would be required. This (UV-B) range is problematic, not only because it is partially carcinogenic but also because it leads to photodegradation and opacification in many materials. Instead, an infrared reference spectrum could be chosen, which could be well detected with InGaAs technology up to approximately 1600 nm. This would only require a UV-A laser of approximately 350 nm, which is significantly less harmful.

Alternatively, the four-wave mixing (FWM) process (χ^3 process) could be used for photon generation instead of the SPDC process (χ^2 process). In four-wave mixing, two pump photons are "absorbed" and two entangled partners, determined by phase matching, are emitted. This process is only conditionally suitable for "Ghost Imaging" because the momentum correlation is subject to significantly more degrees of freedom due to the combination of two pump photons, thus strongly influencing the imaging correlation. Additionally, the process is significantly less efficient than a second-order process, due to the use of third-order nonlinearity, or involves correspondingly high intensities.

However, it is very well suited for generating spectrally entangled partners, as the spectral correlation of the photons can be precisely determined by choosing very narrowband lasers (i.e. SLM). For example, with SLM lasers at 405 nm and 1064 nm, two highly developed laser wavelengths, photon pairs can be generated at 450 and 842 nm, covering much of the visible spectrum. However, this technology comes with many degrees of freedom and potential parasitic effects, so no further performance predictions can currently be made without experimental realization.

4.2 Detectors

The field of single-photon detection is still relatively unexplored but has shown significant interest and development, especially in recent years. This is, of course, partly due to the rapid and extensive advancements in the entire quantum field, from quantum communication to quantum sensing. Additionally, developments in nonlinear optics have increasingly found applications in recent years, enabling new measurement methods and bypassing classical limitations. Since these research fields are very dynamic, predictions about future developments and performance, particularly regarding QGI, are difficult to make. For example, SPADs from other manufacturers [36, 154] also offer single-photon imaging with picosecond time resolution, but due to hardware design, they have proven unsuitable for asynchronous QGI. Moreover, other techniques for time-resolved single-photon detection, such as TimePix chips [30, 155, 156] or Negative Feedback Avalanche Diodes (NFAD) [157, 158], could potentially be used. The following discussion, however, will focus on current developments in the field of SPAD cameras and single-photon detectors for the visible to infrared range, as this is the direction of developments currently planned at

Fraunhofer IOSB.

4.2.1 SPAD Detectors

While single-pixel SPADs are already relatively well developed, there is still significant potential for improvement in SPAD camera development. In addition to increasing the pixel count and improving time resolution and detection efficiency, increasing the camera's duty cycle is particularly interesting for QGI. A free-running detector would allow significant reduction in measurement time, reducing for example the acquisition in Section 3.4.3 from 2 hours to about one minute.

In a current project, we are working with a research partner to develop a corresponding detector. This detector promises improvements with an 80% duty cycle, 64×64 pixels, and a detection efficiency of 35%.

Additionally, this nearly 100-percent duty cycle allows the idler detections to be registered directly by the SPAD detector itself. This eliminates the need for TCSPC and global time stamps, bringing advantages in both data acquisition and processing. In particular, by eliminating the global referencing, the data format can be reduced, significantly reducing both data acquisition and storage requirements. However, the actual improvements will require corresponding investigations once this detector is developed.

For the bucket detector, multi-pixel detectors are of particular interest, both with and without spatial resolution. Spatially resolved detection is, of course, particularly required in HsQGI (see Section 4.1.2) for spectral resolution. However, it would also be interesting for HSPI, based on the wavelength considerations in Section 4.1.3.

Non-spatially resolved multi-pixel detectors, on the other hand, are used to achieve a large detection area with lower dark noise, shorter dead times, and better timing properties compared to a single SPAD with a corresponding area. A similar principle is used in the linear array from Section 3.4.2, where it is employed for background suppression in lidar [160]. These concepts are also found in commercially available silicon bucket detectors [161] and SNSPDs [162], although they are not yet widely available in current InGaAs-SPADs.

Another improvement would be the use of "open," free-space-coupled detectors instead of the fiber-coupled version used in this work. The first such detectors have recently become available [163], and acquisition and corresponding experiments are planned at IOSB in the near future.

Despite current progress in SPAD technology, most developments focus on silicon and InGaAs SPADs. These now offer very efficient and cost-effective single detectors that can operate with relatively simple or

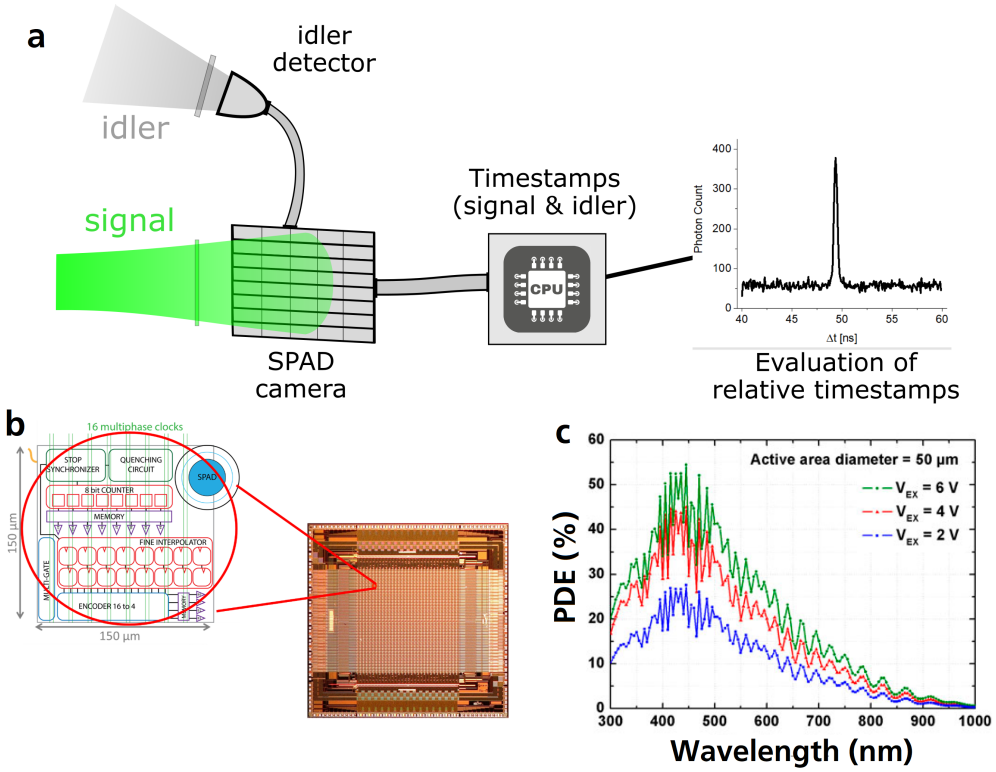

Figure 4.4: Planned future SPAD camera within the framework of the ADEQUADE project [159]. (a) Planned temporal acquisition to avoid additional TCSPC electronics. The idler detections are directly recorded by the SPAD camera and registered in its time base. This reduces data processing, as only the local time stamps from the SPAD camera need to be processed, eliminating the need for time stamp correction (see Section 3.3). This concept is made possible by the planned duty cycle of 80 %. (b) Micrograph of a current prototype of the planned detector and planned schematic of a pixel, based on [112]. The pixel's fill factor is expected to increase from approximately 3 % to 70 % through micro-lens arrays. (c) Photo-detection efficiency of the prototype detector. The DE of the future detector is expected to be similar.

even no cooling technology. However, they are limited by material properties to a spectral range of about $1.7\ \mu\mathrm{m}$. SPADs with materials having lower bandgaps (and thus longer-wavelength detection ranges) are not expected in the near future, as the exponentially increasing dark noise and the required electronic processing become problematic with decreasing bandgaps.

4.2.2 Superconducting Nanowires

Superconducting Nanowire Single Photon Detectors (SNSPD) consist of a long wire of a material that is cooled down to its superconducting temperature, filling the entire detection area. When a photon is absorbed, the wire is locally heated to the point where superconductivity breaks down, generating a detectable signal [166]. These detectors allow for the registration of photons with extremely high detection efficiency, up to 90%, and very precise temporal resolution, down to the single picosecond range [167]. Since these detectors, similar to bolometers, rely on the thermal absorption of photons, they are also capable of detecting a wide range of wavelengths [168]. They are particularly suitable for MIR detection and are used, for example, in microscopy [149].

However, these detectors are currently limited in their application. Besides the difficult and expensive cooling required in the Kelvin range, most of these detectors are fiber-coupled. This coupling is problematic for imaging, as demonstrated in this work (see [135]), due to the challenges of light coupling. However, as a reference detector, e.g., for QGS or HSPI, they would be well-suited, especially when the photon-pair source is designed using fiber technology.

4.2.3 Optical Converters

One way to overcome the lack of suitable detectors is through optical conversion (also known as up-conversion) in nonlinear crystals. This process is very similar to parametric fluorescence, which is used for photon-pair generation. However, in nonlinear conversion, a pump photon is not split into signal and idler photons. Instead, a pump photon and an incident photon are "combined" to generate a photon with a higher energy (shorter wavelength). This process is already used, for example, to convert long-wavelength MIR radiation into the visible spectrum, enabling MIR imaging with silicon detectors [71, 169, 170].

Since optical conversion and SPDC are based on the same principles, some effects and dependencies can be transferred between them. For imaging with QGI, it is particularly important to retain the temporal information of the interacting photons to enable coincidence analysis. Fortunately, this condition is inherently met by the process itself, though the accuracy of this information is limited by the dispersion

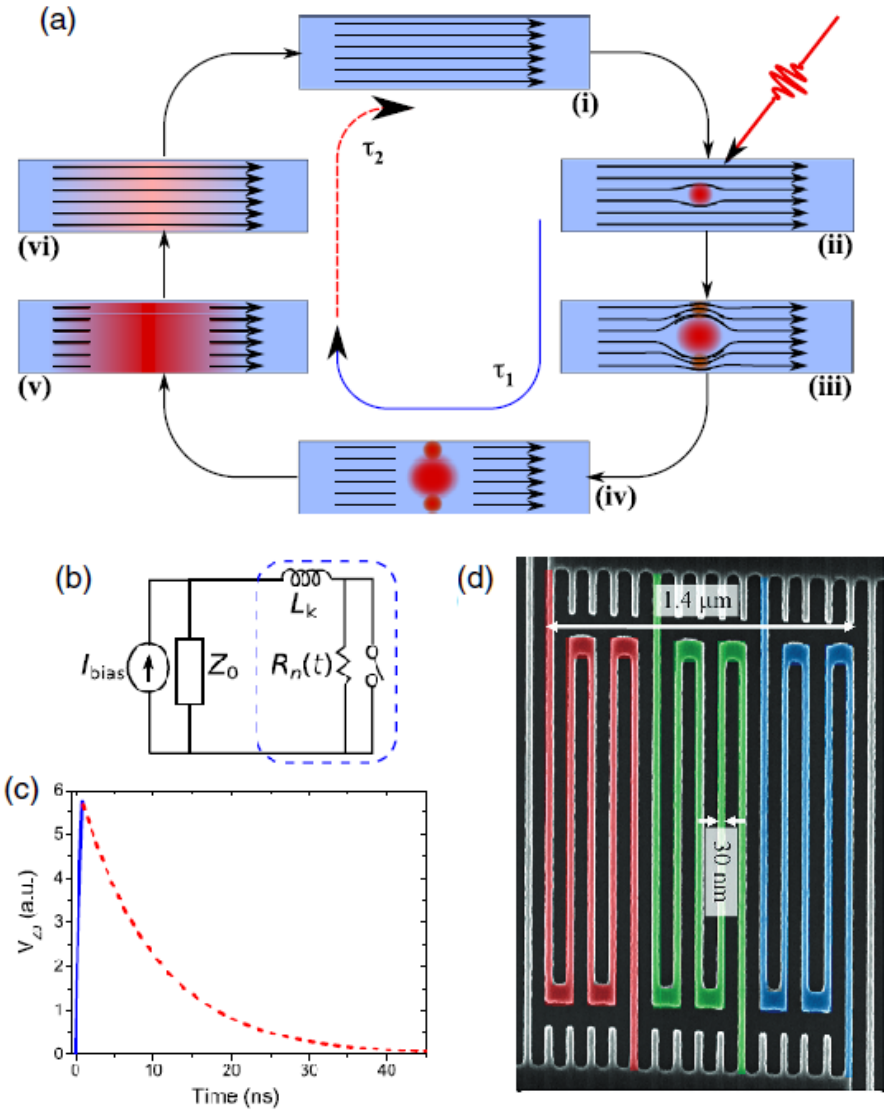

Figure 4.5: SNSPDs and their detection method. (a) Operating principle of SNSPD detection, from [164]. An incoming photon locally heats the nanowire, preventing superconductivity (ii). The heat spreads through thermal diffusion, amplified by the resistance of the local blockade, along the cross-section of the wire (iii), until superconductivity is blocked across the entire cross-section (iv). The detector's resistance increases due to the heating (v), until the detector current is interrupted. The superconductivity is then restored through cooling (vi), and the detector is ready to detect again. (b+c) Equivalent circuit diagram of an SNSPD and simulated detection cycle of the SNSPD, also from [164]. The time behavior corresponds to the phases of the cycle, indicated by τ in (a). (d) SEM image of an SNSPD consisting of three pixels (colored markings). The image is taken from [165].

of the crystals, i.e., the difference in refractive index or the speed of photons in the material. Since the location of the conversion is unknown, the resulting difference in photon speed causes the coincidence peak to "smear," estimated by

$$\Delta t = \frac{L_{crystal} * n_1 * n_2}{c * (n_1 - n_2)} \tag{4.1}$$

where $L_{crystal}$ is the length of the crystal, and n_1 and n_2 are the refractive indices of the material at the incident and converted photon wavelengths, respectively. Similar time-of-flight issues are known in superposition setups, though they are caused by the significantly smaller dispersion over the idler spectrum rather than the dispersion between, for example, visible and MIR photons [16].

This uncertainty obviously limits the depth resolution for a given crystal length or the possible crystal length for a required depth resolution.

For the setup shown in Section 4.1.2, the preservation of spectral information is also necessary. This can be ensured by using appropriately narrowband pump light sources, such as SLM lasers. Since these narrowband lasers typically have limited output power, the conversion efficiency of the upconversion process is also limited. However, this required power can be reduced through implementations such as waveguide or intra-cavity solutions. These approaches, however, come with other constraints, such as making the signal coupling more difficult and, therefore, resulting in further losses.

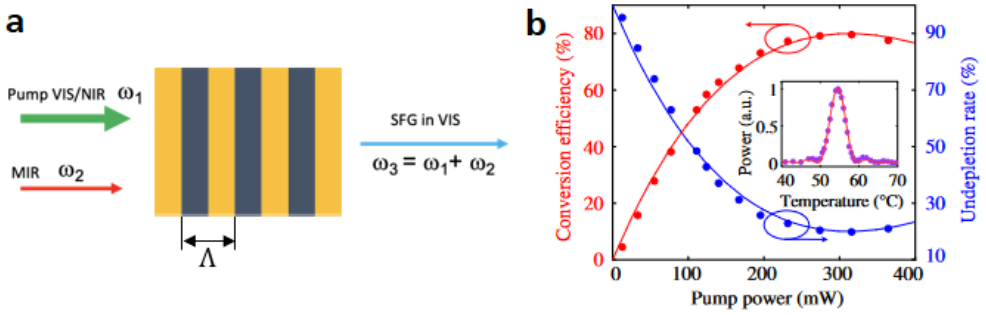

Figure 4.6: Optical conversion of MIR radiation to VIS radiation. (a) Principle of optical conversion using periodically poled crystals. As in SPDC, phase matching for a specific photon triplet is achieved with periodic poling (see Section 2.3.2). However, here, a high-energy pump photon is not split into two lower-energy photons; instead, a pump photon is combined with a signal photon to generate a higher-energy photon. For example, MIR photons between $3 - 5\mu\mathrm{m}$ can be converted into the visible range between $785 - 880$ nm using a well-developed Nd^{3+} : YAG laser (1064 nm) and subsequently detected with conventional cameras. (b) Conversion efficiency of the upconversion process in a periodically poled LiNb crystal with increasing pump power. The image is taken from [171]. However, the pump power in this graph does not correspond to continuous wave power, as synchronized pulses with picosecond lasers were used in this work. Since no repetition rate was given, it is not possible to infer the intensity in the crystal itself, but it will be orders of magnitude higher. This is particularly problematic for spectral applications, as a well-defined conversion requires a narrowband laser, which is typically limited in output power. Thus, the conversion efficiency is obviously limited. The drop at high pump powers is due to parasitic effects, such as SPDC, as described in the original publication.

5 Summary

The properties of entangled photons fundamentally allow for the retrieval of spatial, spectroscopic, and temporal information of one photon based on its entangled partner. In imaging, the ability to separate the illumination of an object from the acquisition of its image, due to the spatial correlation of the photons, is of particular interest. Quantum Ghost Imaging (QGI) is a technique that utilizes this correlation to enable imaging in arbitrary spectral ranges using advanced silicon cameras. For this purpose, a visible photon (signal) is entangled with a photon of the desired wavelength (idler), where only the idler photon interacts with the object. Subsequently, the temporal correlation of the photons is used to identify entangled partners and filter the resulting image accordingly.

The basis of the entire process is, of course, the photon-pair source, where in this work parametric fluorescence (SPDC) in a second-order nonlinear crystal was used. To demonstrate the separation of illumination and image acquisition, a periodically poled crystal was used to achieve phase matching for VIS-IR photon pairs. The resulting correlations were examined both spectrally and as a function of the pump laser's focusing, and the results were discussed. In particular, the use of a pump laser synchronized with the detector and the effects on both the correlations and the evaluation compared to using a narrowband cw laser were analyzed.

Previous setups for QGI use a "heralding" approach to limit the image acquisition to (potentially) entangled photons. However, due to the associated delay line and adjustments, this approach is severely limited in practical application. In this work, a new approach to imaging with QGI was demonstrated, where the coincidence measurement is not fixed by the experimental setup. Instead, novel single-photon cameras and time-correlated single photon counting (TCSPC) electronics are used to measure all photons in the same time frame. By comparing timestamps after the measurement, entangled photon pairs can be identified and separated from uncorrelated detections. It was demonstrated how this technique can be used in remote sensing, and how 3D imaging can be enabled through time-of-flight determination.

As the first demonstration and proof-of-concept, a system was built with a single-line SPAD detector, which was connected to an imaging system using a scanning routine. This allowed the method to be

demonstrated for the first time, and the necessary steps for resynchronization were developed. Due to the losses associated with the scanning, the setup was only used in transmission. For a demonstration in reflection, the use of a prototype 2D array with similar hardware was originally planned. However, issues in the time recording prevented its use for the technique.

Instead, the use in reflection was demonstrated with another SPAD array, based on different hardware. For this, the corresponding detector was characterized, and the relevant resynchronization routines were adjusted. To demonstrate the 3D capability and to characterize the distance information obtained from the system, a setup similar to a Michelson interferometer was realized, where the time-of-flight of the photons could be very well determined and manipulated. Additionally, the application in remote sensing with a 3D scene consisting of reflective elements was demonstrated. The demonstration with diffuse reflection is still pending but is planned after replacing the currently fiber-coupled idler detector with a free-space detector.

In addition to the originally planned application for imaging, this system also enabled the verification and correction of the time information of the detectors used. Thus, this method can also be applied to study the temporal behavior of single-photon detectors and their calibration. It is particularly advantageous that the application relies only on the temporal correlation and not on the spatial one. This allows the use of other photon sources and setup configurations, which can be adapted to various detector configurations.

Due to the significant delays in the development of the 2D detector intended for imaging caused by the COVID-19 pandemic, this work was extended to include studies on alternative configurations of the setup and detection methods. The results of this investigation were summarized, with particular interest on the acquisition of spectral information. The corresponding (qualitatively evaluated) advantages and disadvantages were presented and discussed, with the author particularly noting that no long-term statements can be made about the detection methods. This is due to the currently very active research in these areas.

List of Figures

1.1 Quantum communication setup. 2
1.2 Superposition-based quantum imaging setup. 3
1.3 Coincidence-based depth determination. 4

2.1 Examples of setups for Time-of-Flight measurement and phase comparison with modulated cw lasers. 10
2.2 Setup for Gated Viewing and diagram for determining image depth. 12
2.3 Laser scanner setup. 14
2.4 Compressive Sensing/Computational Ghost Imaging setups. 16
2.5 Setup for "Imaging with undetected photons." 18
2.6 Spontaneous Parametric Down Conversion (SPDC). 19
2.7 Refractive Indices of BK7 and KTP 20
2.8 Quasi-phase matching and its influence on phase matching. 23
2.9 Influence of poling period and crystal temperature on phase matching 24
2.10 Setup for heralded Quantum Ghost Imaging 26
2.11 Implementations of the photon-pair source and the resulting image correlation 27
2.12 Setup for asynchronous Quantum Ghost Imaging 30
2.13 Operational Principle and Quenching of a SPAD 32
2.14 Cross-section of a Thin-film SPAD and Detection Efficiency of Various Geometries . . 33
2.15 Timing characteristics of a SPAD. 34
2.16 Delay-locked-loop TDC Schaltungen. 36
2.17 TDC Design Based on Ring Oscillators 37
2.18 Coincidence Analysis Depending on Detection and Emission Characteristics 41

3.1 Setup for asynchronous Quantum Ghost Imaging. 44
3.2 Photon-pair sources used in this work. 45
3.3 Dependence of KTP phase matching on various poling periods and temperatures. 46
3.4 Spectral-spatial emission characteristics of a lithium-niobate SPDC source 47
3.5 Detection efficiency of the SPADs used in this work. 50

3.6 Identification and correction of missing timestamps for the single-line SPAD. 51
3.7 Identification and estimation of missing timestamps for the 2D detector. 53
3.8 Spectra of the lasers used in this work. 55
3.9 Simulation of the achievable spectral resolution of the idler. 58
3.10 Proof-of-Concept setup for asynchronous quantum ghost imaging. 59
3.11 Improvement of the SPAD line's time capture through correction of temporal offsets. . . 60
3.12 Results achieved with the proof-of-concept setup 61
3.13 Coincidence peak of the 2D detector and improvement through drift correction. 63
3.14 Temporal behavior of the 2D detector and drift of the time information. 64
3.15 Proof-of-concept setups for 3D quantum ghost imaging. 65
3.16 Results of the Michelson setup. 67
3.17 Results of the free space setup. 69
3.18 Setup for investigating resolution 71
3.19 Results of the resolution investigation. 72
3.20 Setup for investigating the emission spectrum and spectral entanglement 73
3.21 Results of the spectroscopic investigation of the photon-pair source. 75
3.22 Interpretation of the results of the spectroscopic investigation 77
3.23 Simulation of the evolutionary algorithm 78

4.1 Quantum Ghost Spectroscopy using the example of a leaky pipe. 82
4.2 Hyperspectral Quantum Ghost Imaging. 83
4.3 Hyperspectral Single Photon Imaging 85
4.4 Planned future SPAD camera 88
4.5 SNSPDs and their detection method 90
4.6 Optical conversion of MIR radiation to VIS radiation. 92

Bibliography

[1] A. Einstein, B. Podolsky, and N. Rosen, "Can quantum-mechanical description of physical reality be considered complete?" *Physical Review*, vol. 47, no. 10, pp. 777–780, May 1935. DOI: 10.1103/physrev.47.777.

[2] J. S. Bell, "On the einstein podolsky rosen paradox," *Physics Physique Fizika*, vol. 1, no. 3, pp. 195–200, Nov. 1964. DOI: 10.1103/physicsphysiquefizika.1.195.

[3] A. Aspect, P. Grangier, and G. Roger, "Experimental realization of einstein-podolsky-rosen-bohmgedankenexperiment: A new violation of bell's inequalities," *Physical Review Letters*, vol. 49, no. 2, pp. 91–94, Jul. 1982. DOI: 10.1103/physrevlett.49.91.

[4] Y.-H. Kim, R. Yu, S. P. Kulik, Y. Shih, and M. O. Scully, "Delayed "choice" quantum eraser," *Physical Review Letters*, vol. 84, no. 1, pp. 1–5, Jan. 2000. DOI: 10.1103/physrevlett.84.1.

[5] A. Steane, "Quantum computing," *Reports on Progress in Physics*, vol. 61, no. 2, pp. 117–173, Feb. 1998. DOI: 10.1088/0034-4885/61/2/002.

[6] N. Gisin and R. Thew, "Quantum communication," *Nature Photonics*, vol. 1, no. 3, pp. 165–171, Mar. 2007. DOI: 10.1038/nphoton.2007.22.

[7] M. A. Taylor and W. P. Bowen, "Quantum metrology and its application in biology," *Physics Reports*, vol. 615, pp. 1–59, Feb. 2016. DOI: 10.1016/j.physrep.2015.12.002.

[8] G. B. Lemos, V. Borish, G. D. Cole, S. Ramelow, R. Lapkiewicz, and A. Zeilinger, "Quantum imaging with undetected photons," *Nature*, vol. 512, no. 7515, pp. 409–412, Aug. 2014. DOI: 10.1038/nature13586.

[9] R. Ghosh and L. Mandel, "Observation of nonclassical effects in the interference of two photons," *Physical Review Letters*, vol. 59, no. 17, pp. 1903–1905, Oct. 1987. DOI: 10.1103/physrevlett.59.1903.

[10] C. K. Hong, Z. Y. Ou, and L. Mandel, "Measurement of subpicosecond time intervals between two photons by interference," *Physical Review Letters*, vol. 59, no. 18, pp. 2044–2046, Nov. 1987. DOI: 10.1103/physrevlett.59.2044.

[11] K. J. Kim, E. Santos, H. Nguyen, and S. Pieper, "An application of inverse reinforcement learning to estimate interference in drone swarms," *Entropy*, vol. 24, no. 10, p. 1364, Sep. 2022. DOI: 10.3390/e24101364.

[12] P. A. Morris, R. S. Aspden, J. E. C. Bell, R. W. Boyd, and M. J. Padgett, "Imaging with a small number of photons," *Nature Communications*, vol. 6, no. 1, Jan. 2015. DOI: 10.1038/ncomms6913.

[13] D. Walter, C. Pitsch, G. Paunescu, and P. Lutzmann, "Detection and jamming resistance of quantum ghost imaging for remote sensing," in *Electro-Optical Remote Sensing XIII*, G. W. Kamerman and O. Steinvall, Eds., SPIE, Oct. 2019. DOI: 10.1117/12.2532379.

[14] D. N. Klyshko, *Photons and nonlinear optics*, Apr. 2018. DOI: 10.1201/9780203743508.

[15] M. Kutas, B. Haase, P. Bickert, F. Riexinger, D. Molter, and G. von Freymann, "Terahertz quantum sensing," *Science Advances*, vol. 6, no. 11, Mar. 2020. DOI: 10.1126/sciadv.aaz8065.

[16] C. Lindner, "Nonlinear interferometers based on spontaneous parametric down-conversion for fourier-transform mid-infrared spectroscopy," en, Ph.D. dissertation, 2022. DOI: 10.6094/UNIFR/228229.

[17] F. G. Herbst, F. Elsen, B. Jungbluth, H.-D. Hoffmann, and C. L. Häfner, "Towards imaging with undetected photons with a nonlinear mach-zehnder-type interferometer in mir," in *Nonlinear Frequency Generation and Conversion: Materials and Devices XX*, P. G. Schunemann and K. L. Schepler, Eds., SPIE, Mar. 2021. DOI: 10.1117/12.2578639.

[18] M. Gilaberte Basset *et al.*, "Video-rate imaging with undetected photons," *Laser & Photonics Reviews*, vol. 15, no. 6, Apr. 2021. DOI: 10.1002/lpor.202000327.

[19] M. Gilaberte Basset, F. Setzpfandt, F. Steinlechner, E. Beckert, T. Pertsch, and M. Gräfe, "Perspectives for applications of quantum imaging," *Laser & Photonics Reviews*, vol. 13, no. 10, Sep. 2019. DOI: 10.1002/lpor.201900097.

[20] D. Walter, C. Pitsch, G. Paunescu, and P. Lutzmann, "Quantum ghost imaging for remote sensing," in *Quantum Communications and Quantum Imaging XVII*, K. S. Deacon, Ed., SPIE, Sep. 2019. DOI: 10.1117/12.2529268.

[21] F. IPM, *Q-ftir webseite, abgerufen am 26.02.2024*. [Online]. Available: https://www.ipm.fraunhofer.de/de/gf/gastechnologie-spektroskopie/komp/sensorik/quantensensorik.html.

[22] T. B. Pittman, Y. H. Shih, D. V. Strekalov, and A. V. Sergienko, "Optical imaging by means of two-photon quantum entanglement," *Physical Review A*, vol. 52, no. 5, R3429–R3432, Nov. 1995. DOI: 10.1103/physreva.52.r3429.

[23] S. Dello Russo *et al.*, "Advances in mid-infrared single-photon detection," *Photonics*, vol. 9, no. 7, p. 470, Jul. 2022. DOI: 10.3390/photonics9070470.

[24] M. Perenzoni, L. Pancheri, and D. Stoppa, "Compact SPAD-based pixel architectures for time-resolved image sensors," *Sensors*, vol. 16, no. 5, p. 745, May 2016. DOI: 10.3390/s16050745.

[25] D. Bronzi, F. Villa, S. Tisa, A. Tosi, and F. Zappa, "SPAD figures of merit for photon-counting, photon-timing, and imaging applications: A review," *IEEE Sensors Journal*, vol. 16, no. 1, pp. 3–12, Jan. 2016. DOI: 10.1109/jsen.2015.2483565.

[26] M. Caccia, L. Nardo, R. Santoro, and D. Schaffhauser, "Silicon photomultipliers and spad imagers in biophotonics: Advances and perspectives," *Nuclear Instruments and Methods in Physics Research Section A: Accelerators, Spectrometers, Detectors and Associated Equipment*, vol. 926, pp. 101–117, May 2019. DOI: 10.1016/j.nima.2018.10.204.

[27] J. F. Haase, S. Grollius, S. Grosse, A. Buchner, and M. Ligges, "A 32x24 pixel SPAD detector system for lidar and quantum imaging," in *Photonic Instrumentation Engineering VIII*, Y. Soskind and L. E. Busse, Eds., SPIE, Mar. 2021. DOI: 10.1117/12.2578775.

[28] P. Lecoq *et al.*, "Roadmap toward the 10 ps time-of-flight pet challenge," *Physics in Medicine & Biology*, vol. 65, no. 21, 21RM01, Oct. 2020. DOI: 10.1088/1361-6560/ab9500.

[29] M. Fishburn, L. H. Menninga, C. Favi, and E. Charbon, "A 19.6 ps, fpga-based tdc with multiple channels for open source applications," *IEEE Transactions on Nuclear Science*, vol. 60, no. 3, pp. 2203–2208, Jun. 2013. DOI: 10.1109/tns.2013.2241789.

[30] X. Llopart *et al.*, "Timepix4, a large area pixel detector readout chip which can be tiled on 4 sides providing sub-200 ps timestamp binning," *Journal of Instrumentation*, vol. 17, no. 01, p. C01044, Jan. 2022. DOI: 10.1088/1748-0221/17/01/c01044.

[31] K. Heijhoff *et al.*, "Timing performance of the timepix4 front-end," *Journal of Instrumentation*, vol. 17, no. 07, P07006, Jul. 2022. DOI: 10.1088/1748-0221/17/07/p07006.

[32] R. Kokozinski *et al.*, "SPAD-based flash lidar sensor with high ambient light rejection for automotive applications," in *Quantum Sensing and Nano Electronics and Photonics XV*, M. Razeghi, G. J. Brown, G. Leo, and J. S. Lewis, Eds., SPIE, Jan. 2018. DOI: 10.1117/12.2286879.

[33] E. Gros-Daillon *et al.*, "First characterization of the SPADnet sensor: A digital silicon photomultiplier for pet applications," *Journal of Instrumentation*, vol. 8, no. 12, pp. C12026–C12026, Dec. 2013. DOI: 10.1088/1748-0221/8/12/c12026.

[34] M. Unternährer, B. Bessire, L. Gasparini, M. Perenzoni, and A. Stefanov, "Super-resolution quantum imaging at the heisenberg limit," *Optica*, vol. 5, no. 9, p. 1150, Sep. 2018. DOI: 10.1364/optica.5.001150.

[35] B. Eckmann, B. Bessire, M. Unternährer, L. Gasparini, M. Perenzoni, and A. Stefanov, "Characterization of space-momentum entangled photons with a time resolving CMOS SPAD array," *Optics Express*, vol. 28, no. 21, p. 31 553, Oct. 2020. DOI: 10.1364/oe.401260.

[36] F. Qi and P. Zhang, "High-resolution multi-spectral snapshot 3D imaging with a SPAD array camera," *Optics Express*, vol. 31, no. 19, p. 30 118, Aug. 2023. DOI: 10.1364/oe.492581.

[37] A. Lyons *et al.*, "Attosecond-resolution hong-ou-mandel interferometry," *Science Advances*, vol. 4, no. 5, May 2018. DOI: 10.1126/sciadv.aap9416.

[38] C. Pitsch, D. Walter, S. Grosse, W. Brockherde, H. Bürsing, and M. Eichhorn, "Quantum ghost imaging using asynchronous detection," *Applied Optics*, vol. 60, no. 22, F66, Jun. 2021. DOI: 10.1364/ao.423634.

[39] C. Pitsch, D. Walter, L. Gasparini, H. Bürsing, and M. Eichhorn, "3D quantum ghost imaging," *Applied Optics*, vol. 62, no. 23, p. 6275, Aug. 2023. DOI: 10.1364/ao.492208.

[40] J. Garnier and G. Papanicolaou, *Passive Imaging with Ambient Noise*. Cambridge University Press, 2016, p. 306.

[41] tropos.de, *Tropos-webseite (lidar), , abgerufen am 27.11.2023*. [Online]. Available: $https://www.tropos.de/forschung/grossprojekte-infrastruktur-technologie/technologie-am-tropos/fernerkundung/lidar$.

[42] M. Eichhorn, *Lecture Notes: Laser Metrology, Summer Term 2022, Karlsruhe Institute of Technology (KIT)*.

[43] F. Angelini and F. Colao, "Optimization of laser wavelength, power and pulse duration for eye-safe raman spectroscopy," *Journal of the European Optical Society-Rapid Publications*, vol. 15, no. 1, Mar. 2019. DOI: 10.1186/s41476-019-0099-y.

[44] Z. Dai, A. Wolf, P.-P. Ley, T. Glück, M. C. Sundermeier, and R. Lachmayer, "Requirements for automotive lidar systems," *Sensors*, vol. 22, no. 19, p. 7532, Oct. 2022. DOI: 10.3390/s22197532.

[45] A. Rogalski, *Antimonide-based infrared detectors, A new perspective* (SPIE Press Monograph PM 280), M. Kopytko and P. Martyniuk, Eds. Bellingham, Washington, USA: SPIE Press, 2018, 1 p.

[46] S. M. Spuler and S. D. Mayor, "Scanning eye-safe elastic backscatter lidar at 1.54 μm," *Journal of Atmospheric and Oceanic Technology*, vol. 22, no. 6, pp. 696–703, Jun. 2005. DOI: 10.1175/jtech1755.1.

[47] J. Zheng, *Optical frequency-odulated continuous-wave (FMCW) interferometry* (Springer series in optical sciences 107). [New York, NY]: Springer, 2010, 245 pp.

[48] B. Göhler and P. Lutzmann, "SWIR laser gated-viewing at Fraunhofer IOSB," in *SPIE Proceedings*, G. Kamerman, O. Steinvall, K. L. Lewis, and J. D. Gonglewski, Eds., SPIE, Oct. 2015. DOI: 10.1117/12.2195932.

[49] B. Göhler and P. Lutzmann, "Penetration of pyrotechnic effects with SWIR laser gated viewing in comparison to VIS and thermal IR bands," in *Electro-Optical Remote Sensing X*, G. Kamerman and O. Steinvall, Eds., SPIE, Oct. 2016. DOI: 10.1117/12.2241072.

[50] M. Shangguan, Z. Yang, Z. Lin, Z. Lee, H. Xia, and Z. Weng, "Compact long-range single-photon underwater lidar with high spatial–temporal resolution," *IEEE Geoscience and Remote Sensing Letters*, vol. 20, pp. 1–5, 2023. DOI: 10.1109/lgrs.2023.3274449.

[51] B. Göhler and P. Lutzmann, "Review on short-wavelength infrared laser gated-viewing at fraunhofer IOSB," *Optical Engineering*, vol. 56, no. 3, p. 031 203, Sep. 2016. DOI: 10.1117/1.oe.56.3.031203.

[52] M.-J. Sun, M. P. Edgar, D. B. Phillips, G. M. Gibson, and M. J. Padgett, "Improving the signal-to-noise ratio of single-pixel imaging using digital microscanning," *Optics Express*, vol. 24, no. 10, p. 10 476, May 2016. DOI: 10.1364/oe.24.010476.

[53] R. S. Bennink, S. J. Bentley, R. W. Boyd, and J. C. Howell, "Quantum and classical coincidence imaging," *Physical Review Letters*, vol. 92, no. 3, p. 033 601, Jan. 2004. DOI: 10.1103/physrevlett.92.033601.

[54] J. H. Shapiro and R. W. Boyd, "The physics of ghost imaging," *Quantum Information Processing*, vol. 11, no. 4, pp. 949–993, Jan. 2012. DOI: 10.1007/s11128-011-0356-5.

[55] Y. Bromberg, O. Katz, and Y. Silberberg, "Ghost imaging with a single detector," *Physical Review A*, vol. 79, no. 5, p. 053 840, May 2009. DOI: 10.1103/physreva.79.053840.

[56] D. B. Phillips *et al.*, "Adaptive foveated single-pixel imaging with dynamic supersampling," *Science Advances*, vol. 3, no. 4, Apr. 2017. DOI: 10.1126/sciadv.1601782.

[57] M.-J. Sun, L.-T. Meng, M. P. Edgar, M. J. Padgett, and N. Radwell, "A russian dolls ordering of the hadamard basis for compressive single-pixel imaging," *Scientific Reports*, vol. 7, no. 1, Jun. 2017. DOI: 10.1038/s41598-017-03725-6.

[58] P. G. Vaz, D. Amaral, L. F. R. Ferreira, M. Morgado, and J. Cardoso, "Image quality of compressive single-pixel imaging using different hadamard orderings," *Optics Express*, vol. 28, no. 8, p. 11 666, Apr. 2020. DOI: 10.1364/oe.387612.

[59] M. Gilaberte Basset *et al.*, "Experimental analysis of image resolution of quantum imaging with undetected light through position correlations," *Physical Review A*, vol. 108, no. 5, p. 052 610, Nov. 2023. DOI: 10.1103/physreva.108.052610.

[60] X. Y. Zou, L. J. Wang, and L. Mandel, "Induced coherence and indistinguishability in optical interference," *Physical Review Letters*, vol. 67, no. 3, pp. 318–321, Jul. 1991. DOI: 10.1103/physrevlett.67.318.

[61] refractiveindex.info, *Refractive index database, abgerufen am 27.11.2023*. [Online]. Available: https://www.refractiveindex.info/.

[62] H. Di Lorenzo Pires and M. P. van Exter, "Near-field correlations in the two-photon field," *Physical Review A*, vol. 80, no. 5, p. 053 820, Nov. 2009. DOI: 10.1103/physreva.80.053820.

[63] I. Kim, D. Lee, and K. J. Lee, "Study of type ii SPDC in lithium niobate for high spectral purity photon pair generation," *Crystals*, vol. 11, no. 4, p. 406, Apr. 2021. DOI: 10.3390/cryst11040406.

[64] A. Christ, A. Fedrizzi, H. Hübel, T. Jennewein, and C. Silberhorn, "Parametric down-conversion," in *Single-Photon Generation and Detection - Physics and Applications*. Elsevier, 2013, pp. 351–410. DOI: 10.1016/b978-0-12-387695-9.00011-1.

[65] M. Hojo and K. Tanaka, "Broadband infrared light source by simultaneous parametric down-conversion," *Scientific Reports*, vol. 11, no. 1, Sep. 2021. DOI: 10.1038/s41598-021-97531-w.

[66] K. A. Forbes, J. S. Ford, G. A. Jones, and D. L. Andrews, "Quantum delocalization in photon-pair generation," *Physical Review A*, vol. 96, no. 2, p. 023 850, Aug. 2017. DOI: 10.1103/physreva.96.023850.

[67] K. A. Forbes, J. S. Ford, and D. L. Andrews, "Nonlocalized generation of correlated photon pairs in degenerate down-conversion," *Physical Review Letters*, vol. 118, no. 13, p. 133 602, Mar. 2017. DOI: 10.1103/physrevlett.118.133602.

[68] M. Houe and P. D. Townsend, "An introduction to methods of periodic poling for second-harmonic generation," *Journal of Physics D: Applied Physics*, vol. 28, no. 9, pp. 1747–1763, Sep. 1995. DOI: 10.1088/0022-3727/28/9/001.

[69] P. Xu and S. N. Zhu, "Review article: Quasi-phase-matching engineering of entangled photons," *AIP Advances*, vol. 2, no. 4, p. 041 401, Dec. 2012. DOI: 10.1063/1.4773457.

[70] R. W. Boyd, *Nonlinear optics*. Academic Press, 2008, p. 613.

[71] M. Widarsson, "Pulse generation and detection through intra-cavity up-conversion," QC 220511, Ph.D. dissertation, KTH, Laser Physics, 2022.

[72] F. Steinlechner *et al.*, "Efficient heralding of polarization-entangled photons from type-0 and type-ii spontaneous parametric downconversion in periodically poled $KTiOPO_4$," *Journal of the Optical Society of America B*, vol. 31, no. 9, p. 2068, Aug. 2014. DOI: 10.1364/josab.31.002068.

[73] M. V. Jabir and G. K. Samanta, "Robust, high brightness, degenerate entangled photon source at room temperature," *Scientific Reports*, vol. 7, no. 1, Oct. 2017. DOI: 10.1038/s41598-017-12709-5.

[74] A. Vanselow, P. Kaufmann, H. M. Chrzanowski, and S. Ramelow, "Ultra-broadband SPDC for spectrally far separated photon pairs," *Optics Letters*, vol. 44, no. 19, p. 4638, Sep. 2019. DOI: 10.1364/ol.44.004638.

[75] M. Kutas, B. Haase, J. Klier, D. Molter, and G. von Freymann, "Quantum-inspired terahertz spectroscopy with visible photons," *Optica*, vol. 8, no. 4, p. 438, Mar. 2021. DOI: 10.1364/optica.415627.

[76] M. Kutas *et al.*, "Quantum sensing with extreme light," *Advanced Quantum Technologies*, vol. 5, no. 6, Mar. 2022. DOI: 10.1002/qute.202100164.

[77] I. Kviatkovsky, H. M. Chrzanowski, E. G. Avery, H. Bartolomaeus, and S. Ramelow, "Microscopy with undetected photons in the mid-infrared," *Science Advances*, vol. 6, no. 42, Oct. 2020. DOI: 10.1126/sciadv.abd0264.

[78] A. Smith, *SNLO webseite, abgerufen am 17.11.2023*. [Online]. Available: https://as-photonics.com/products/snlo/.

[79] M. V. Pack, D. J. Armstrong, and A. V. Smith, "Measurement of the χ^2 tensors of $KTiOPO_4$, $KTiOAsO_4$, $RbTiOPO_4$, and $RbTiOAsO_4$ crystals," *Applied Optics*, vol. 43, no. 16, p. 3319, Jun. 2004. DOI: 10.1364/ao.43.003319.

[80] J. Svozilík, J. Peřina, and J. P. Torres, "High spatial entanglement via chirped quasi-phase-matched optical parametric down-conversion," *Physical Review A*, vol. 86, no. 5, p. 052 318, Nov. 2012. DOI: 10.1103/physreva.86.052318.

[81] A. Tanaka *et al.*, "Spectral properties of ultra-broadband entangled photons generated from chirped-MgSLT crystal towards monocycle entanglement generation," in *SPIE Proceedings*, Z. U. Hasan, P. R. Hemmer, H. Lee, and C. M. Santori, Eds., SPIE, Mar. 2013. DOI: 10.1117/12.2003390.

[82] T. W. Neely, L. Nugent-Glandorf, F. Adler, and S. A. Diddams, "Broadband mid-infrared frequency upconversion and spectroscopy with an aperiodically poled $LiNbO_3$ waveguide," *Optics Letters*, vol. 37, no. 20, p. 4332, Oct. 2012. DOI: 10.1364/ol.37.004332.

[83] T. B. Pittman, D. V. Strekalov, D. N. Klyshko, M. H. Rubin, A. V. Sergienko, and Y. H. Shih, "Two-photon geometric optics," *Physical Review A*, vol. 53, no. 4, pp. 2804–2815, Apr. 1996. DOI: 10.1103/physreva.53.2804.

[84] A. Vega, S. Saravi, T. Pertsch, and F. Setzpfandt, "Pinhole quantum ghost imaging," *Applied Physics Letters*, vol. 117, no. 9, Aug. 2020. DOI: 10.1063/5.0012477.

[85] B. Baghdasaryan, F. Steinlechner, and S. Fritzsche, "Justifying the thin-crystal approximation in spontaneous parametric down-conversion for collinear phase matching," *Physical Review A*, vol. 103, no. 6, p. 063 508, Jun. 2021. DOI: 10.1103/physreva.103.063508.

[86] D. R. Guido and A. B. U'Ren, "Study of the effect of pump focusing on the performance of ghost imaging and ghost diffraction, based on spontaneous parametric downconversion," *Optics Communications*, vol. 285, no. 6, pp. 1269–1274, Mar. 2012. DOI: 10.1016/j.optcom.2011.09.059.

[87] M. Reichert, X. Sun, and J. W. Fleischer, "Quality of spatial entanglement propagation," *Physical Review A*, vol. 95, no. 6, p. 063 836, Jun. 2017. DOI: 10.1103/physreva.95.063836.

[88] K. W. Chan, J. P. Torres, and J. H. Eberly, "Transverse entanglement migration in hilbert space," *Physical Review A*, vol. 75, no. 5, p. 050 101, May 2007. DOI: 10.1103/physreva.75.050101.

[89] K. W. C. Chan, M. N. O'Sullivan, and R. W. Boyd, "Two-color ghost imaging," *Physical Review A*, vol. 79, no. 3, p. 033 808, Mar. 2009. DOI: 10.1103/physreva.79.033808.

[90] M. Tsang, "Quantum imaging beyond the diffraction limit by optical centroid measurements," *Physical Review Letters*, vol. 102, no. 25, p. 253 601, Jun. 2009. DOI: 10.1103/physrevlett.102.253601.

[91] P.-A. Moreau *et al.*, "Resolution limits of quantum ghost imaging," *Optics Express*, vol. 26, no. 6, p. 7528, Mar. 2018. DOI: 10.1364/oe.26.007528.

[92] S. Cova, M. Ghioni, A. Lacaita, C. Samori, and F. Zappa, "Avalanche photodiodes and quenching circuits for single-photon detection," *Applied Optics*, vol. 35, no. 12, p. 1956, Apr. 1996. DOI: 10.1364/ao.35.001956.

[93] J. Haase, "Algorithmen und signalverarbeitung für lidar," de, Ph.D. dissertation, 2021. DOI: 10.17185/DUEPUBLICO/74921.

[94] M. Fishburn, "Fundamentals of CMOS single-photon avalanche diodes," Ph.D. dissertation, 2012. DOI: 10.4233/UUID:7ED6E57D-404E-4372-8053-6B0B5C7FA0FE.

[95] M. Moreno-Garcia, H. Xu, L. Gasparini, and M. Perenzoni, "Low-noise single photon avalanche diodes in a 110nm cis technology," in *2018 48th European Solid-State Device Research Conference (ESSDERC)*, IEEE, Sep. 2018. DOI: 10.1109/essderc.2018.8486883.

[96] X. Michalet *et al.*, "Silicon photon-counting avalanche diodes for single-molecule fluorescence spectroscopy," *IEEE Journal of Selected Topics in Quantum Electronics*, vol. 20, no. 6, pp. 248–267, Nov. 2014. DOI: 10.1109/jstqe.2014.2341568.

[97] D. Portaluppi, E. Conca, and F. Villa, "32x32 CMOS SPAD imager for gated imaging, photon timing, and photon coincidence," *IEEE Journal of Selected Topics in Quantum Electronics*, vol. 24, no. 2, pp. 1–6, Mar. 2018. DOI: 10.1109/jstqe.2017.2754587.

[98] N. Palina, T. Mueller, S. Mohanti, and A. G. Aberle, "Laser assisted boron doping of silicon wafer solar cells using nanosecond and picosecond laser pulses," in *2011 37th IEEE Photovoltaic Specialists Conference*, IEEE, Jun. 2011. DOI: 10.1109/pvsc.2011.6186392.

[99] S. Sze and G. Gibbons, "Effect of junction curvature on breakdown voltage in semiconductors," *Solid-State Electronics*, vol. 9, no. 9, pp. 831–845, Sep. 1966. DOI: 10.1016/0038-1101(66)90033-5.

[100] S. Grosse, A. Steuer, P. vom Stein, C. Zeidler, and J. Haase, "B10.1 a 64 x 48 BSI SPAD sensor based on 8" wafer 3d stacking technology," in *SMSI 2021 - Sensors and Instrumentation*, AMA Service GmbH, Von-Münchhausen-Str. 49, 31515 Wunstorf, Germany, 2021. DOI: 10.5162/smsi2021/b10.1.

[101] C. Bruschini, H. Homulle, I. M. Antolovic, S. Burri, and E. Charbon, "Single-photon avalanche diode imagers in biophotonics: Review and outlook," *Light: Science & Applications*, vol. 8, no. 1, Sep. 2019. DOI: 10.1038/s41377-019-0191-5.

[102] K. R. McIntosh, M. D. Abbott, and B. A. Sudbury, "Ray tracing isotextured solar cells," *Energy Procedia*, vol. 92, pp. 122–129, Aug. 2016. DOI: 10.1016/j.egypro.2016.07.041.

[103] F. Nolet *et al.*, "Quenching circuit and SPAD integrated in CMOS 65 nm with 7.8 ps FWHM single photon timing resolution," *Instruments*, vol. 2, no. 4, p. 19, Sep. 2018. DOI: 10.3390/instruments2040019.

[104] W. v. Muench and E. Pettenpaul, "Saturated electron drift velocity in 6h silicon carbide," *Journal of Applied Physics*, vol. 48, no. 11, pp. 4823–4825, Nov. 1977. DOI: 10.1063/1.323506.

[105] F. Gramuglia, M.-L. Wu, C. Bruschini, M.-J. Lee, and E. Charbon, "A low-noise CMOS SPAD pixel with 12.1 ps SPTR and 3 ns dead time," *IEEE Journal of Selected Topics in Quantum Electronics*, vol. 28, no. 2: Optical Detectors, pp. 1–9, Mar. 2022. DOI: 10.1109/jstqe.2021.3088216.

[106] D. Bronzi *et al.*, "Low-noise and large-area CMOS SPADs with timing response free from slow tails," in *2012 Proceedings of the European Solid-State Device Research Conference (ESSDERC)*, IEEE, Sep. 2012. DOI: 10.1109/essderc.2012.6343375.

[107] H. Xu, L. Pancheri, G.-F. D. Betta, and D. Stoppa, "Design and characterization of a p+/n-well SPAD array in 150nm CMOS process," *Optics Express*, vol. 25, no. 11, p. 12 765, May 2017. DOI: 10.1364/oe.25.012765.

[108] F. Villa, R. Lussana, D. Portaluppi, A. Tosi, and F. Zappa, "Time-resolved CMOS SPAD arrays: Architectures, applications and perspectives," in *Advanced Photon Counting Techniques XI*, M. A. Itzler and J. C. Campbell, Eds., SPIE, Jun. 2017. DOI: 10.1117/12.2262586.

[109] S. Henzler, *Time-To-Digital Converters* (Springer Series in Advanced Microelectronics Ser. v.29), 1st ed. Dordrecht: Springer Netherlands, 2010, 1131 pp., Description based on publisher supplied metadata and other sources.

[110] R. Machado, J. Cabral, and F. S. Alves, "Recent developments and challenges in fpga-based time-to-digital converters," *IEEE Transactions on Instrumentation and Measurement*, vol. 68, no. 11, pp. 4205–4221, Nov. 2019. DOI: 10.1109/tim.2019.2938436.

[111] G. W. Roberts and M. Ali-Bakhshian, "A brief introduction to time-to-digital and digital-to-time converters," *IEEE Transactions on Circuits and Systems II: Express Briefs*, vol. 57, no. 3, pp. 153–157, Mar. 2010. DOI: 10.1109/tcsii.2010.2043382.

[112] F. Villa *et al.*, "CMOS imager with 1024 SPADs and TDCs for single-photon timing and 3-d time-of-flight," *IEEE Journal of Selected Topics in Quantum Electronics*, vol. 20, no. 6, pp. 364–373, Nov. 2014. DOI: 10.1109/jstqe.2014.2342197.

[113] M. Zarghami *et al.*, "A 32x32-pixel CMOS imager for quantum optics with per-SPAD TDC, 19.48% fill-factor in a $44.64\mu m$ pitch reaching 1 mhz observation rate," *IEEE Journal of Solid-State Circuits*, vol. 55, no. 10, pp. 2819–2830, Oct. 2020. DOI: 10.1109/jssc.2020.3005756.

[114] C. Bruschini *et al.*, "Challenges and prospects for multi-chip microlens imprints on front-side illuminated SPAD imagers," *Optics Express*, vol. 31, no. 13, p. 21 935, Jun. 2023. DOI: 10.1364/oe.488177.

[115] M. Fox, *Quantum optics, an introduction*. Oxford University Press, 2006, p. 378.

[116] P. Seitz and A. Theuwissen, Eds., *Single-photon imaging*. Springer Berlin Heidelberg, 2011. DOI: 10.1007/978-3-642-18443-7.

[117] S. Ruder, *An overview of gradient descent optimization algorithms*, 2016. DOI: 10.48550/ARXIV.1609.04747.

[118] H. Vanherzeele and J. D. Bierlein, "Magnitude of the nonlinear-optical coefficients of $KTiOPO_4$," *Optics Letters*, vol. 17, no. 14, p. 982, Jul. 1992. DOI: 10.1364/ol.17.000982.

[119] G. H. Wagniere and S. Wozniak, "Nonlinear optical properties," in *Encyclopedia of Spectroscopy and Spectrometry*. Elsevier, 1999, pp. 1594–1608. DOI: 10.1006/rwsp.2000.0208.

[120] IDQuantique, *ID230 produkt-webseite, abgerufen am 30.11.2023*. [Online]. Available: https://www.idquantique.com/quantum-sensing/products/id230/.

[121] F. Kaneda, K. Garay-Palmett, A. B. U'Ren, and P. G. Kwiat, "Heralded single-photon source utilizing highly nondegenerate, spectrally factorable spontaneous parametric downconversion," *Optics Express*, vol. 24, no. 10, p. 10 733, May 2016. DOI: 10.1364/oe.24.010733.

[122] A. Vega *et al.*, "Fundamental resolution limit of quantum imaging with undetected photons," *Physical Review Research*, vol. 4, no. 3, p. 033 252, Sep. 2022. DOI: 10.1103/physrevresearch.4.033252.

[123] E. Slenders *et al.*, "Cooled SPAD array detector for low light-dose fluorescence laser scanning microscopy," *Biophysical Reports*, vol. 1, no. 2, p. 100 025, Dec. 2021. DOI: 10.1016/j.bpr.2021.100025.

[124] C. Bruschini, H. Homulle, and E. Charbon, "Ten years of biophotonics single-photon SPAD imager applications: Retrospective and outlook," in *Multiphoton Microscopy in the Biomedical Sciences XVII*, A. Periasamy, P. T. C. So, K. König, and X. S. Xie, Eds., SPIE, Feb. 2017. DOI: 10.1117/12.2256247.

[125] S. Vasile, J. Cheng, J. Lipson, J. Liu, and J. Michel, "Single-photon imaging camera development for night vision," in *Infrared Technology and Applications XXXVI*, B. F. Andresen, G. F. Fulop, and P. R. Norton, Eds., SPIE, Apr. 2010. DOI: 10.1117/12.852646.

[126] V. Zickus *et al.*, "Fluorescence lifetime imaging with a megapixel SPAD camera and neural network lifetime estimation," *Scientific Reports*, vol. 10, no. 1, Dec. 2020. DOI: 10.1038/s41598-020-77737-0.

[127] M. Beer, C. Thattil, J. F. Haase, W. Brockherde, and R. Kokozinski, "2x192 pixel CMOS SPAD-based flash LiDAR sensor with adjustable background rejection," in *2018 25th IEEE International Conference on Electronics, Circuits and Systems (ICECS)*, IEEE, Dec. 2018. DOI: 10.1109/icecs.2018.8617905.

[128] F. IMS, *Website des CSPAD Alpha, abgerufen am 17.11.2023*. [Online]. Available: https://www.ims.fraunhofer.de/de/Geschaeftsfelder/CMOS-Image-Sensors/Technologien/CSPAD-alpha.html.

[129] L. Gasparini *et al.*, "A 32x32-pixel time-resolved single-photon image sensor with $44.64\mu m$ pitch and 19.48% fill-factor with on-chip row/frame skipping features reaching 800khz observation rate for quantum physics applications," in *2018 IEEE International Solid - State Circuits Conference - (ISSCC)*, IEEE, Feb. 2018. DOI: 10.1109/isscc.2018.8310202.

[130] M. Zarghami, L. Gasparini, M. Perenzoni, and L. Pancheri, "High dynamic range imaging with TDC-based CMOS SPAD arrays," *Instruments*, vol. 3, no. 3, p. 38, Aug. 2019. DOI: 10.3390/instruments3030038.

[131] F. IMS, *Datenblatt SPADeye2, abgerufen am 30.11.2023*. [Online]. Available: https://www.ims.fraunhofer.de/content/dam/ims/de/newsroom/kernkompetenzen/technology/SPADeye2.pdf.

[132] F. J. Duarte, *Tunable laser optics*, Second edition, First issued in paperback. Boca Raton: CRC Press, 2017, 323 pp., Literaturverz. S. 293 - 315.

[133] F. Roeder *et al.*, *Measurement of ultrashort bi-photon correlation times with an integrated two-colour broadband su(1,1)-interferometer*, 2023. DOI: 10.48550/ARXIV.2310.04293.

[134] W. Freude, *Lecture Notes: Optical waveguides and fibers, Winter Term 2018, Karlsruhe Institute of Technology (KIT)*.

[135] C. Pitsch, D. Walter, and S. Grosse, "Supplementary document for quantum ghost imaging using asynchronous detection - 5255832.pdf," 2021. DOI: 10.6084/M9.FIGSHARE.14665131.V2.

[136] C. Pitsch, D. Walter, L. Gasparini, H. Bürsing, and M. Eichhorn, *A method to correct the temporal drift of single photon detectors, based on asynchronous quantum ghost imaging*, 2024. DOI: 10.48550/ARXIV.2402.14365.

[137] Thorlabs, *ND filter produkt-webseite, abgerufen am 12.12.2023*. [Online]. Available: https://www.thorlabs.com/newgrouppage9.cfm?objectgroup_id=5022.

[138] Thorlabs, *Wedged ND filter produkt-webseite, abgerufen am 12.12.2023*. [Online]. Available: https://www.thorlabs.com/newgrouppage9.cfm?objectgroup_id=14282.

[139] P. F. McManamon, P. Banks, J. Beck, A. S. Huntington, and E. A. Watson, "A comparison flash lidar detector options," in *Laser Radar Technology and Applications XXI*, M. D. Turner and G. W. Kamerman, Eds., SPIE, May 2016. DOI: 10.1117/12.2229068.

[140] S. Miller and R. Turner, "A dynamic lunar spectral irradiance data set for npoess/viirs day/night band nighttime environmental applications," *IEEE Transactions on Geoscience and Remote Sensing*, vol. 47, no. 7, pp. 2316–2329, Jul. 2009. DOI: 10.1109/tgrs.2009.2012696.

[141] F. Crete, T. Dolmiere, P. Ladret, and M. Nicolas, "The blur effect: Perception and estimation with a new no-reference perceptual blur metric," in *Human Vision and Electronic Imaging XII*, B. E. Rogowitz, T. N. Pappas, and S. J. Daly, Eds., SPIE, Feb. 2007. DOI: 10.1117/12.702790.

[142] R. S. Bennink, "Optimal collinear gaussian beams for spontaneous parametric down-conversion," *Physical Review A*, vol. 81, no. 5, p. 053 805, May 2010. DOI: 10.1103/physreva.81.053805.

[143] J. Schneeloch *et al.*, "Introduction to the absolute brightness and number statistics in spontaneous parametric down-conversion," *Journal of Optics*, vol. 21, no. 4, p. 043 501, Feb. 2019. DOI: 10.1088/2040-8986/ab05a8.

[144] V. Nissen, *Einführung in Evolutionäre Algorithmen*. Vieweg+Teubner Verlag, 1997. DOI: 10.1007/978-3-322-93861-9.

[145] I. Gerdes, *Evolutionäre Algorithmen, Genetische Algorithmen - Strategien und Optimierungsverfahren - Beispielanwendungen* (Computational Intelligence), F. Klawonn and R. Kruse, Eds. Wiesbaden: Vieweg+Teubner Verlag, 2004, 1252 pp.

[146] C. P. Dominik Walter Simon Grosse, "Quantentechnologien.," in R. Neugebauer, Ed. Stuttgart: Fraunhofer Verlag, 2022, ch. Quanten-Ghost-Imaging mit asynchroner Detektion, pp. 175–190.

[147] A. S. Solntsev, P. Kumar, T. Pertsch, A. A. Sukhorukov, and F. Setzpfandt, "LiNbO3 waveguides for integrated SPDC spectroscopy," *APL Photonics*, vol. 3, no. 2, Feb. 2018. DOI: 10.1063/1.5009766.

[148] J. Haas and B. Mizaikoff, "Advances in mid-infrared spectroscopy for chemical analysis," *Annual Review of Analytical Chemistry*, vol. 9, no. 1, pp. 45–68, Jun. 2016. DOI: 10.1146/annurev-anchem-071015-041507.

[149] V. F. Gili *et al.*, "Experimental realization of scanning quantum microscopy," *Applied Physics Letters*, vol. 121, no. 10, Sep. 2022. DOI: 10.1063/5.0095972.

[150] K. Morimoto *et al.*, "Megapixel time-gated SPAD image sensor for 2D and 3D imaging applications," *Optica*, vol. 7, no. 4, p. 346, Apr. 2020. DOI: 10.1364/optica.386574.

[151] V. F. Gili *et al.*, "Quantum ghost imaging based on a "looking back" 2D SPAD array," *Applied Optics*, vol. 62, no. 12, p. 3093, Apr. 2023. DOI: 10.1364/ao.487084.

[152] A. R. Harvey, J. Lawlor, A. I. McNaught, J. W. Williams, and D. W. Fletcher-Holmes, "Hyperspectral imaging for the detection of retinal disease," in *Imaging Spectrometry VIII*, S. S. Shen, Ed., SPIE, Nov. 2002. DOI: 10.1117/12.451693.

[153] E. R. Reshef, J. B. Miller, and D. G. Vavvas, "Hyperspectral imaging of the retina: A review," *International Ophthalmology Clinics*, vol. 60, no. 1, pp. 85–96, Dec. 2019. DOI: 10.1097/iio.0000000000000293.

[154] R. Xue, Y. Kang, T. Zhang, L. Li, and W. Zhao, "Sub-pixel scanning high-resolution panoramic 3D imaging based on a SPAD array," *IEEE Photonics Journal*, vol. 13, no. 4, pp. 1–6, Aug. 2021. DOI: 10.1109/jphot.2021.3103817.

[155] R. Ballabriga *et al.*, "The timepix4 analog front-end design: Lessons learnt on fundamental limits to noise and time resolution in highly segmented hybrid pixel detectors," *Nuclear Instruments and Methods in Physics Research Section A: Accelerators, Spectrometers, Detectors and Associated Equipment*, vol. 1045, p. 167 489, Jan. 2023. DOI: 10.1016/j.nima.2022.167489.

[156] V. Vidyapin, Y. Zhang, D. England, and B. Sussman, "Characterisation of a single photon event camera for quantum imaging," *Scientific Reports*, vol. 13, no. 1, Jan. 2023. DOI: 10.1038/s41598-023-27842-7.

[157] J. Liu, Y. Xu, Y. Li, Z. Liu, and X. Zhao, "Exploiting the single-photon detection performance of ingaas negative-feedback avalanche diode with fast active quenching," *Optics Express*, vol. 29, no. 7, p. 10 150, Mar. 2021. DOI: 10.1364/oe.420368.

[158] G. Gras *et al.*, "Optical control of single-photon negative-feedback avalanche diode detector," *Journal of Applied Physics*, vol. 127, no. 9, Mar. 2020. DOI: 10.1063/1.5140824.

[159] ADEQUADE, *Webseite des EU-projekt ADEQUADE, abgerufen am 01.12.2023*. [Online]. Available: https://adequade.eu/.

[160] M. Beer, J. Haase, J. Ruskowski, and R. Kokozinski, "Background light rejection in SPAD-based lidar sensors by adaptive photon coincidence detection," *Sensors*, vol. 18, no. 12, p. 4338, Dec. 2018. DOI: 10.3390/s18124338.

[161] Hamamtsu Photonics, *Webseite eines multi-pixel-SPAD-detektor, abgerufen am 19.12.2023*. [Online]. Available: https://www.hamamatsu.com/jp/en/product/optical-sensors/mppc.html.

[162] L. Stasi, G. Gras, R. Berrazouane, M. Perrenoud, H. Zbinden, and F. Bussières, "Fast high-efficiency photon-number-resolving parallel superconducting nanowire single-photon detector," *Physical Review Applied*, vol. 19, no. 6, p. 064 041, Jun. 2023. DOI: 10.1103/physrevapplied.19.064041.

[163] IDQuantique, *Webseite eines freiraum gekoppelten ingaas-SPAD, abgerufen am 19.12.2023*. [Online]. Available: https://www.idquantique.com/quantum-sensing/products/id-qube-nir-free-running/.

[164] C. M. Natarajan, M. G. Tanner, and R. H. Hadfield, "Superconducting nanowire single-photon detectors: Physics and applications," *Superconductor Science and Technology*, vol. 25, no. 6, p. 063 001, Apr. 2012. DOI: 10.1088/0953-2048/25/6/063001.

[165] F. Marsili *et al.*, "Single-photon detectors based on ultranarrow superconducting nanowires," *Nano Letters*, vol. 11, no. 5, pp. 2048–2053, May 2011. DOI: 10.1021/nl2005143.

[166] I. Esmaeil Zadeh *et al.*, "Superconducting nanowire single-photon detectors: A perspective on evolution, state-of-the-art, future developments, and applications," *Applied Physics Letters*, vol. 118, no. 19, May 2021. DOI: 10.1063/5.0045990.

[167] B. Korzh *et al.*, "Demonstration of sub-3 ps temporal resolution with a superconducting nanowire single-photon detector," *Nature Photonics*, vol. 14, no. 4, pp. 250–255, Mar. 2020. DOI: 10.1038/s41566-020-0589-x.

[168] Y. Pan *et al.*, "Mid-infrared nb4n3-based superconducting nanowire single photon detectors for wavelengths up to $10\mu m$," *Optics Express*, vol. 30, no. 22, p. 40 044, Oct. 2022. DOI: 10.1364/oe.472378.

[169] K. Huang, J. Fang, M. Yan, E. Wu, and H. Zeng, "Wide-field mid-infrared single-photon upconversion imaging," *Nature Communications*, vol. 13, no. 1, Feb. 2022. DOI: 10.1038/s41467-022-28716-8.

[170] M. Widarsson, M. Henriksson, L. Barrett, V. Pasiskevicius, and F. Laurell, "Room temperature photon-counting lidar at $3\mu m$," *Applied Optics*, vol. 61, no. 4, p. 884, Jan. 2022. DOI: 10.1364/ao.444963.

[171] K. Huang *et al.*, "Mid-infrared photon counting and resolving via efficient frequency upconversion," *Photonics Research*, vol. 9, no. 2, p. 259, Feb. 2021. DOI: 10.1364/prj.410302.

List of Publications

Journal Contributions

Carsten Pitsch, Dominik Walter, Simon Grosse, Werner Brockherde, Helge Bürsing, and Marc Eichhorn, "Quantum ghost imaging using asynchronous detection," Appl. Opt. 60, F66-F70 (2021). (editor's pick)

Carsten Pitsch, Dominik Walter, Leonardo Gasparini, Helge Bürsing, and Marc Eichhorn, "3D quantum ghost imaging," Appl. Opt. 62, 6275-6281 (2023). (editor's pick)

Carsten Pitsch, Dominik Walter, Leonardo Gasparini, Helge Bürsing, and Marc Eichhorn. "A Method to Correct the Temporal Drift of Single-Photon Detectors Based on Asynchronous Quantum Ghost Imaging," Sensors 24, no. 8: 2578 (2024).

Patent

Dominik Walter and **Carsten Pitsch**. "System und Verfahren zur Bildrekonstruktion unter Verwendung eines optischen Aufbaus zur aktiven Beleuchtung mit einzelnen Photonen," (03/2020).

Conference Contributions

Dominik Walter, **Carsten Pitsch**, Gabriela Paunescu, and Peter Lutzmann. "Quantum ghost imaging for remote sensing", Proc. SPIE 11134, 111340W (2019)

Dominik Walter, **Carsten Pitsch**, Gabriela Paunescu, and Peter Lutzmann. "Detection and jamming resistance of quantum ghost imaging for remote sensing", Proc. SPIE 11160, 1116002 (2019)

Carsten Pitsch, Dominik Walter, Peter Lutzmann, Helge Bürsing, and Marc Eichhorn. “Asynchronous Quantum Ghost Imaging,” in Quantum Information and Measurement VI 2021 (Optica), paper Th4A.3 (2021)

Dominik Walter, **Carsten Pitsch**, and Helge Bürsing. “Quantum Ghost Imaging for Remote Sensing,” in Optica Sensing Congress 2023 (AIS, FTS, HISE, Sensors, ES), paper SM3D.5 (2023)

Carsten Pitsch, Dominik Walter, Helge Bürsing, and Marc Eichhorn. “3D quantum ghost imaging”, Proc. SPIE 12740, 1274006 (2023)

Carsten Pitsch, Dominik Walter, Peter Lutzmann, Helge Bürsing, and Marc Eichhorn. “3-Dimensional Quantum Ghost Imaging” [Poster]. In Sensing with Quantum Light (790. WE-Heraeus-Seminar) (2023)

Carsten Pitsch, Dominik Walter, Helge Bürsing, and Marc Eichhorn. “Remote quantum ghost imaging”, Proc. SPIE 12912, 129120W (2024)

Book Contributions

Carsten Pitsch, Dominik Walter, Simon Grosse. “Quantentechnologien”, techreport “Quanten-Ghost-Imaging mit asynchroner Detektion”, pages 175–190. Fraunhofer Verlag, Stuttgart, 2022

Acknowledgements

Here, I would like to thank the people who supported me while writing this thesis and contributed to its completion.

Special thanks go to my supervisor, Dr. Dominik Walter, who developed the foundations of asynchronous QGI even before I joined his group and always had an open ear for even the most absurd ideas. Without his contributions, this work would probably not have come this far.

My thanks also go to the entire Fraunhofer Institute for Optronics, System Technologies, and Image Exploitation (IOSB) and the Institute for Control Systems (IRS) at KIT, along with their staff. First and foremost, I thank my professor and institute director, Dr. Marc Eichhorn, and my department head, Dr. Helge Bürsing, who ensured that I could fully focus on the scientific work during this project and advised me on any questions I had. Additionally, I would like to especially thank the Optronics (OPT) and Laser Technology (LAS) departments, who always supported me with equipment and a helping hand, and with whom, during lunch breaks, one could discuss not only work but also topics such as laser-based mosquito defense, the absurdities of large administrations, the existence of pink elephants, the optimal cheese-to-spätzle ratio, and the woes of a barely planned SAP implementation.

In addition to my Fraunhofer Institute, I am also grateful to all the colleagues from my first project, the Fraunhofer project QUILT. I would like to thank Simon Grosse and Dr. Manuel Ligges from the Fraunhofer Institute for Microelectronic Circuits and Systems (IMS), who developed my first detectors and helped integrate them into our system. Special thanks also go to Dr. Markus Gräfe (now at TU Darmstadt), to whom I could turn with any questions about quantum correlation and without whom the connection to FBK would not have been established. I would also like to thank Fondazione Bruno Kessler (FBK), our current manufacturer, for lending us their detector, especially Dr. Leonardo Gasparini, who could answer even the most detailed questions and with whom it is always a pleasure to co-author a paper.

Beyond my work environment, I would, of course, like to thank my personal support network, which has

supported me throughout this project as well as my previous studies. Special thanks go to my parents, who ensured that I could focus on my studies, and to my roommate, who patiently listened to all my frustrations. I would also like to thank my girlfriend, who, even though we haven't known each other for long, provides me with exactly the motivation I need.

Finally, I would like to thank the examination committee for reviewing this thesis: Dr. Christian Koos, Dr. Sebastian Kempf, Dr. Ulrich Lemmer, and especially Dr. Markus Gräfe for being willing to provide additional evaluation for this work.